

Special Issue: Measurement, control, and analysis of motion using ICT and AI

Preface to the Special Issue

Ryuichi Imai ¹

¹ Faculty of Engineering and Design, Hosei University, 2-33 Ichigaya-tamachi, Shinjuku-ku, Tokyo 162-0843, Japan

In recent years, the rapid advancement of ICT (Information and Communication Technology) and AI (Artificial Intelligence) has led to increased research activity in the measurement, control, and analysis of various moving entities, including humans and machines. These technologies are being applied across a wide range of fields, including construction, agriculture, manufacturing, healthcare, and sports, driving the development of innovative methodologies.

In the field of measurement technology, advancements in sensors and IoT (Internet of Things) have enabled real-time and highly precise data collection. For example, on construction sites, precise tracking of heavy machinery and workers contributes to improved safety and operational efficiency. In agriculture, drones and robots are being utilized to monitor crop growth, facilitating the advancement of precision farming.

In the domain of control technology, autonomous driving and robotics have made significant progress, enabling the independent operation of moving entities in diverse environments. In the manufacturing sector, AI-driven robotic control is enhancing productivity and reducing labor burdens. Similarly, in healthcare, the integration of AI into surgical support robots is enabling more precise medical procedures, marking a transformative shift in medical technology.

In the area of motion analysis, researchers are analyzing collected data to understand behavioral patterns and convert tacit knowledge into explicit knowledge. In sports science, motion analysis of athletes is aiding in performance enhancement, while in the medical field, research is being conducted to quantify rehabilitation effectiveness, facilitating more effective treatment strategies.

This special issue aims to gather the latest research findings on the measurement, control, and analysis of moving entities across various domains and to foster innovation through interdisciplinary and cross-sector collaboration. By facilitating knowledge exchange and cooperation among researchers and engineers from different fields, further technological advancements can be expected. We hope that this special issue will contribute to the continued evolution of both academic and technological frontiers.

Published: 26 March 2025

* Correspondence: imai@hosei.ac.jp

Publisher's Note: JOURNAL OF DIGITAL LIFE. stays neutral with regard to jurisdictional claims in published maps and institutional affiliations.



Copyright: © SANKEI DIGITAL INC. Submitted for possible open access publication under the terms and conditions of the Creative Commons Attribution (CC BY) license (<https://creativecommons.org/licenses/by/4.0/>).

Special Issue: Measurement, control, and analysis of motion using ICT and AI
 Article

Fundamental Study on Detection of Dangerous Objects on the Road Surface Leading to Motorcycle Accidents Using a 360-Degree Camera

Haruka Inoue ^{1, *} and Yuma Nakasuji ¹

¹ Faculty of Information Technology and Social Sciences, Osaka University of Economics, 2-2-8 Higashiyodogawa-ku, Osaka 533-8533, Japan

Abstract

In recent years, the number of fatalities in traffic accidents involving motorcyclists has remained almost unchanged, with single-vehicle accidents accounting for 37.2% of all accidents by accident type in the past five years. In the development of overturn prevention devices for motorcycles, problems remain in post-mounting of the device as well as its downsizing. On the other hand, an existing study using deep learning has proposed a method for detecting dangerous objects on the road surface leading motorcycles to overturn, though this method still needs verification under different conditions. In this study, we apply a method for detecting dangerous objects on the road surface from video images using YOLO to two types of 360-degree cameras and verify that this method is versatile under different conditions.

Keywords: Motorcycle; Dangerous objects on the road surface; 360-degree camera; Deep learning.

1. Introduction

In recent years, the number of fatalities in traffic accidents involving motorcyclists has remained almost unchanged, and although the Metropolitan Police Department has been conducting motorcycle safety classes, the number of fatalities increased for all ages in 2023. Single-vehicle accidents accounted for 37.2% of all accidents by accident type in the past five years from 2018 to 2022 (Tokyo Metropolitan Police Department, 2024). The occurrence situations of traffic accidents resulting in injury or death in 2024 show that the number of fatalities from motorcycle accidents is about twice as high as that of automobiles accidents. Although ADAS (Nikkei xTECH, 2024), an advanced safety technology for motorcycles has been developed, its diffusion is slower than that for automobiles. Therefore, riders are required to follow the traffic rules and instantly predict danger. An existing study on the development of an overturn prevention device for motorcycles using the gyro effect suggests a need for downsizing the device (Senoo et al., 2017). A study on detecting dangerous objects as well as detection of dangerous objects that may cause motorcycles to overturn using deep learning (Inoue et al., 2023) as well as a study on detecting dangers leading to motorcycle accidents using 360-degree cameras (Inoue et al., 2024) show the difficult issue of verification under different conditions. In this study, we apply a method to detect dangerous objects on the road surface from video images using YOLO to two types of 360-degree cameras (hereinafter referred to as "Dangerous object detection method") and verify that this method is versatile. In this study, as with the existing studies, fallen leaves, gravel, manholes, bumps, and wet road surfaces are considered as dangerous objects on the road surface.

2. Method

Fig. 1 shows the process flow of the dangerous object detection method. The dangerous object detection method consists of a learning function and an estimation function. The input data for the learning function is the learning data, and the output data is the dangerous object detection model. The input data for the estimation function are video

Received: 22 November 2024, Accepted: 18 January 2025, Published: 26 March 2025

* Correspondence: h.inoue@osaka-ue.ac.jp

Publisher's Note: JOURNAL OF DIGITAL LIFE. stays neutral with regard to jurisdictional claims in published maps and institutional affiliations.



Copyright: © SANKEI DIGITAL INC. Submitted for possible open access publication under the terms and conditions of the Creative Commons Attribution (CC BY) license (<https://creativecommons.org/licenses/by/4.0/>).

images taken by the 360-degree camera while riding a motorcycle, and the output data are the results of dangerous object detection.

The learning function builds up a learning model to detect dangerous objects on the road surface that may cause a motorcycle to overturn. Specifically, as shown in Table 1, the model to detect fallen leaves, gravel, manholes, bumps, and wet road surface as dangerous objects from video images (hereinafter referred to as "dangerous object detection model") by annotating dangerous objects on the road surface and learning them using YOLOv5.

The estimation function is used to detect dangerous objects on the road surface from video images captured by the 360-degree camera. In the image generation process, the THETA+ application is used to convert the display format to flat, and crop to 1.91:1, and cut out the video image at 3 fps. The dangerous object detection process is used to detect dangerous objects on the road surface using the dangerous object detection model built up by the learning function.

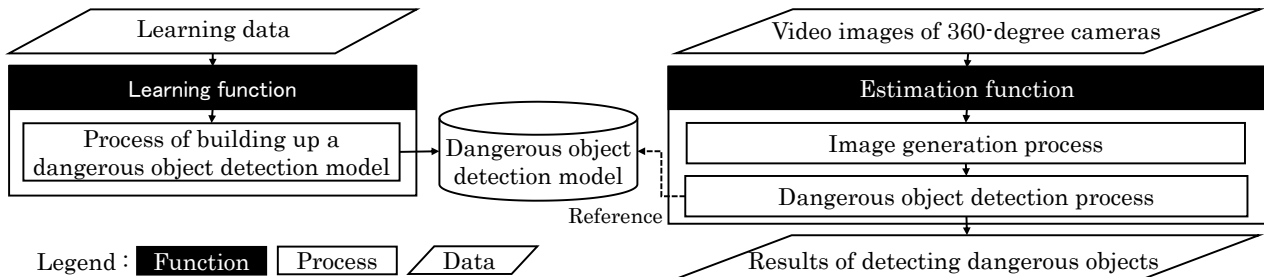


Fig. 1. Process Flow

Table 1. Example of annotation



3. Demonstration Experiment

In this experiment, we confirm the versatility of the proposed method by applying it to the video images shot by using 360-degree cameras under different conditions regarding types of cameras, resolution, and the versions of YOLO. The experimental conditions for Experiments 1 through 3 are shown in Table 2.

3.1. Method of the experiment

First, this study targets two types of cameras: THETA SC and THETA V, both of which are products of RICOH. In this experiment, each of the 360-degree cameras are installed at the front part the motorcycle (Fig. 2). A male person in his 20s rides the motorcycle along the same section of road in the urban area of Wakayama Prefecture multiple times with the same speed as much as possible. Then, the results of detecting dangerous objects detected by applying the dangerous object detection method to the respective video images are compared with the manually generated correct-answer data, to make evaluation based on precision, recall, and F-measure. The learning model was built up using different images from the data used for the evaluation. For the learning data, the data shot by THETA SC on

Table 2. Experimental conditions

| Experiment | Camera | | Video resolution | | YOLO | |
|------------|----------|---------|------------------|----|------|----|
| | THETA SC | THETA V | Full HD | 4K | v5 | v8 |
| 1 | ○ | ○ | ○ | - | ○ | - |
| 2 | - | ○ | ○ | ○ | ○ | - |
| 3 | ○ | - | ○ | - | ○ | ○ |



Fig. 2. Experimental view

March 20, 21, July 10, and 12, 2024 were used. 3,103 images were used for the dangerous object detection model. On the other hand, the evaluation data were those shot by THETA SC and THETA V on March 22 and July 11, 2024.

3.2. Experiment 1: Verification of versatility for different types of cameras

In Experiment 1, The dangerous object detection method is applied to the video images shot using THETA SC and THETA V to verify its versatility for different types of cameras. The ISO sensitivity differs between the two, ranging from 100 to 1,600 with THETA SC and from 64 to 6,400 with THETA V. The video resolution is 1,920 x 960 for both.

Table 3 shows the experimental results of Experiment 1, and Table 4 shows an example of the results of detecting dangerous objects. The overall F-measure is 0.917 for THETA SC and 0.839 for THETA V respectively, indicating that the dangerous object detection method is capable of detecting dangerous objects on the road surface correctly on the whole. Comparing the F-measure by camera type, the difference between THETA SC and THETA V was 0.078, which is not much difference. However, as the results of detecting bumps and wet road surface shown in Table 3, there were cases where only one of the 360-degree cameras was able to detect dangerous objects, even when the images were taken at the same point. Besides, comparing the F-measure by dangerous object type, the F-measure was lower for bumps and wet road surfaces than for fallen leaves, gravel, and manholes. Focusing on the result of detecting dangerous objects, there was a tendency of omission of detection for small bumps or wet road surfaces covered with shadows. We will increase the number of learning data under various environments and change the version of YOLO in order to advance the system.

Table 3. Experimental result of Experiment 1

| Camera | Video resolution | YOLO | Dangerous objects | Fallen leave | Gravel | Manhole | Bump | Wet road surface | Total |
|----------|------------------|------|-------------------------------|--------------|--------|---------|-------|------------------|-------|
| THETA SC | Full HD | v5 | Total number | 20 | 23 | 11 | 47 | 11 | 112 |
| | | | Number of determination cases | 19 | 19 | 8 | 37 | 8 | 91 |
| | | | Number of correct answers | 19 | 19 | 8 | 37 | 8 | 91 |
| | | | Precision | 1.000 | 1.000 | 1.000 | 1.000 | 1.000 | 1.000 |
| | | | Recall | 0.950 | 0.826 | 0.727 | 0.787 | 0.727 | 0.813 |
| | | | F-measure | 0.974 | 0.905 | 0.842 | 0.881 | 0.842 | 0.897 |
| THETA V | | | Total number | 16 | 18 | 8 | 44 | 11 | 97 |
| | | | Number of determination cases | 15 | 13 | 7 | 33 | 7 | 75 |
| | | | Number of correct answers | 15 | 13 | 7 | 33 | 7 | 75 |
| | | | Precision | 1.000 | 1.000 | 1.000 | 1.000 | 1.000 | 1.000 |
| | | | Recall | 0.938 | 0.722 | 0.875 | 0.750 | 0.636 | 0.773 |
| | | | F-measure | 0.968 | 0.839 | 0.933 | 0.857 | 0.778 | 0.872 |

Table 4. Result of detecting dangerous objects with different cameras

| Dangerous objects | Fallen leave | Gravel | Manhole | Bump | Wet road surface |
|-------------------|---|---|---|---|---|
| THETA SC |  |  |  |  |  |
| THETA V |  |  |  |  |  |

3.3. Experiment 2: Verification of versatility for different resolutions

In Experiment 2, the dangerous object detection method is applied to the video images shot using THETA V with resolutions of 1,920 x 960 and 2,840 x 1,920 to verify its versatility for different resolutions. It should be noted that as THETA SC only has a resolution of 1,920 x 960, it was excluded from the experiment.

Table 5 shows the experimental results of Experiment 2, and Table 6 shows an example of the results of detecting dangerous objects. The overall F-measure is 0.872 for full HD, and 0.857 for 4k, indicating that the dangerous object detection method is capable of detecting dangerous objects on the road surface correctly for the most part. Comparing the F-measure by the resolutions, the difference between full HD and 4K was 0.015, which was not a large difference. However, the result of detection shows the tendency that 4k is capable of detecting dangerous objects on the road surface located at a remote distance compared with full HD.

Comparison of F-measure by types of dangerous objects shows that it is high for fallen leaves and manholes in the case of 4K, just as the same with full HD. Focusing on the dangerous object for which the F-measure for 4K is lower than that for full HD, examples of success and failure of gravel, bumps, and wet road surfaces are shown in Table 7. The result of detection indicates the tendency of failing to detect light-colored gravel, bumps where it was difficult to visually check the unevenness of the road surface, and the road surface where the wetted area is small. In the future, we plan to advance the method by increasing the learning data under diverse environments and by changing the version of YOLO.

Table 5. Experimental result of Experiment 2

| Camera | Video resolution | YOLO | Dangerous objects | Fallen leave | Gravel | Manhole | Bump | Wet road surface | Total |
|---------|------------------|------|-------------------------------|--------------|--------|---------|-------|------------------|-------|
| THETA V | 4K | v5 | Total number | 14 | 22 | 10 | 41 | 9 | 96 |
| | | | Number of determination cases | 14 | 15 | 9 | 29 | 5 | 72 |
| | | | Number of correct answers | 14 | 15 | 9 | 29 | 5 | 72 |
| | | | Precision | 1.000 | 1.000 | 1.000 | 1.000 | 1.000 | 1.000 |
| | | | Recall | 1.000 | 0.682 | 0.900 | 0.707 | 0.556 | 0.750 |
| | | | F-measure | 1.000 | 0.811 | 0.947 | 0.829 | 0.714 | 0.857 |

Table 6. Result of detecting dangerous objects with different resolutions

| Video Resolution | Fallen leave | Gravel | Manhole | Bump | Wet road surface |
|------------------|---|---|---|--|---|
| Full HD |  |  |  |  |  |
| 4K |  |  |  |  |  |

3.4. Experiment 3: Verification of versatility for different versions of YOLO

In Experiment 2, the dangerous object detection model is generated for two types of versions: YOLOv5 and YOLOv8 to verify the versatility of the method in the case of different versions of YOLO.

Table 8 shows the experimental result of Experiment 3, and Table 9 shows an example of the results of detecting dangerous objects. The overall F-measure is 0.897 for YOLOv5 and 0.874 for YOLOv8, which indicate that the dangerous object detection method is capable of dangerous objects on the road surface for the most part. The detection result indicates the tendency that YOLOv8 is capable of detect dangerous objects on the road surface located at a distance better than YOLOv5. However, YOLOv8 sometimes detected a wet road surface erroneously as a manhole. The detection result shown in Table 10 suggests that its cause can be considered that the pattern of the wet road surface

is similar to the manhole. In addition, focusing on the gravel for which the F-measure with YOLOv8 is lower than that with YOLOv5, it is made clear that the recall ratio of the gravel is low with YOLOv8, and that there are more failures in detection than other dangerous objects. Just as in Experience 2, its cause can be considered the difference in color of the gravel. Since this occurs due to differences in weather conditions as shown in Table 11, we plan to advance the method by increase the learning data under diverse environments in the future.

The results of experiments 1 to 3 indicate that there is little difference among the overall F-measure when applying the dangerous object detection method to the video images shot with 360-degree cameras under different conditions as to the types of cameras, resolutions, and YOLO versions, which proves the versatility of the proposed dangerous object detection method. Furthermore, assuming its utilization in the actual sites on different dates or under different weather conditions, the fact that the detection accuracy was equal to or higher than 0.85 in different dates and under different weather conditions in this study indicates that this dangerous object detection method is useful.

Table 7. Examples of success and failure for the results of detecting dangerous objects

| Dangerous objects | Success | Failure |
|-------------------|---|--|
| Gravel |  |  |
| Bump |  |  |
| Wet road surface |  |  |

Table 8. Experimental result of Experiment 3

| Camera | Video resolution | YOLO | Dangerous objects | Fallen leave | Gravel | Manhole | Bump | Wet road surface | Total |
|----------|------------------|------|-------------------------------|--------------|--------|---------|-------|------------------|-------|
| THETA SC | Full HD | v8 | Total number | 20 | 24 | 11 | 49 | 11 | 115 |
| | | | Number of determination cases | 19 | 17 | 10 | 37 | 8 | 91 |
| | | | Number of correct answers | 19 | 17 | 10 | 36 | 8 | 90 |
| | | | Precision | 1.000 | 1.000 | 1.000 | 0.973 | 1.000 | 0.989 |
| | | | Recall | 0.950 | 0.708 | 0.909 | 0.735 | 0.727 | 0.783 |
| | | | F-measure | 0.974 | 0.829 | 0.952 | 0.837 | 0.842 | 0.874 |

Table 9. Result of detecting dangerous objects with different versions of YOLO

| YOLO | Fallen leave | Gravel | Manhole | Bump | Wet road surface |
|------|---|---|--|---|---|
| v5 |  |  |  |  |  |
| v8 |  |  |  |  |  |

Fundamental Study on Detection of Dangerous Objects on the Road Surface
Leading to Motorcycle Accidents Using a 360-degree Camera
Inoue, H. and Nakasuji, Y.

Table 10. Example of erroneous detection of the wet road surface

| Correct | Error | Detection result with YOLOv8 |
|------------------|---------|--|
| Wet road surface | Manhole |  |

Table 11. Shot images of dangerous objects under different weather conditions

| Weather | Fair Weather | Rain |
|---------|---|---|
| Gravel |  |  |

4. Conclusion

In this study, we verified the versatility of the method to detect dangerous objects on the road surfaces including fallen leaves, gravel, manholes, bumps, and wet road surfaces. In the demonstration experiments, we applied the dangerous object detection method to the video images shot under respective conditions for the 360-degree camera (THETA SC and THETA V), resolutions (full HD and 4K), and YOLO versions (YOLOv5 and YOLOv8) to evaluate the precision ratio, recall ratio, and F-measure. As a result of demonstration experiments, it was found that there is little difference in the F-measure under different conditions such as types of cameras, resolution, and versions of YOLO, and consequently it is capable of detecting dangerous objects on the roads for the most part.

In the future, we plan to improve its accuracy by increasing the learning data under a variety of environments to deal with a problem of detection errors through repeated verification under different environments. We also aim to decrease the number of motorcycle accidents by detecting the factors leading to motorcycle accidents with additional information about the drivers.

Funding

This research received no external funding.

Conflicts of Interest

The authors declare no conflict of interest.

References

- Inoue, H., et al. (2023). Research for detecting dangerous objects leading to overturning of motorcycles using deep learning. *Proceedings of the 85th National Convention of IPSJ*, 85(1), 965–966.
- Inoue, H., et al. (2024). Research for Detecting Dangerous Leading to Motorcycle Accident Using 360 Degree Camera. *Proceedings of the 86th National Convention of IPSJ*, 86(1), 2-351–2-352.
- Nikkei xTECH, Hitachi Astemos aims to commercialize ADAS for motorcycles by 2028. (2024). <https://xtech.nikkei.com/atcl/nxt/column/18/02594/102800022/>
- Senoo, D., et al. (2017). Development of motor-and-bicycle anti roll-down system. *The Proceedings of the Transportation and Logistics Conference*, 26. <https://doi.org/10.1299/jsmetld.2017.26.1104>
- Tokyo Metropolitan Police Department. (2024). Motorcycle traffic fatality statistics (through 2023). https://www.keishicho.metro.tokyo.lg.jp/kotsu/jikoboshi/nirinsha/2rin_jiko.html

Special Issue: Measurement, control, and analysis of motion using ICT and AI
Article

Wildlife Approach Detection Using a Custom-Built Multimodal IoT Camera System with Environmental Sound Analysis

Ryo Tochimoto¹, Katsunori Oyama², Kazuki Nakamura²

¹ Graduate School of Computer Science, Nihon University, 1 Nakagawara, Tamuramachi Tokusada, Koriyama, Fukushima 963-8642, Japan

² Department of Computer Science, College of Engineering, Nihon University, 1 Nakagawara, Tamuramachi Tokusada, Koriyama, Fukushima 963-8642, Japan

Abstract

This paper presents a custom-built IoT camera system designed for recognizing wild animal approaches, where data transmission and power consumption are critical concerns in resource-constrained outdoor settings. The proposed method involves the spectral analysis on both infrared and environmental sound data before uploading images and videos to the remote server. Experiments, including battery endurance tests and wildlife monitoring, were conducted to validate the system. These results showed that the system minimized false positives caused by environmental factors such as wind or vegetation movement. Importantly, adding frequency features from audio waveforms that capture sounds including wind noise and footsteps led to an improvement in detection accuracy, which increased the AUC from 0.894 to 0.990 in Random Forest (RF) and from 0.900 with infrared sensor data alone to 0.987 in Logistic Regression (LR). These findings contribute to applications in wildlife conservation, agricultural protection, and ecosystem monitoring.

Keywords: Wildlife approach detection; Environmental sound analysis; Low-power IoT systems.

1. Introduction

Crop damage caused by wildlife remains a serious social issue, as it leads to certain vulnerable species becoming uncultivable (Ministry of Agriculture, Forestry and Fisheries, 2023). Monitoring animal behavior is a critical first step in controlling wildlife pests; however, tracking free-roaming animals such as wild boars within a camera's field of view is inherently challenging. Fixed cameras equipped with human detection sensors in the real-world outdoor settings often experience false detections due to noise generated by swaying vegetation, resulting in an excessive number of unnecessary images being uploaded to a cloud server. Additionally, battery exhaustion is a persistent issue when installing cameras in remote, mountainous areas where securing a power source is impractical. Even when animals are captured within the camera's field of view, it is often challenging to interpret situations involving an approaching animal based solely on images. Proper interpretation and appropriate actions require considering the behavioral and environmental contexts with those the detection results (Chang et al., 2009; Wu et al., 2023). Environmental contexts can include various audible events such as footsteps, wind, and vegetation movement. These environmental contexts have the potential to indirectly identify animal presence or movement.

Most wildlife monitoring systems adopt either bioacoustic monitoring or image processing techniques. Bioacoustic monitoring is effective for detecting animals through vocalizations, enabling the monitoring of species such as frogs and deer (McLoughlin et al., 2019; LOSTANLEN et al., 2019). However, this approach assumes that animals vocalize and that environmental noise is minimal. On the other hand, YOLO (You Only Look Once) models are widely used for their high accuracy and real-time performance in image processing (Li et al., 2023; Ma et al., 2024). Yet, both methods

Received: 22 November 2024, Revised: 18 January 2025, Accepted: 26 January 2025, Published: 26 March 2025

* Correspondence: oyama.katsunori@nihon-u.ac.jp

Publisher's Note: JOURNAL OF DIGITAL LIFE. stays neutral with regard to jurisdictional claims in published maps and institutional affiliations.



Copyright: © SANKEI DIGITAL INC. Submitted for possible open access publication under the terms and conditions of the Creative Commons Attribution (CC BY) license (<https://creativecommons.org/licenses/by/4.0/>).

face challenges in terms of energy consumption and data transmission when implemented on resource-constrained devices such as the Raspberry Pi.

Existing wildlife monitoring solutions include commercial trail cameras from SPYPOINT and Moultrie. These products often employ AI-based filters to mitigate false triggers and can upload images via Wi-Fi or cellular networks. However, they primarily rely on PIR sensors and image-based analysis before uploading images, which may lead to increased false positives in windy or densely vegetated environments (SPYPOINT, n.d.; Moultrie Mobile, n.d.). In contrast, our approach integrates both infrared and audio frequency features (e.g., wind noise, footsteps) to reduce false positives more effectively, especially under challenging outdoor conditions.

Our study is among the first to indicate that combining infrared and audio data efficiently improves detection accuracy, which not only conserves energy and reduces data transmission but also extends operational longevity in remote wildlife monitoring applications. We have been developing custom-built IoT camera systems based on Raspberry Pi Zero 2 by integrating infrared and audio sensors for monitoring animal movements (Tochimoto et al., 2023). Unlike existing systems, our multimodal approach uniquely employs spectral analysis on both infrared and environmental sound data collected from the surroundings to minimize false positives caused by environmental factors such as wind or vegetation movement. This study primarily targets medium to large animals, such as wild boars, deer, monkeys, and raccoons, as these species are known to cause significant damage to crops.

This paper presents the experimental evaluations of our multimodal IoT camera system, conducted at two distinct locations in Japan. In 2023, we tested the system in an open space near a residential area to assess its performance under moderate environmental conditions by focusing on the system’s ability to reduce false detections in a relatively controlled setting. Subsequently, from May to July 2024, we deployed the system in a mountainous region of Katsurao Village, Fukushima, Japan, where the environment introduced challenges such as dense vegetation and variable weather conditions.

2. Multimodal IoT Camera System

2.1. Hardware Design and Implementation

The IoT camera system developed in this study is based on the Raspberry Pi Zero 2 to integrate various sensors such as an infrared sensor, infrared camera, Raspberry Pi camera, and audio microphone. Two types of the multimodal camera systems were designed for this research: The first model, **Version 1 (Ver 1)**, uses a small mobile battery paired with a solar panel, while the second model, **Version 2 (Ver 2)**, employs a 12 V lithium-ion battery to support extended continuous operation. In Ver 1, the system features a solar panel that recharges the battery using sunlight. Ver 2, on the other hand, has a larger battery capacity than Ver 1 and is also equipped with an infrared camera to enable nighttime detection. Both models are housed in custom-designed cases created with a 3D printer, which encase all sensors and batteries. The front of the case includes an infrared sensor, a camera, and an audio microphone. Each case is designed to be highly waterproof, with functionality verified through high-pressure shower tests, as shown in Figure 1.

The infrared sensor used in this study is a pyroelectric infrared sensor, PaPIRs (manufactured by Panasonic, long-distance detection type). This sensor is a long-distance detection type with a 12-m range, providing an analog output that enables the collection of time-series data from the surrounding environment for advanced time-series analysis. Our preliminary tests indicate that beyond 12 m, false alarms rise significantly due to environmental factors, which informed our decision to limit the range for improved accuracy and power conservation (Tochimoto et al., 2023). Detection ranges of commercial trail cameras can exceed 15 m, potentially increasing the risk of false positives in dense vegetation. In contrast, we selected a 12 m effective detection radius to balance sensitivity and battery efficiency.

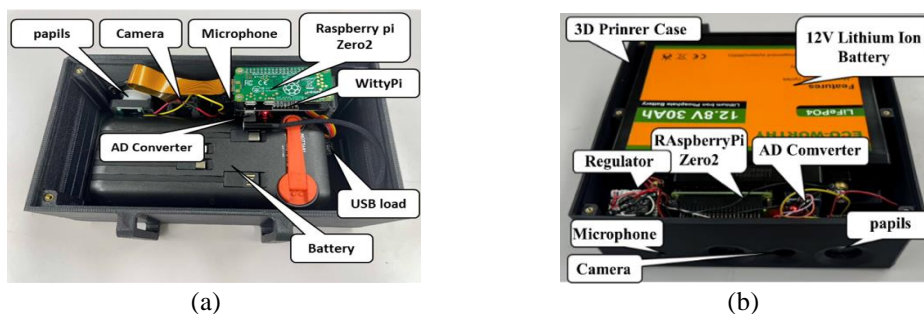


Figure 1: Two Types of Multimodal IoT Camera Systems: (a) the Version 1 (Ver 1) with a Mobile Battery and (b) the Version 2 (Ver 2) with an Extended Battery for Longer Operation.

In addition, an omnidirectional audio microphone, as illustrated in Figure 2, captures environmental audio waveforms, including sounds from rain, wind, and animal vocalizations. Processing this time-series audio data allows the system to classify diverse environmental sounds, during interpreting motion detected by the infrared sensor.

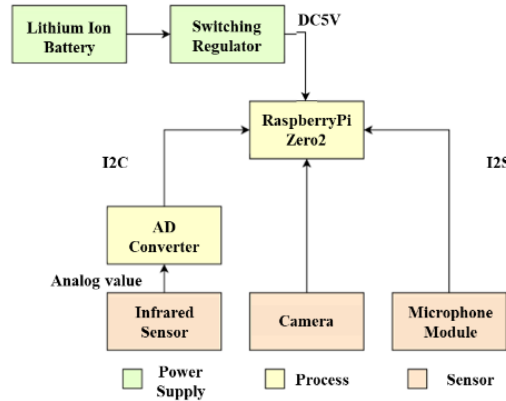


Figure 2: Block Diagram of Ver 2 IoT Camera System

2.2. Software Design and Implementation

This system requires continuous acquisition of infrared data while simultaneously operating the camera and microphone. Multithreading is employed for enabling the concurrent operation of various sensors. Every 0.1 seconds, the system retrieves values from the infrared sensor. As shown in Figure 3 of the system’s sequence diagram, if a reaction is detected, it initiates both the photo capture and audio recording processes as subprocesses to collect data concurrently, while infrared data collection remains uninterrupted. Additionally, creating a cron job on the Raspberry Pi Zero 2, which is a resident program for executing scripts automatically, enables the device to start sensing immediately upon power-on.

The transmission of image data is the heaviest load on server communication. Therefore, to minimize unnecessary image transmissions and improve efficiency in resource-limited environments, such as mountainous areas, the system uses machine learning models locally to assess the likelihood of animal detection before transmission. Only when there is a high probability of detecting an animal does the system transmit relevant data to the remote server.

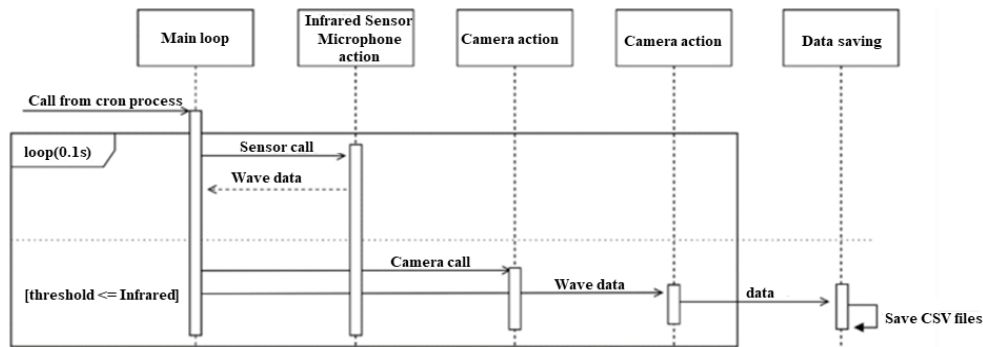


Figure 3: System Sequence for Multithreading Process

3. Methods

3.1. Operation Testing

The multimodal IoT camera system continuously monitors infrared waveforms. The system records images, videos, and audio data to log detected events when the detection threshold is exceeded. The collected infrared waveform data is stored in CSV format hourly, and data retrieval is performed remotely via a 4th Generation Mobile Communication System (4G) connection. Figure 4 illustrates the test setup. A power supply with a solar panel and a 4G router is placed at the center, with the Camera 1 and the Camera 2 representing the IoT camera systems developed and installed for this study. Each IoT camera system is connected via Wi-Fi and can be placed anywhere within a Wi-Fi range of approximately 50 m.

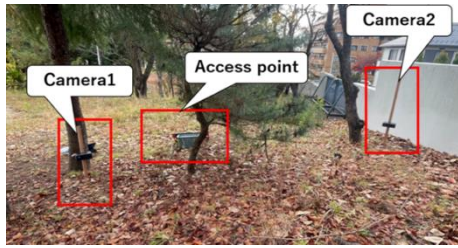
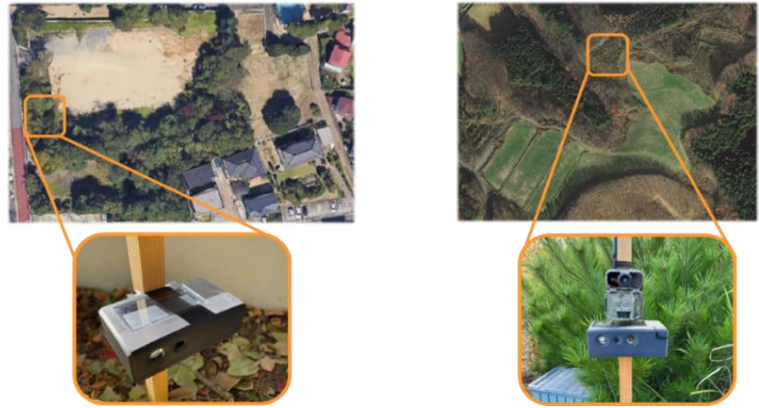


Figure 4: Operation Testing



(a) Open space near a residential area

(b) Mountainous area

Figure 5: Test Sites

3.2. Test Sites and Measured Data

Data collection for this study was conducted at two test sites: (a) an open space near a residential area in April 2023 and (b) a mountainous area in Katsurao Village, Fukushima, Japan, from May to July 2024. Two IoT cameras were installed at each site, with the sensing areas marked as squares in the figures. At both locations, the ground was covered with leaves and grass, and vegetation was within the cameras' field of view. Conducting experiments at two different locations not only provided diverse measured data for model training and testing but also strengthened the reliability of the findings by validating the system under the practical environmental conditions.

Figure 6 shows an example of the infrared and audio waveform data collected per window time. To prepare the data for analysis, the following processing steps were performed. Noise artifacts may occur depending on the recording's start time (as shown in Figure 6), and these can affect the Fourier Transform (FFT) results. Therefore, as part of the audio data preprocessing, the first 0.3 seconds from the start of the recording were removed. Additionally, as preprocessing for the infrared data, a 10-second window was extracted from the point of detection. Next, FFT was applied to the time-series data of the infrared and audio waveforms. By converting these waveforms to the frequency domain for each time window, characteristic features were extracted. Subsequently, the sum and variance of the infrared and audio waveform FFT results were calculated, and labels for successful detection (“Approaching”) or failed detection (“No Approaching”) were added based on the footage captured during detection, creating the dataset for analysis.

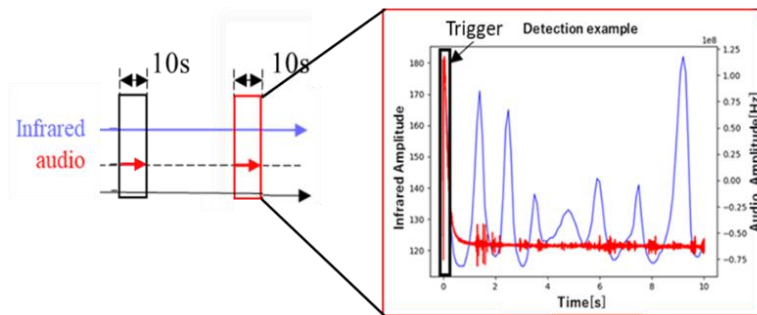


Figure 6: Examples of infrared and audio waveform data collected within a single time window

As shown in Table 1, the first set of columns in the dataset includes the filename, which contains the timestamp and the ground truth label. The subsequent columns (highlighted in red and blue) represent frequency features extracted from the infrared and audio waveforms. The column labeled “sum” indicates the sum of the components within the active frequency bands, “var” represents the variance of those components within the 10-second window, and “mean” represents their mean value. The “0.0 Hz” column indicates the spectral power of the frequency band between 0 Hz and 0.1 Hz.

Table 1: Example Dataset with Frequency Features from Infrared and Audio Waveforms

| time | correct | Infrared | | | | | | | | audio | | | | | |
|-----------------|---------|----------|------|------|-------|-------|-------|-------|------|-------|------|------|--------|--------|--------|
| | | sum | var | mean | 0.0Hz | 0.1Hz | 4.9Hz | 5.0Hz | sum | var | 0k | 1k | 22k | 23k | 24k |
| 20230310_152236 | 1 | 418 | 1384 | 134 | 268 | 6.21 | 0.56 | 0.56 | 0.46 | 0 | 0.05 | 0 | 0.0014 | 0.0016 | 0.0017 |
| 20230310_152331 | 1 | 389 | 1328 | 131 | 262 | 6.36 | 0.54 | 0.54 | 0.46 | 0 | 0.1 | 0.01 | 0.001 | 0.0011 | 0.0012 |
| 20230310_152356 | 1 | 367 | 1312 | 130 | 260 | 5.05 | 0.51 | 0.51 | 0.15 | 0 | 0.04 | 0 | 0.0003 | 0.0002 | 0.0002 |
| 20230310_152514 | 1 | 439 | 1485 | 139 | 277 | 11 | 0.46 | 0.46 | 0.26 | 0 | 0.04 | 0 | 0.0007 | 0.0007 | 0.0007 |
| 20230318_155753 | 0 | 287 | 1198 | 124 | 248 | 1.81 | 0.38 | 0.38 | 0.08 | 0 | 0.04 | 0 | 0.0002 | 0.0003 | 0.0003 |
| 20230321_080818 | 1 | 357 | 1257 | 134 | 267 | 7.6 | 0.23 | 0.23 | 0.06 | 0 | 0.04 | 0 | 0.0001 | 0.0001 | 0.0001 |

3.3. PCA Method

To extract spectral features in the frequency domain, a dataset was generated where the spectral power for each frequency band served as a feature. The infrared waveform was segmented into units of either 0.1 Hz or 1 Hz, while the audio waveform was divided into units of 1 kHz, 2 kHz, and 4 kHz to assess their impact on detection accuracy. This segmentation, however, resulted in high-dimensional data. As illustrated in Table 2, six datasets (Dataset1 through Dataset6) were created based on these configurations. To manage the high dimensionality, Principal Component Analysis (PCA) was employed for dimensionality reduction, and detection accuracy was evaluated both with and without PCA.

Table 2: Column Specifications for Each Dataset Based on Infrared and Audio Waveforms

| Dataset | Infrared Waveform | Audio Waveform | Infrared Columns | Audio Columns |
|----------|-------------------|----------------|------------------|---------------|
| Dataset1 | 0.1 Hz | 1 kHz | 54 | 27 |
| Dataset2 | 0.1 Hz | 2 kHz | 54 | 14 |
| Dataset3 | 0.1 Hz | 4 kHz | 54 | 8 |
| Dataset4 | 1 Hz | 1 kHz | 10 | 27 |
| Dataset5 | 1 Hz | 2 kHz | 10 | 14 |
| Dataset6 | 1 Hz | 4 kHz | 10 | 8 |

3.4. Machine Learning Method

Two machine learning models, Random Forest (RF) and Logistic Regression (LR), were evaluated to compare the performance of the system using infrared and audio waveform data. Additionally, two approaches were tested to maximize model accuracy: one applied dimensionality reduction via Principal Component Analysis (PCA) to extract key features, while the other used all features without PCA.

In the PCA-applied approach, the reduced-dimension data were input into the model. In contrast, in the non-PCA approach, all features were used directly without dimensionality reduction. This comparison aimed to evaluate improvements in training efficiency achieved through dimensionality reduction and to analyze performance differences between models using all features and those using reduced features.

To address class imbalances in the training data, the Synthetic Minority Over-sampling Technique (SMOTE) was applied, and a stratified 5-fold cross-validation was performed. This approach enables a balanced training dataset by reducing the effects of class imbalance during training. The test data were used without additional processing, and model performance was assessed using the Area Under the Curve (AUC) metric.

4. Results

4.1. Operation Verification Results

Table 3 shows the predicted and actual operating days of the system. In this experiment, two types of systems were tested: The Ver 1 as the mobile battery model and the Ver 2 as the lithium-ion battery model, with the operating time of each system measured.

In the Ver 1, power consumption was approximately 1 W, with a battery capacity of 144 Wh. Although the predicted operating time was 144 hours, the result showed the system operated continuously for 168 hours, which is likely extended by the solar panel recharging the battery. In the Ver 2, with a battery capacity of 360 Wh (12 V) and a power consumption of 1 W, the estimated operating time was 360 hours. The actual operating time was 336 hours, approximately two weeks, and was close to the expected result. Both models demonstrated that power consumption and environmental conditions influenced operating time, with the Ver 2 proving more suitable for stable, long-term operation.



Figure 7: Images Captured During Detection Events

Table 3: Operational Records and Detection Counts

| Version | estimated operation time | Number of working hour | Number of detections |
|---------|--------------------------|------------------------|----------------------|
| Ver 1 | 168 | 168 | 59 |
| Ver 2 | 360 | 336 | 66 |

4.2. Data Collection Results

At the first test site, 267 data instances were collected, including 13 instances with animals and 254 without. At the second test site in Katsurao Village, 2,087 data instances were collected, with 109 containing animals and 1,978 without. The images shown in Figure 7 below provide examples of actual camera captures. At the first site, data included images of humans and cats, while at the second test site, images included humans, dogs, raccoons, and wild boars. When no animals were present, the cameras occasionally recorded empty scenes triggered mistakenly by swaying vegetation due to wind.

4.3. PCA Results

To improve the performance of the machine learning model, feature selection was conducted to identify the most relevant columns (features). Given the high dimensionality of the current dataset, a Principal Component Analysis (PCA) was applied to reduce dimensionality and extract the most important features. For each dataset, principal components were selected until the cumulative contribution rate reached 90%, and the contribution of each feature to

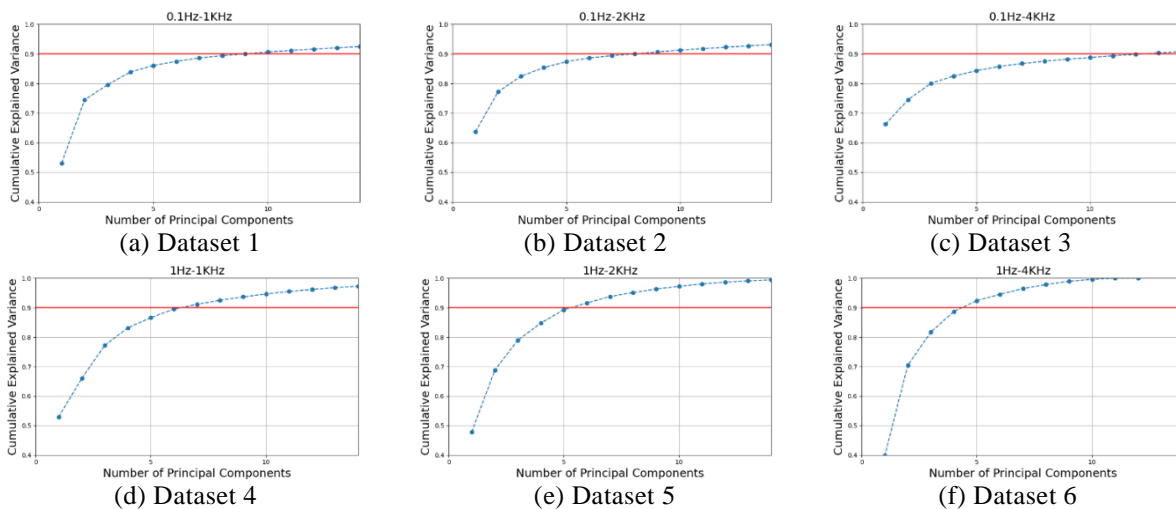


Figure 8: Cumulative Contribution Rate

these components was evaluated. Figure 8 shows the cumulative contribution rates of PCA for each dataset, while Table 4 lists the top 10 contributing features in Principal Components 1 (PC1) to 5 (PC5) for each dataset. Based on the analysis of the contributing features and the video data, the PC1 likely corresponds to swaying vegetation, and the PC2 to environmental noise such as wind.

Table 4: Contribution Rate (Example from Dataset1)

| PC1 (Swaying Vegetation) | | PC2 (Environmental Noise, e.g., Wind) | | PC3 (Animal Vocal Characteristics) | | PC4 (Slow Movements of Animals) | | PC5 (Environmental Noise, e.g., Wind) | |
|--------------------------------|-------|---|-------|--|-------|---------------------------------------|-------|---|-------|
| 2.7 Hz | 0.149 | 10 kHz | 0.228 | 2 kHz | 0.175 | 0.4Hz | 0.267 | 14 kHz | 0.208 |
| 2.5 Hz | 0.148 | 9 kHz | 0.227 | 1 kHz | 0.174 | 0.6Hz | 0.242 | 13 kHz | 0.186 |
| 2.1 Hz | 0.148 | 11 kHz | 0.224 | 3 kHz | 0.174 | 0.5Hz | 0.235 | 15 kHz | 0.175 |
| 2.2 Hz | 0.148 | 7 kHz | 0.223 | 0.4 Hz | 0.170 | 0.9Hz | 0.193 | 9 kHz | 0.092 |
| 2.8 Hz | 0.148 | 8 kHz | 0.223 | 0.6 Hz | 0.159 | 0.7Hz | 0.187 | 11 kHz | 0.081 |
| 3.0 Hz | 0.148 | 6 kHz | 0.221 | 4 kHz | 0.148 | 0.1Hz | 0.178 | 10 kHz | 0.078 |
| 2.3 Hz | 0.148 | 12 kHz | 0.216 | 0.5 Hz | 0.147 | 0.3Hz | 0.169 | 12 kHz | 0.074 |
| 2.4 Hz | 0.148 | 5 kHz | 0.216 | 0.3 Hz | 0.145 | 23 kHz | 0.168 | 16 kHz | 0.063 |
| 3.1 Hz | 0.148 | 16 kHz | 0.213 | 6 kHz | 0.142 | 20 kHz | 0.162 | 4.7 Hz | 0.059 |
| 3.2 Hz | 0.147 | 13 kHz | 0.213 | 7 kHz | 0.138 | 24 kHz | 0.160 | 4.6 Hz | 0.057 |

For the infrared waveform, low-frequency components such as 2–3 Hz and 0.1–1 Hz made substantial contributions across multiple datasets, as they appear to reflect responses to animal approaches and environmental fluctuations. In the audio waveform, high and mid-frequency components, specifically in the 10–11 kHz and 1–3 kHz ranges, were also significant, and may correspond to noise and animal-related sounds in the audio signal. The variance of the audio waveform ("var" in the audio category, as shown in Table 1) contributed strongly across multiple datasets as a key indicator of variations in environmental and animal sounds.

4.4. Machine Learning Results

Table 5 shows the 5-fold stratified cross-validated AUC scores and the independent test AUC scores of the RF model with and without PCA. These cross-validated AUC scores are averaged over a stratified 5-fold procedure with SMOTE applied to the training split (80 %), while the test AUC scores represent performance on a separate hold-out set (20 %) without further oversampling. From the results, the combination of infrared 0.1 Hz and audio 4 kHz achieved the highest AUC score of 0.990. When PCA was applied, the combination of infrared 0.1 Hz and audio 1 kHz recorded a high AUC score of 0.986. These results indicate that for lower-dimensional data, high performance can be achieved even without using PCA.

Table 6 presents the AUC results of the LR model with and without PCA. When PCA was applied, the combination of infrared 0.1 Hz and audio 1 kHz achieved an AUC of 0.987 with PCA, which nearly matched the 0.985 AUC without PCA. This finding indicates a slight improvement in model accuracy when PCA is applied to higher-dimensional data.

The Random Forest (RF) model maintained high performance regardless of whether PCA was applied or not. It is noteworthy that the combination of infrared 0.1 Hz and audio 4 kHz achieved the highest AUC score of 0.990 without PCA. Furthermore, even with PCA applied, high AUC scores of 0.986 were recorded for the combinations of infrared 0.1 Hz and audio 1 kHz, as well as infrared 0.1 Hz and audio 2 kHz. These results indicate that the RF model can achieve sufficient performance without PCA, while PCA proves to be effective for high-dimensional data.

On the other hand, applying PCA to low-dimensional data was found to reduce performance. For instance, in the Logistic Regression (LR) model, the combination of infrared 1 Hz and audio 4 kHz achieved an AUC score of 0.950 without PCA, which dropped to 0.877 when PCA was applied. This demonstrates that PCA is not always effective in every scenario.

Table 5: Random Forest AUC with and without PCA

| Infrared | Audio | PCA | Cross-Validated AUC (Mean:0.98) | Test AUC (Mean:0.96) |
|----------|-------|-----|---------------------------------|----------------------|
| 0.1 Hz | 4 kHz | No | 0.952 | 0.990 |
| 1 Hz | 1 kHz | No | 0.984 | 0.989 |
| 0.1 Hz | 1 kHz | Yes | 0.990 | 0.986 |
| 0.1 Hz | 2 kHz | Yes | 0.992 | 0.986 |
| 1 Hz | 4 kHz | No | 0.972 | 0.984 |
| 1 Hz | 2 kHz | No | 0.982 | 0.982 |
| 0.1 Hz | 1 kHz | No | 0.973 | 0.980 |
| 0.1 Hz | 2 kHz | No | 0.984 | 0.979 |
| 1 Hz | 2 kHz | Yes | 0.983 | 0.915 |
| 1 Hz | 1 kHz | Yes | 0.975 | 0.906 |
| 1 Hz | 4 kHz | Yes | 0.981 | 0.895 |
| 0.1 Hz | 4 kHz | Yes | 0.991 | 0.874 |

Table 6: Logistic Regression AUC with and without PCA

| Infrared | Audio | PCA | Cross-Validated AUC (Mean:0.93) | Test AUC (Mean:0.94) |
|----------|-------|-----|---------------------------------|----------------------|
| 0.1Hz | 1KHz | Yes | 0.961 | 0.987 |
| 1Hz | 1KHz | No | 0.941 | 0.987 |
| 1Hz | 2KHz | No | 0.955 | 0.985 |
| 0.1Hz | 2KHz | Yes | 0.961 | 0.980 |
| 0.1Hz | 1KHz | No | 0.931 | 0.972 |
| 0.1Hz | 2KHz | No | 0.925 | 0.965 |
| 1Hz | 4KHz | No | 0.893 | 0.950 |
| 0.1Hz | 4KHz | No | 0.892 | 0.922 |
| 1Hz | 1KHz | Yes | 0.946 | 0.881 |
| 1Hz | 2KHz | Yes | 0.918 | 0.879 |
| 1Hz | 4KHz | Yes | 0.884 | 0.877 |
| 0.1Hz | 4KHz | Yes | 0.922 | 0.847 |

4.5. Variable Importance in Machine Learning Models

The important frequency bands were identified using the Random Forest (RF) and Logistic Regression (LR). As shown in Tables 7 and 8, the analysis focused on the data with the highest AUC values among those without PCA, specifically the combination of infrared 0.1 Hz and audio 1 kHz, to identify key frequency bands. Table 7 summarizes the feature importance from the RF, while Table 8 shows the coefficients from the LR.

In the RF results, the 5 kHz frequency band showed the highest importance (0.079), followed by 11 kHz, 13 kHz, and 10 kHz. These results indicate that high-frequency audio data plays a significant role in animal detection. In contrast, the importance of infrared data was relatively low, and high-frequency audio data contributes substantially to the model's predictions.

The RF model prioritized high-frequency audio bands (e.g., 5 kHz, 11 kHz, 13 kHz), and it suggests that audio data plays an important role in detecting animal vocalizations and environmental noise. The LR model, however, placed greater emphasis on low-frequency infrared data, such as 0.7 Hz and 1.7 Hz. This suggests that infrared data is more effective for identifying slow animal movements and environmental fluctuations.

Table 7: Random Forest Feature Importance

| Feature | Importance | Data Type |
|---------------|------------|-----------|
| 5 kHz | 0.079 | Audio |
| 11 kHz | 0.047 | Audio |
| 13 kHz | 0.045 | Audio |
| 10 kHz | 0.042 | Audio |
| 8 kHz | 0.040 | Audio |
| 9 kHz | 0.040 | Audio |
| 12 kHz | 0.039 | Audio |
| 7 kHz | 0.038 | Audio |
| infrared_mean | 0.036 | Infrared |
| infrared_var | 0.033 | Infrared |
| 6 kHz | 0.033 | Audio |
| 0.5 Hz | 0.032 | Infrared |
| audio_var | 0.032 | Infrared |
| 0.4 Hz | 0.031 | Infrared |
| 2 kHz | 0.029 | Audio |
| 4 kHz | 0.029 | Audio |
| 0.0 Hz | 0.029 | Infrared |
| audio_add | 0.021 | Audio |
| 3 kHz | 0.018 | Audio |
| 1 kHz | 0.018 | Audio |

Table8: Logistic Regression Coefficients

| Feature | Importance | Data Type |
|---------|------------|-----------|
| 2 kHz | 1.83 | Audio |
| 0.7 Hz | 1.79 | Infrared |
| 1.7 Hz | 1.60 | Infrared |
| 15 kHz | 1.44 | Audio |
| 6 kHz | 1.27 | Audio |
| 5.0 Hz | 1.27 | Infrared |
| 13 kHz | 1.18 | Audio |
| 0.4 Hz | 1.10 | Infrared |
| 0.6 Hz | 1.09 | Infrared |
| 4.2 Hz | 1.08 | Infrared |
| 4.5 Hz | 1.08 | Infrared |
| 0.5 Hz | 1.03 | Infrared |
| 5 kHz | 1.03 | Audio |
| 14 kHz | 0.99 | Audio |
| 2.9 Hz | 0.96 | Infrared |
| 10 kHz | 0.80 | Audio |
| 3.5 Hz | 0.80 | Infrared |
| 12 kHz | 0.78 | Audio |
| 1.5 Hz | 0.69 | Infrared |
| 2.4 Hz | 0.67 | Infrared |

4.6. Influence of Audio Waveform

This study assessed the effect of integrating audio waveforms with infrared waveforms on the accuracy of animal approach detection. Models trained with only infrared waveforms were compared to those using both infrared and audio waveforms. As shown in Figure 9, AUC scores for the RF and the LR achieved 0.894 and 0.900, respectively, when using only infrared waveforms. These models using frequency features extracted from infrared waveforms alone achieved a reasonable level of accuracy, although the risk of false positives and missed detections remains. The inclusion of audio frequency features improved the AUC to 0.990 for the RF and 0.987 for the LR. These results are consistent with the cross-validated and test AUC values shown in Tables 5 and 6. From these findings, we confirm that integrating audio waveforms plays an essential role.

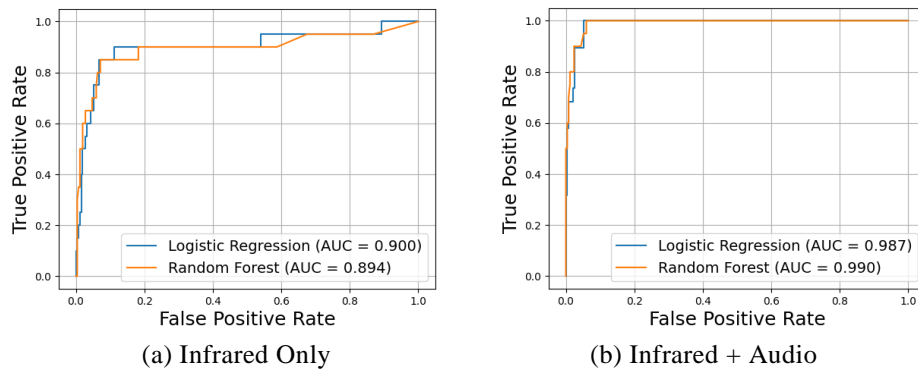


Figure 9: ROC Curves and AUC Comparison Between Infrared Only and Infrared with Audio

Table 9 summarizes selected training results for each model, while Figure 10 illustrates examples of detection under different conditions: **Case 1** (Wild Boar) represents a straightforward scenario where accurate detection was achieved with both infrared-only and infrared-plus-audio data. **Case 2** (Human) is the case of a false negative in the infrared-only approach, where minimal movement between frames caused the model to misclassify the instance as “no approaching.” The addition of frequency features extracted from audio waveforms allowed the detection of human voices, resulting in a correct classification of “approaching.” Lastly, **Case 3** (No Detection) is the case of a false positive with the infrared-only approach, where swaying vegetation was misclassified as “approaching.” The addition of frequency features from audio waveforms helped identify wind noise for the correct classification of “no approaching.”



Figure 10: Comparison of Detection Cases Under Various Conditions

Table 9: Comparison of Detection Results: Infrared Only vs. Infrared with Audio

| Case | Ground Truth | LR_IR Only | RF_IR Only | LR_IR+Audio | RF_IR+Audio |
|----------------------|--------------|------------|------------|-------------|-------------|
| Case1 (Wild Boar) | P | P | P | P | P |
| Case2 (Human) | P | N | N | P | P |
| Case3 (No Detection) | N | P | P | N | N |

LR: Random Forest RF: Random Forest IR: Infrared

5. Discussion

This study proposed a multimodal detection system that integrates frequency features from infrared and audio waveforms. The analysis confirmed that frequency bands identified through FFT analysis are important for identifying animal movements and mitigating false detections. Infrared waveforms provided low-frequency components, such as 2–3 Hz (swaying vegetation) and 0.1–1 Hz (slow movements of animals or humans), which were particularly significant, as highlighted in Section 4.5.

Similarly, audio waveforms contributed mid-to-high frequency bands, such as 1–3 kHz (human voices or animal vocalizations) and 10–11 kHz (environmental noise like wind). These features, as demonstrated in Section 4.6, significantly improved the AUC for both the RF and LR models. The integration of audio data effectively reduced errors caused by environmental factors, such as vegetation sway.

Experiments in this study were conducted at two distinct test sites: a residential area and a mountainous region. These environments invited unique challenges such as varying vegetation density and weather conditions for validating the robustness and adaptability of the proposed system. By effectively reducing false detections through the integration of infrared and audio data, the proposed system shows considerable promise for real-world applications.

In this paper, we evaluated both Random Forest (RF)—a non-linear ensemble method—and Logistic Regression (LR)—a linear model—to compare their performance in our system. Based on the analysis in Section 4.4, RF consistently delivers robust, high performance on multimodal (infrared + audio) and higher-dimensional datasets across diverse frequency-segmentation settings. Meanwhile, LR can perform nearly as well, particularly when paired with effective PCA for high-dimensional data, though it is more sensitive to feature engineering. Accordingly, we recommend RF as an immediate, stable solution, whereas LR (and other linear models) may be preferable in scenarios where interpretability is a priority, especially when identifying which features contribute most to the detection results.

Nevertheless, this study has certain limitations. The system relies on camera-based data collection for ground truth labels, limiting detection to the camera’s field of view and introducing a risk of missed detections outside this range. Additionally, as noted in Section 3.1, the Raspberry Pi hardware brought challenges in power consumption, constraining operational time even with a larger battery. Overcoming these challenges will be essential for improving the system’s practicality and enabling its deployment in diverse real-world scenarios.

6. Conclusion and Future Challenges

This study proposed and evaluated a multimodal detection system that integrates frequency features from infrared and audio waveforms to improve the accuracy of animal approach detection. By applying FFT to these waveform types, the system identified critical frequency bands that contribute to the detection accuracy. Infrared waveforms captured low-frequency components, such as 0.1–1 Hz and 2–3 Hz, linked to animal movements and environmental fluctuations. Audio waveforms provided mid-to-high frequency features, such as 1–3 kHz and 10–11 kHz, capturing animal vocalizations, footsteps, and environmental noise. This integration proved highly effective by improving the AUC for RF and LR models to 0.990 and 0.987, respectively. From these results, we confirm that combining infrared and audio data is the key strategy for practical application of the multimodal IoT camera systems.

Future efforts should focus on improvement of robustness and reliability by adapting the system to diverse environmental conditions. Expanding the dataset to include more balanced samples representing various animal species is necessary for refining detection performance. Additionally, optimizing machine learning models for real-time processing and addressing energy efficiency will enable long-term deployment in resource-constrained outdoor environments. By addressing these challenges, the proposed system has the potential to significantly advance wildlife management, mitigate crop damage, and contribute to broader environmental conservation efforts.

Author Contributions

Conceptualization, K.O., and K.N.; methodology, K.O.; software, R.T.; validation, R.T., K.O., and K.O.; formal analysis, R.T.; investigation, R.T. and K.O.; data curation, R.T.; writing—original draft preparation, R.T.; writing—review and editing, K.O.; visualization, R.T.; supervision, K.O.; project administration, K.O. and K.N.

Conflicts of Interest

The authors declare no conflict of interest.

Acknowledgements

We gratefully acknowledge the Fukushima Innovation Coast Framework Promotion Project, which provided a strong foundation for collaboration and innovation in developing the IoT camera systems used in this research.

References:

- Chang, C. K., Jiang, H., Ming, H., & Oyama, K. (2009). Situ: A situation-theoretic approach to context-aware service evolution. *IEEE Transactions on Services Computing*, 2(3), 261–275. <https://doi.org/10.1109/TSC.2009.21>
- Li, S., Zhang, H., & Xu, F. (2023). Intelligent detection method for wildlife based on deep learning. *Sensors*, 23(19), 9669. <https://doi.org/10.3390/s23249669>
- Lostanlen, V., Salamon, J., Farnsworth, A., Kelling, S., & Bello, J. P. (2019). Robust sound event detection in bioacoustic sensor networks. *PLOS ONE*, 14(10), e0214168. <https://doi.org/10.1371/journal.pone.0214168>
- Ma, Z., Dong, Y., Xia, Y., Xu, D., Xu, F., & Chen, F. (2024). Wildlife real-time detection in complex forest scenes based on YOLOv5s deep learning network. *Remote Sensing*, 16(8), 1350. <https://doi.org/10.3390/rs16081350>
- McLoughlin, M. P., Stewart, R., & McElligott, A. G. (2019). Automated bioacoustics: Methods in ecology and conservation and their potential for animal welfare monitoring. *Journal of the Royal Society Interface*, 16(150), 20190225. <https://doi.org/10.1098/rsif.2019.0225>
- Ministry of Agriculture, Forestry and Fisheries. Summary of the Annual Report on Food, Agriculture and Rural Areas in Japan (FY2023). https://www.maff.go.jp/e/data/publish/Annual_Report/AnnualReportonFoodAgricultureandRuralAreas_FY2023.pdf
- Moultrie Mobile. (n.d.). Why am I getting so many pictures or pictures with nothing in them? <https://support.moultriemobile.com/hc/en-us/articles/1500006416442-Why-am-I-getting-so-many-pictures-or-pictures-with-nothing-in-them>
- SPYPOINT. (n.d.). Best practices for resolving false triggers. <https://spypoint.onsitesupport.io/knowledge-base/article/best-practices-for-resolving-false-triggers>
- Tochimoto, R., Oyama, K., & Ming, H. (2023). Development of an IoT camera system for situation recognition of approaching animals. In *Proceedings of the IEEE International Conference on Software Services Engineering (SSE)* (pp. 1–6). <https://doi.org/10.1109/SSE60056.2023.00047>
- Wu, J., Feng, Y., & Chang, C. K. (2023). Sound of daily living identification based on hierarchical situation audition. *Sensors*, 23(7), 3726. <https://doi.org/10.3390/s23073726>

Special Issue: Measurement, Control, and Analysis of Motion Using ICT and AI
Article

Research on Indoor Self-Location Estimation Technique Using Similar Image Retrieval Considering Environmental Changes

Masaya Nakahara ¹, Yoshinori Tsukada ², Yoshimasa Umehara ³ and Shota Yamashita ⁴

¹ Faculty of Information Science and Arts, Osaka Electro-Communication University, 1130-70 Kiyotaki, Shijonawate-shi, Osaka 575-0063, Japan

² Faculty of Engineering, Reitaku University, 2-2-1 Hikarigaoka, Kashiwa-shi, Chiba 277-8686, Japan

³ Faculty of Business Administration, Setsunan University, 17-8 Ikedanakamachi, Neyagawa-shi, Osaka 572-8508, Japan

⁴ Graduate School of Information Science and Arts, Osaka Electro-Communication University, 1130-70 Kiyotaki, Shijonawate-shi, Osaka 575-0063, Japan

Abstract

In Japan, the shortage of human resources due to the declining birthrate and aging population is becoming a social problem. Particularly in the security industry, the irregular working hours and associated risks are making it increasingly challenging to secure workers. This has led to a rise in use of security systems that utilize security cameras and drones. However, in factories and other buildings with a lot of equipment and intricate structures, there is the problem of blind spots caused by occlusion. This situation necessitates the use of automated drone patrols, and a problem arises when self-position estimation fails in areas where acquiring feature points is difficult, such as corridors. To solve these problems, in a previous study, we devised a technique for position estimation using a method that can calculate similarity based on changes in the distribution of color information across the entire image. In this study, we propose a method that can cope with environmental changes caused by object movement while combining feature point-based methods.

Keywords: *automated patrol, drone, position estimation, image search*

1. Introduction

In Japan, the shortage of human resources has become a social problem due to the declining birthrate and aging population. This has had a serious effect on the security industry because of the irregular hours of work, the danger involved in responding to suspicious persons, and the large number of personnel required to patrol large facilities (Ministry of Health, Labour and Welfare, 2024). These factors necessitate the development of security systems that utilize security cameras and drones as a solution to the shortage of human resources. However, security systems that utilize security cameras face several challenges. For example, when monitoring areas with many pieces of equipment and intricate locations, such as factories, there are concerns that the number of cameras installed will increase and blind spots will occur due to the effects of occlusion. Therefore, it is expected that drones and robots that can move autonomously can mount and move cameras to patrol and monitor these areas, thereby reducing the number of personnel required for security.

For example, Skydio 2+ is a drone that can fly autonomously using camera images. It uses Visual SLAM to estimate its own position with high accuracy even in non-GNSS space, based on the images from multiple cameras installed on the drone. This system enables safe navigation in narrow, complex structures with steel or concrete frames under bridges and in wide-area shooting. As methods for estimating self-position using camera images in fields other than drones, “A method for estimating self-position by feature point matching” (Okamoto et al., 2012; Yamazaki et al.,

Received: 21 November 2024, Revised: 20 January 2025, Accepted: 15 February 2025, Published: 26 March 2025

* Correspondence: nakahara@oecu.jp

Publisher's Note: JOURNAL OF DIGITAL LIFE. stays neutral with regard to jurisdictional claims in published maps and institutional affiliations.



Copyright: © SANKEI DIGITAL INC. Submitted for possible open access publication under the terms and conditions of the Creative Commons Attribution (CC BY) license (<https://creativecommons.org/licenses/by/4.0/>).

2019) and “A method for feature point matching on a 3D map generated from RGBD camera shots” (Matsumoto et al., 2024; Yang et al., 2020) have been proposed. The former calculates features from a set of previously captured images and compares them with features obtained from the captured images to estimate the location of the captured images. In “A method for feature point matching on a 3D map generated from RGBD camera shots,” a 3D map is created using an RGBD camera to obtain the positional relationships of characteristic structures and objects in a building. Then, based on the created 3D map, the positions where the features match the input image are searched for using deep learning and other methods.

All existing methods estimate self-location under the assumption of many common features in the video, regardless of the time of year. Therefore, when targeting narrow indoor areas with many plain walls, such as those patrolled by security drones, there is “the problem of failing to estimate self-position due to the small number of features” and “the problem of failing to estimate self-position when the feature object itself is moving” in places, such as factories. For example, in the case of Skydio 2+, when flying over a complex structure or a wide area, one of the cameras will always reflect a feature object or landmark location, enabling highly accurate self-position estimation. However, in the case of an indoor hallway between plain walls, the distance from the camera to the plain walls on both sides of the subject is short, and it may be difficult for each camera to always have sufficient features for self-position estimation during flight. Conversely, in “A method for estimating self-position by feature point matching” and “A method for feature point matching on a 3D map generated from RGBD camera shots,” position estimation is based on previously obtained features. Therefore, when applied to locations such as factories, where objects such as tools and instruments are easily moved, the number of commonly obtained features decreases, and a completely different position may be misestimated as the self-position.

In our previous study (Yamashita et al., 2024), we proposed a method using not only a feature point-based approach but also dHash (Figure 1), an algorithm that searches for overlapping images based on changes in the distribution of color information across the entire image. The dHash method calculates a hash value based on the distribution of color changes in the entire image using the luminance gradient of each segmented image area in relation to adjacent areas. Using this algorithm, hash values similar to those in daylight can be calculated based on small differences in luminance even in environments with insufficient light. Therefore, it is highly possible to generate hash values that approximate the nearest pre-captured image even at nighttime, if the features within the shooting range are visible. This method can be used to capture color changes common to images with location information that have been previously captured and images used for self-location estimation, even with few obtained features. In addition, because dHash utilizes information from the entire image, it effectively suppresses the effects of changes in local features caused by object movement better than feature point-based methods. For example, in the case of a hallway, opening and closing doors may cause environmental changes. Therefore, the method can address existing methods problems, such as those of “failing to estimate self-position due to the small number of features” and of “failing to estimate self-position when the feature object itself is moving.” However, demonstration experiments showed that the estimation results are prone to errors on straight sections. However, while the drone used for automatic patrol does not need to change the direction of travel in the straight sections, it needs to change the direction of travel significantly in the straight sections near the curve points. Therefore, the number of images taken in advance must be denser when the drone is close to a curve, and more accurate position estimation is required than in existing studies. In the existing method, no feature change occurs between the images taken before and after the straight section except for the distance from the wall at the end of the curve point, and it is said that there is little difference in the similarity in the straight section near the curve point (Figure 2).

In this study, we propose a method that selects multiple candidate images similar to the input image using scale-invariant feature transform (SIFT) features and then estimates similar images using dHash among them. This method is expected to improve the estimation results for straight sections by considering the distribution of local features influenced by columns, windows, and other factors.

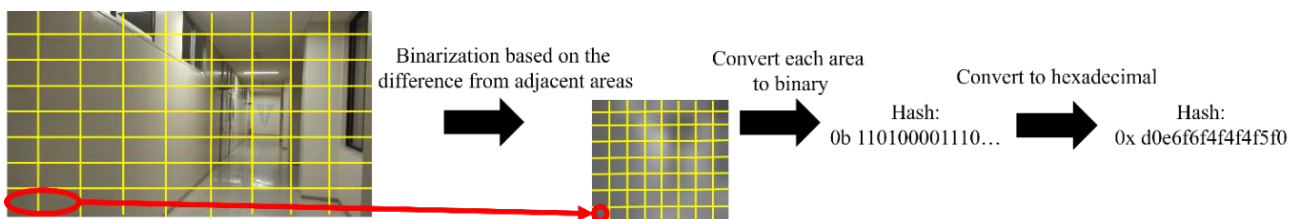


Figure 1. Processing steps of dHash



Figure 2. Examples of straight sections that are prone to estimation failures

2. Methods

2.1 Overview of Methodology

Based on the issues discussed in Section 1, we propose a self-positioning estimation technique that considers the similarity of images taken in straight sections, such as corridors, indoors, and in factories, where security drones target many plain wall surfaces. Figure 3 shows the process flow of the proposed method, which consists of the “Candidate Image Selection Function,” “Similar Image Retrieval Function,” and “Location Estimation Function.” The input data of the proposed method consists of “camera images for location estimation,” “images and location information on the patrol route taken in advance,” and “a map of the patrol route composed of point cloud data.” The output data is the “coordinates of the estimated location,” which can be displayed on a map. In this case, the images on the travel route in the input data are stored with the coordinate values on the map of the travel route corresponding to the shooting position of each image in advance (Figure 4). In this method, images are collected at regular intervals in straight sections, while images are collected at denser intervals in curve sections. This is because the estimated position acquired by this method is used to provide movement instructions to the drone, so it is necessary to collect images at high density in the curve section.

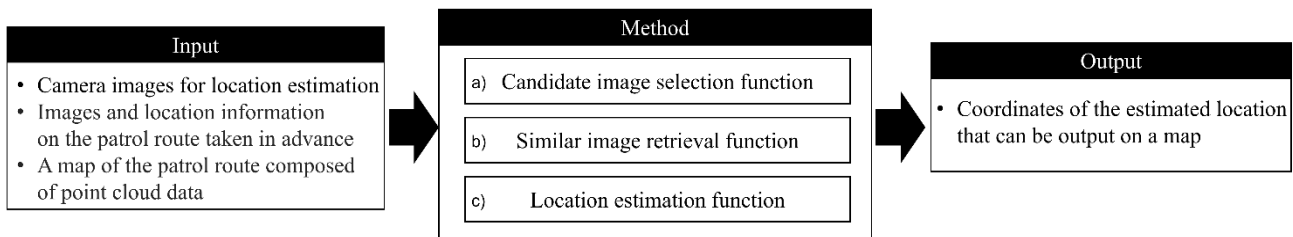


Figure 3. Flow of the proposed method

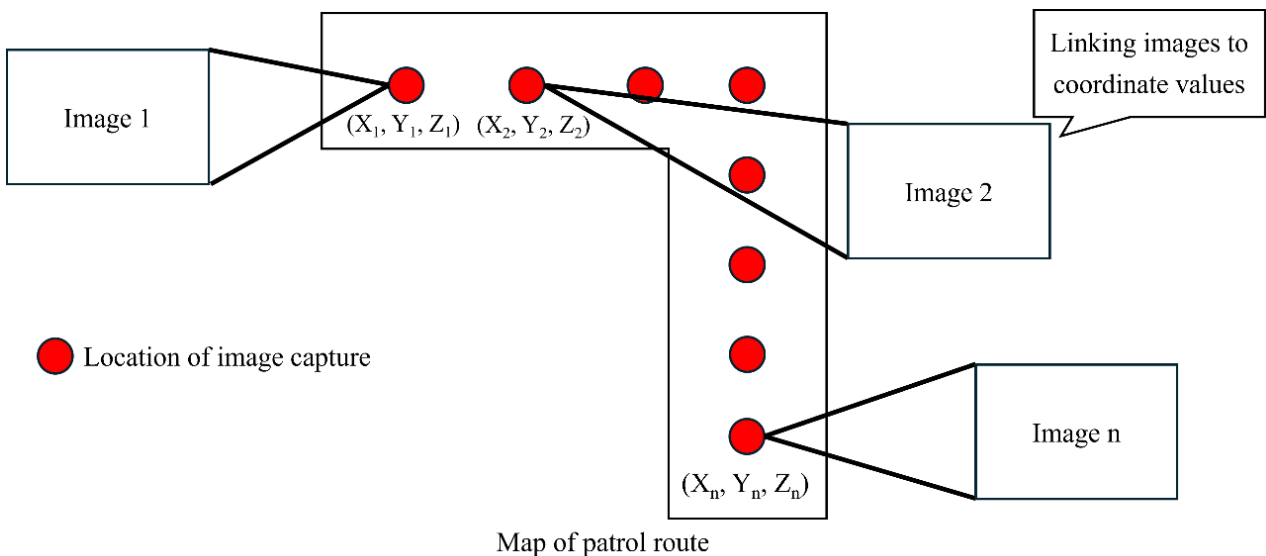


Figure 4. Image diagram of input data

2.2 Candidate Image Selection Function

In the “Candidate Image Selection Function,” the distance to the feature point obtained by SIFT is used as the basis for calculating the similarity between each image and the target images to be searched for. First, local features are calculated using SIFT for images on the traversing path and images used for self-position estimation. However, if local features of the images on the traversing path have already been calculated, they are calculated only for the image used for self-position estimation. The Hamming distance to the corresponding feature is then calculated using Brute-Force Matcher, and the average of all Hamming distances calculated for each image is obtained. This selects a group of images with a certain number of matching features.

2.3 Similar Image Retrieval Function

The “Similar Image Retrieval Function” uses dHash to estimate and output images with a threshold level of similarity or higher with respect to the images selected in the “Candidate Image Selection Function.” First, a hash value is obtained from each image using dHash. Specifically, the grayscale image is divided into regions of a certain size, and the difference in luminance between adjacent regions is calculated. Then, based on the calculated results, the lightness and darkness of the left and right areas are expressed as a string of 01 and output as a hash value. Next, the hash values of the images on the traversing path are compared with the hash values from the images used for self-position estimation, and the Hamming distance is calculated from the XOR operation results. The calculated Hamming distance is normalized in the range of 0–1, and the value is used as the similarity. Furthermore, images on the traversing path with similarity above a threshold value are output as similar images.

2.4 Location Estimation Function

The “Location Estimation Function” estimates the most appropriate location on the map of the traversing route from the images with high similarity estimated by the “Similar Image Retrieval Function.” First, the system obtains the coordinates associated with the images on the traversing path that have a similarity greater than a threshold. Then, using the acquired coordinate values and the estimation result of the previous shooting position, the system outputs the coordinate values associated with the image with the highest similarity within the range where the drone can move from the previous position to the current shooting position(Figure 5). However, in the absence of a previous estimated position, the system outputs the position of the image with the highest similarity as the current shooting position.

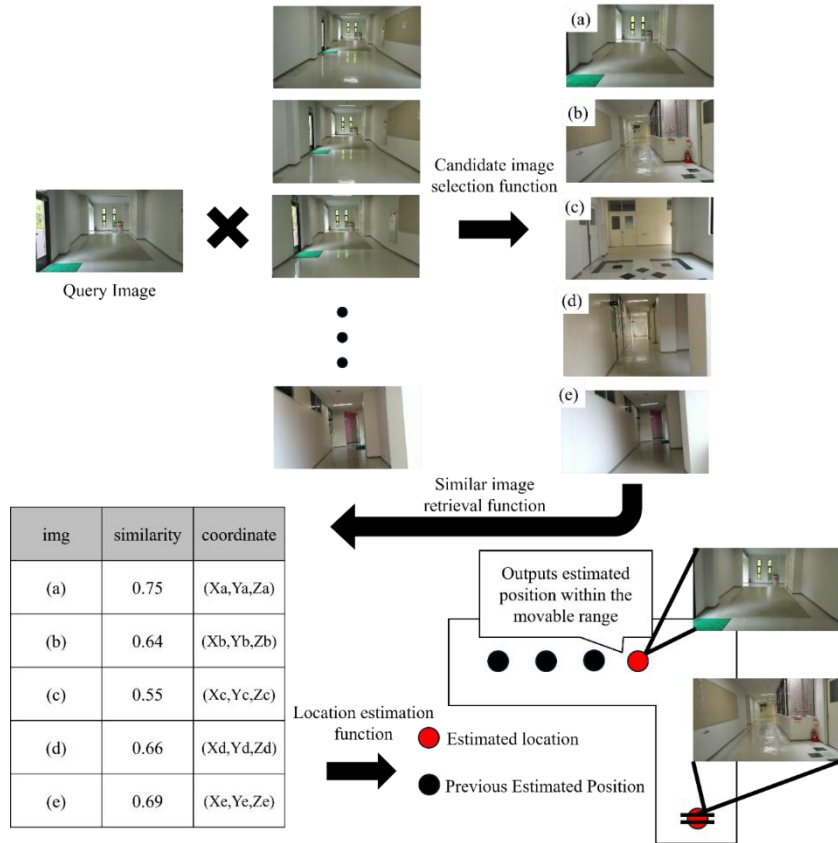


Figure 5. Diagram of each function

3. Results

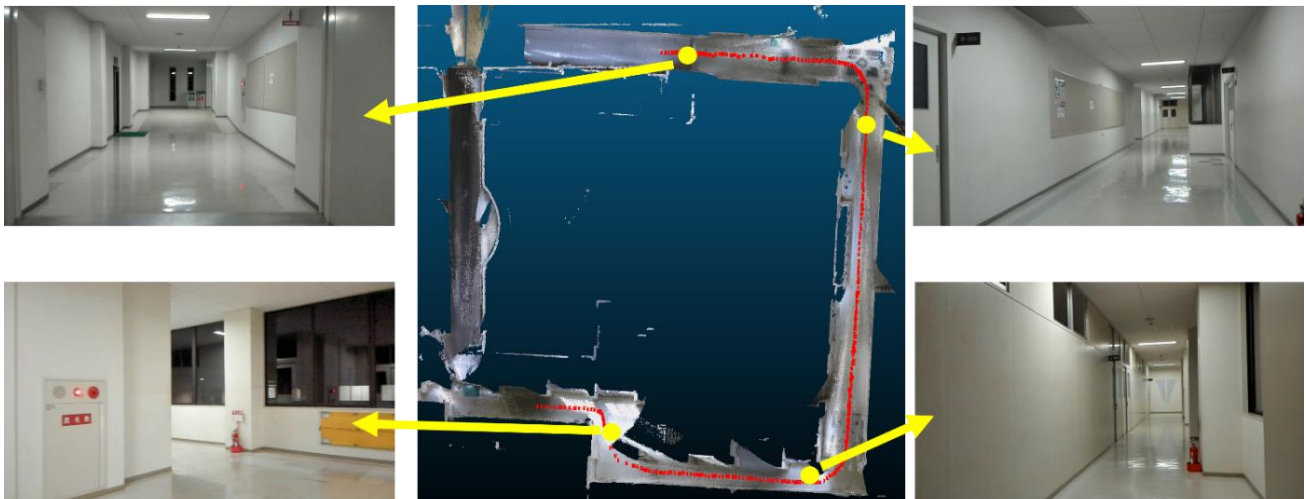
3.1 Verification Experiments

We applied the proposed method to an indoor corridor at night, assuming two types of situations: one in which the situation is the same as when the image was taken beforehand, and another where the situation has changed. Then, we verified the applicability of the proposed method to self-position estimation for automatic patrols by security drones. The experiment location was an L-shaped corridor on a university campus, which has many plain walls and straight sections that are difficult to estimate using the proposed method and previous research methods. For the input data, a 3D map consisting of point cloud data was constructed using a unit that can measure point cloud data by SLAM, as used in previous work (Kajitani et al., 2024). The measurement unit recorded images of the patrol route in advance and linked the coordinate values to the map (Figure 6).

In the present experiment, to compare with the previous study and to verify the effects of changes in local features, we also verified the case in which the objects that are features, such as door opening and closing and installation locations, which are likely to be features in self-position estimation, are varied in each case of the previous study (Yamashita et al., 2024) and the proposed method. In addition, each input image must match the shooting conditions of a small drone that can fly indoors. To simulate flight, we raised a hand-held web camera capable of capturing RGB images to the same height as the small drone's flight altitude. During the evaluation, we compared the self-positions estimated by each method with the actual shooting positions. We then compared the percentage of correctly estimated positions to the shooting positions at all locations, thereby confirming the usefulness of the proposed method. Furthermore, we verified the applicability of the proposed method from the viewpoint of applying it to automatic patrols by security drones.

3.2 Experiments Results

Figure 7(a) shows the visualization results of position estimation using only dHash without changing local features; Figure 7(b) shows the visualization results of position estimation using the proposed method; and Figure 7(c) shows the visualization results of position estimation using the proposed method with changing local features. Table 1 shows the percentage of correct responses, the average position error, and the maximum error for similar images in each result. Notably, the location estimation process, which solely relied on dHash and required input images with local feature changes, experienced significant failure. Consequently, we didn't verify the visualization results or compute the error amount.



Red Point : Location of images on the tied patrol route

Figure 6. Map visualization of patrol routes

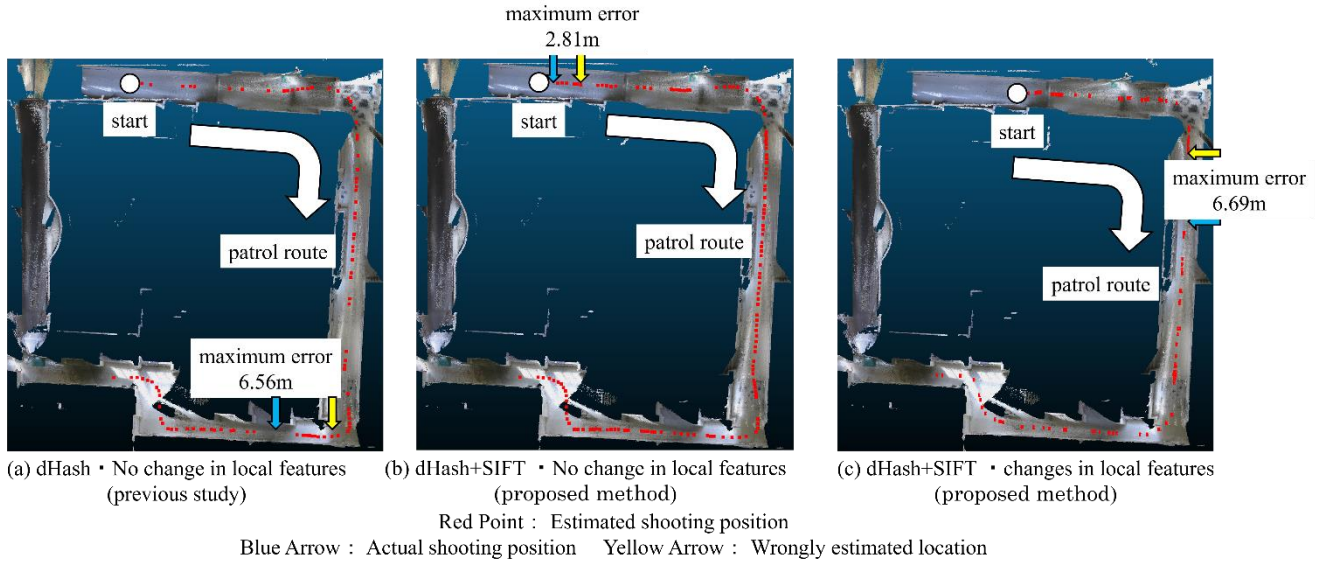


Figure 7. Location Estimation Visualization Results

Table 1. Percentage of correct answers in each result

| Local feature | Method | Number of input images | Number of correct images | Correct responses | Average position error | Maximum error |
|---------------|-------------------------|------------------------|--------------------------|-------------------|------------------------|---------------|
| No change | dHash | 216 | 153 | 70.8% | 2.54m | 6.56m |
| | dHash+SIFT (Our Method) | 216 | 209 | 96.3% | 2.14m | 2.81m |
| Change | dHash | 129 | 36 | 27.9% | error | error |
| | dHash+SIFT (Our Method) | 129 | 106 | 82.8% | 3.37m | 6.69m |

4. Discussion

As shown by visualization results of position estimation in Figure 7(b) and (c), the position of the drone on its patrol path is generally estimated from the webcam image, even when SIFT is combined with SIFT. The comparison of the percentage of correct responses in Table 1 confirms that the combination of SIFT produces more accurate location estimation results in both cases, with and without changes in local features. This suggests that the method improves two issues in the existing approach. Comparing the respective results with no change in local features, the maximum values of the percentage of correct answers and position errors confirm the improvement in the accuracy of position estimation. Specifically, the calculation of more than 90% of the correct answers validates the feasibility of location estimation across all sections. Therefore, we confirm that combining a method such as dHash, which generously captures overall features, and SIFT, which is a feature point-based method, is useful even with few features, such as in a corridor or in a straight section, which has been an issue in previous studies.

The combined dHash and SIFT method was generally successful in estimating the input images when local features were changing. However, when the results were compared with and without local features, the percentage of correct responses decreased and the location error worsened. In fact, when we checked the location where the maximum error occurred in Figure 7(c), we found several locations where local features changed (Figure 8). Thus, it is unlikely that feature point-based methods alone can further improve estimation accuracy in locations with many changes in local features. It is expected to achieve higher accuracy by comparing the results of similarity calculations between the feature point-based method and dHash and using the more reliable estimation result as a reference for location estimation. However, this experiment assumed that the actual patrolling guards might be in a dark place with no

lighting, despite taking the input images with the lighting on. Therefore, we need to enhance the method's sensitivity to light intensity changes using gamma correction or deep learning to produce images that mimic a quasi-bright environment.

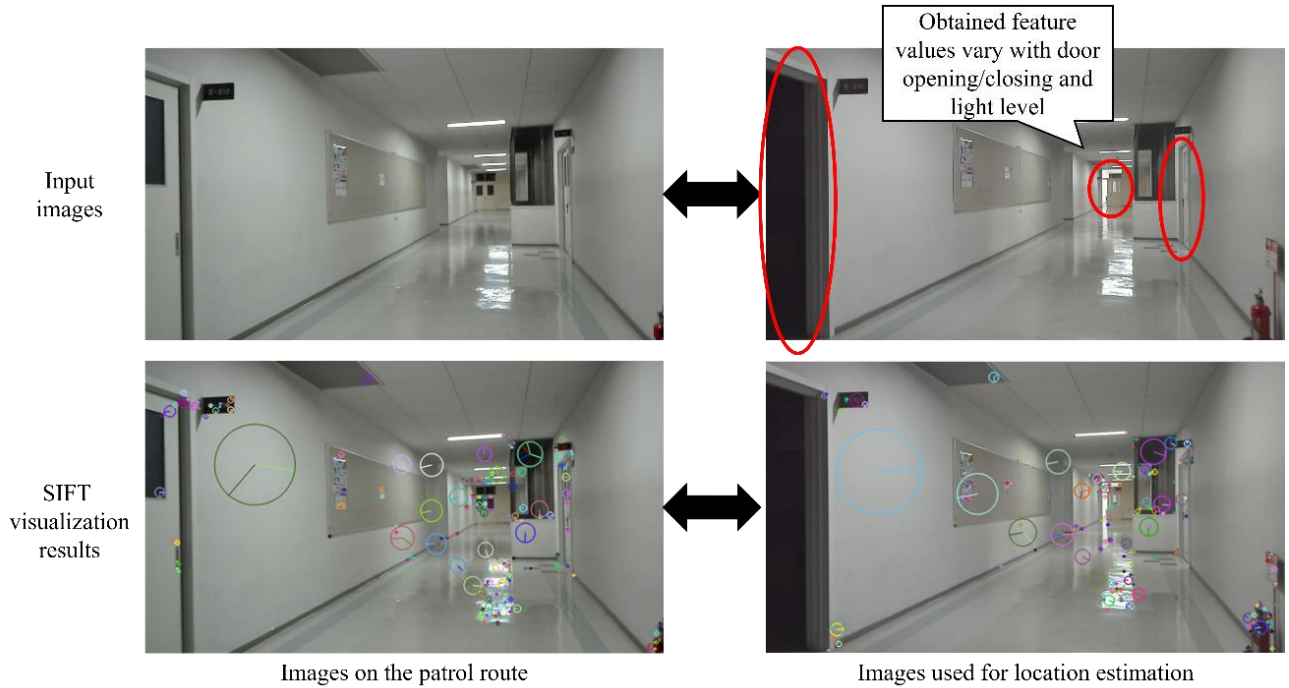


Figure 8. Locations of maximum error in Figure 7(c) results

5. Conclusions

In this paper, we propose a method for estimating self-location by combining SIFT and dHash to search similar images for indoor areas with few features. Empirical experiments confirm that the overall accuracy can be improved, even for straight sections that previous studies found difficult to estimate. In the future, we aim to make this method robust to changes in light intensity and develop a self-position estimation technique that can be applied even at night.

Author Contributions

Conceptualization, M.N. and S.Y.; methodology, M.N., Y.T., Y.U. and S.Y.; software, S.Y.; validation, S.Y.; formal analysis, S.Y.; investigation, S.Y.; resources, M.N. and S.Y.; data curation, S.Y.; writing—original draft preparation, S.Y.; writing—review and editing, M.N., Y.T. and Y.U.; visualization, S.Y.; supervision, M.N., Y.T. and Y.U.; project administration, M.N.

Funding

This research received no external funding.

Informed Consent Statement

Not applicable.

Conflicts of Interest

The authors declare no conflict of interest.

References:

Kajitani, M., Nakahara, M., Tsukada, Y., Umehara, Y., Nishida, Y., Shimizu, N. & Tanaka, S. (2024). Research on correction of point cloud data by handheld laser scanner with SLAM. *Proceedings of the 86th National Convention of IPSJ*, 86(4), 805-806.

Research on Indoor Self-Location Estimation Technique
Using Similar Image Retrieval Considering Environmental Changes
Masaya Nakahara, Yoshinori Tsukada, Yoshimasa Umehara and Shota Yamashita

- Matsumoto, Y., Nakano, G. & Ogura, K. (2024). Indoor visual localization using point and line correspondences in dense colored point cloud. *2024 IEEE/CVF Winter Conference on Applications of Computer Vision (WACV)*, 3604-3613.
- Ministry of Health, Labour and Welfare. Employment referrals for general workers. (2024). <https://www.mhlw.go.jp/toukei/list/114-1.html>
- Okamoto, K., Kazama, H. & Kawamoto, K. (2012). A fuzzy codebook based image search method for visual localization in libraries. *28th Fuzzy System Symposium*, 28, 444-447.
- Skydio. Skydio2+. (2024). <https://www.skydio.com/skydio-2-plus-enterprise>
- Yamashita, S., Nakahara, M., Tsukada, Y. & Umehara, Y. (2024). Research on estimation technique of self-location indoors using similar image retrieval technique. *Proceedings of the symposium on civil engineering informatics*, 49, 205-208.
- Yamazaki, K., Shishido, H., Kitahara, I. & Kameda, Y. (2019). Evaluation for harmonic location estimation system of image retrieval and SLAM. *International Workshop on Advanced Imaging Technologies 2020*
- Yang, Y., Toth, C. & Brzezinska, D. (2020). A 3D map aided deep learning based indoor localization system for smart devices, *The International Archives of the Photogrammetry Remote Sensing and Spatial Information Sciences.*, XLIII-B4-2020, 391–397.

Special Issue: Measurement, control, and analysis of motion using ICT and AI
Article

A Study on the Development of a Traffic Volume Counting Method by Vehicle Type and Direction Using Deep Learning

Yuhei Yamamoto ¹, Masaya Nakahara ², Ryo Sumiyoshi ³, Wenyuan Jiang ⁴, Daisuke Kamiya ⁵ and Ryuichi Imai ^{6*}

¹Faculty of Environmental and Urban Engineering, Kansai University, 3-3-35 Yamate-cho, Suita-shi, Osaka 564-8680, Japan

²Faculty of Information Science and Arts, Osaka Electro-Communication University, 1130-70 Kiyotaki, Shijonawate-shi, Osaka 575-0063, Japan

³Doctoral Course Graduate School of Engineering and Design, Hosei University, 2-33 Ichigaya-tamachi, Shinjuku-ku, Tokyo 162-0843, Japan

⁴Faculty of Engineering, Osaka Sangyo University, 3-1-1 Nakagakiuchi, Daito-shi, Osaka 574-8530, Japan

⁵Faculty of Engineering, University of the Ryukyus, 1 Senbaru, Nishihara-cho, Nakagami-gun, Okinawa 903-0213, Japan

⁶Faculty of Engineering and Design, Hosei University, 2-33 Ichigaya-tamachi, Shinjuku-ku, Tokyo 162-0843, Japan

Abstract

The turning movement count is investigated to understand the traffic conditions at intersections and identify bottleneck locations. In recent years, methods utilizing probe data and AI-based analysis of video images have been developed to streamline the survey process. Existing methods can count vehicles as they pass but struggle to classify vehicle types. Therefore, the objective of this study is to develop a method for counting turning movement count by vehicle type using deep learning. In this method, YOLOv8 is used to detect cars, buses, and trucks in video images, and BoT-SORT is used for tracking. When a vehicle being tracked crosses the cross-sectional lines and auxiliary lines at the intersection captured in the video images, it is counted by class. In this case, the entry direction of vehicles that cannot be determined upon entering the intersection is estimated based on accurately counted vehicles. Additionally, the entry direction is inferred from a series of vector information within the detection bounding boxes. The results of the verification experiment showed that the proposed method can count the directional traffic volume with an accuracy of over 95.0% and classify the three vehicle classes—car, bus, and truck—with an accuracy of over 90.0%.

Keywords: *Turning Movement Counts, Vehicle, Deep Learning, Image Processing, Classification*

1. Introduction

In many countries, turning movement counts surveys are conducted to understand the usage of roads (Japan International Cooperation Agency, 2018 and Streetlight Data, 2024). In Japan, turning movement counts are counted by turning movements (right-turn, left-turn, and straight) and vehicle type to understand traffic conditions at intersections and identify bottleneck locations. This survey requires at least four surveyors per intersection, leading to increased survey costs as the number of survey locations increases. For example, in Tokyo, a large-scale survey was conducted as part of the Major Intersection Traffic Volume Survey, covering 125 intersections and requiring more than 500 surveyors (Metropolitan Police Department, 2023). Against this backdrop, in recent years, the Ministry of Land, Infrastructure, Transport and Tourism has been exploring survey methods that utilize probe data to streamline the process, as well as methods that analyze recorded video images using AI (Ministry of Land, Infrastructure, Transport and Tourism, 2019). A survey method using probe data has demonstrated the potential to count turning movement counts by combining ETC 2.0 probe data with data collected from vehicle detectors (Shiomi, 2022).

Received: 21 November 2024, Revised: 29 January 2025, Accepted: 27 February 2025, Published: 26 March 2025

* Correspondence: imai@hosei.ac.jp

Publisher's Note: JOURNAL OF DIGITAL LIFE. stays neutral with regard to jurisdictional claims in published maps and institutional affiliations.



Copyright: © SANKEI DIGITAL INC. Submitted for possible open access publication under the terms and conditions of the Creative Commons Attribution (CC BY) license (<https://creativecommons.org/licenses/by/4.0/>).

However, when the penetration rate of vehicles equipped with ETC 2.0 probe data is low, the accuracy of traffic volume counting decreases, presenting a significant challenge. Although the penetration rate is expected to increase as more vehicles are equipped with ETC 2.0 onboard units, the installation incurs additional costs. Therefore, it is challenging to rapidly promote the widespread adoption of onboard units. In response, we focused on a survey method that analyzes video images using AI. As survey methods using AI, there are two primary approaches: one involves counting based on vehicle trajectories (Horii et al., 2022), and the other sets cross-sectional lines on roads visible in video images and counts vehicles passing through these lines (Watanabe et al., 2023). However, the former method faces a challenge in that vehicle trajectories differ for each intersection, requiring parameter adjustments for counting every time the target intersection changes. This challenge could potentially be resolved by predefining the camera angles during filming, which may reduce variations in vehicle trajectories specific to each intersection. However, this approach cannot be applied to intersections that do not fit the predefined camera angles, leading to a reduction in versatility. The latter issue, as shown in Fig.1, arises from the occlusion that occurs when vehicles overlap near the cross-sectional line, causing vehicles farther from the camera to be obscured, which leads to counting omissions. To address this issue, we have developed a method for counting turning movement counts that sets auxiliary lines in addition to cross-sectional lines as a countermeasure against occlusion (Sumiyoshi et al., 2024). However, this method cannot count turning movement counts categorized by vehicle type. Therefore, the purpose of this study was to develop a method for counting turning movement counts by vehicle type using deep learning applied to video images of intersections. In Section 2, the proposed method is explained in detail, and the experimental conditions for verifying its effectiveness are described. Section 3 evaluates and discusses the results of the demonstration experiments. Section 4 provides a summary of this study.

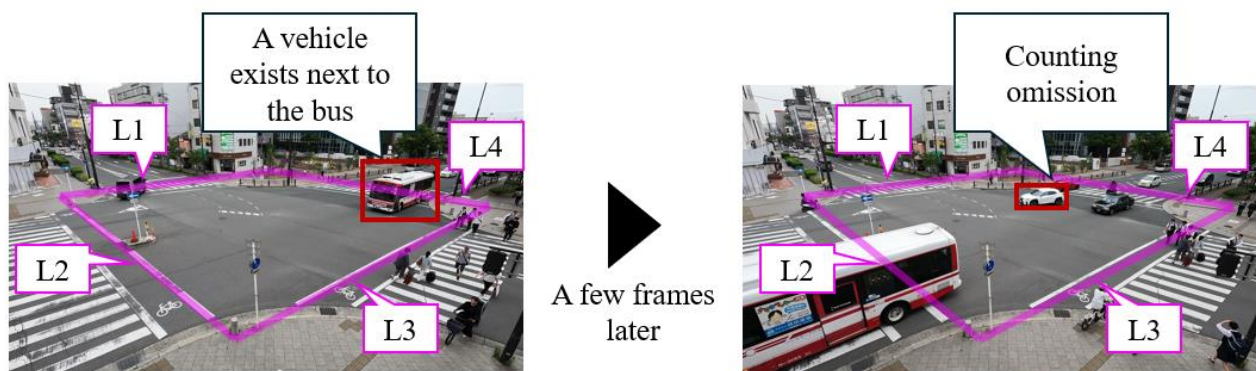


Fig.1. Scenarios where counting omissions occur in existing methods

2. Methods

In this section, we summarize the challenges identified in existing research and outline the development strategy of the method devised in this study. Next, we provide a detailed explanation of the proposed method. Then, we describe the conditions of the empirical experiments conducted using this method.

2.1 Development Approach for Counting Turning Movement Counts by Vehicle Type

This section organizes the challenges identified in existing studies and outlines the development approach for the method proposed in this study (Watanabe et al., 2023). This method has been reported to result in counting omissions when occlusion occurs within the region enclosed by the cross-sectional line, causing the vehicle ID to switch (see Fig.1). Hamamura et al. utilized YOLOv7, an object detection method, fine-tuning it with images of passenger cars, light trucks, buses, and motorcycles to count cross-sectional traffic volumes by vehicle type (Hamamura et al., 2023). Additionally, Okubo et al. employed the SSD object detection method, training it with images of light trucks, buses, passenger cars, small trucks, pedestrians, motorcycles, and bicycles to count cross-sectional traffic volumes by the trained classes (Okubo et al., 2020). These methods aim to count cross-sectional traffic volumes, leading to the placement of cross-sectional lines closer to the camera. However, to count turning movement counts, it is necessary to place cross-sectional lines at positions farther from the camera. Therefore, near the cross-sectional lines farther from the camera, vehicles appear smaller in the footage, potentially leading to a decrease in vehicle classification accuracy.

Based on the above, this study proposes a method to address undercounting caused by occlusion. The method involves analyzing traffic conditions using vehicles that are correctly counted and estimating the inflow directions of vehicles for which only outflow directions can be determined. Additionally, to improve the classification accuracy of small vehicles appearing in the footage, this study employs the YOLOv8x model, which can detect smaller objects with higher precision than YOLOv7 by replacing the Detection Head with one based on NAS-FPN (Varghese, R and Sambath, M, 2024). Furthermore, to enhance vehicle classification accuracy, this study incorporates not only the classification results of vehicles on the cross-sectional line but also employs a majority voting approach based on the classification results of vehicles within the area enclosed by the cross-sectional lines.

2.2 Proposal of a Method for Counting Turning Movement Counts by Vehicle Type

The processing flow of the proposed method is illustrated in Fig.2. This process consists of cross-sectional and auxiliary line setting, detection, counting, interpolation, and vehicle classification.

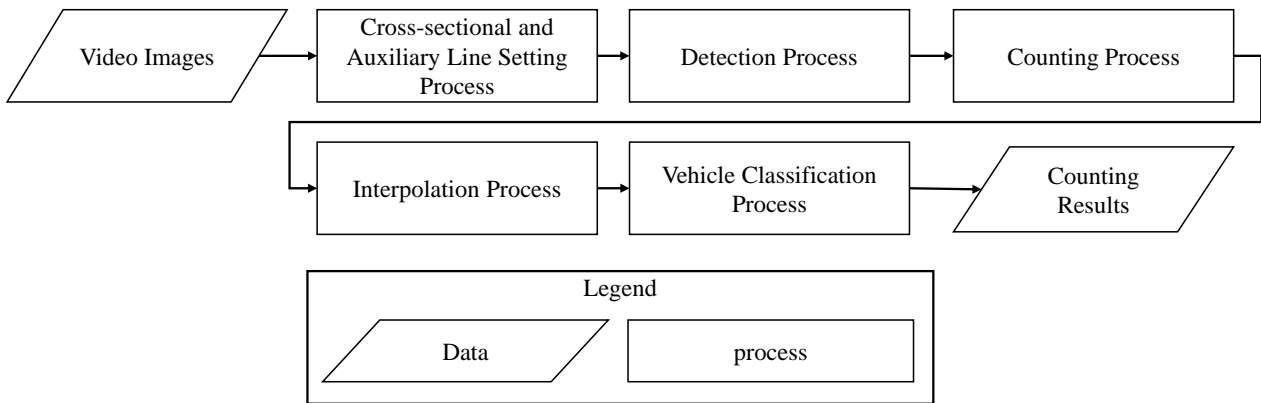


Fig.2. Processing Flow of the Proposed Method

In the cross-sectional and auxiliary line setting process, cross-sectional and auxiliary lines are established to determine the inflow and outflow directions. The flow of the process is illustrated in Fig.3a. First, eight points (points 1 through 8) are manually selected to enclose the intersection. Next, lines are drawn connecting points 1 and 2, points 3 and 4, points 5 and 6, and points 7 and 8. These lines are extended until adjacent lines intersect. Then, auxiliary lines are established by connecting the midpoints of opposing cross-sectional lines. This approach reduces the impact of occlusion within the area enclosed by the cross-sectional lines.

In the detection process, vehicles appearing in the video images are detected and tracked to count turning movement counts. In this process, the YOLOv8x model is used to detect three classes: car, bus, and truck. Next, the detected vehicles are tracked using BoT-SORT (Aharon et al., 2022). During this process, an ID is assigned to each tracked vehicle to prevent excessive counting at the cross-sectional lines.

In the counting process, vehicles crossing the cross-sectional and auxiliary lines are counted. First, when the midpoint of the bottom edge of a bounding box for a detected vehicle passes over a cross-sectional or auxiliary line, the ID of that vehicle is recorded. This allows for determining the direction from which the vehicle entered. Subsequently, when the midpoint of the bottom edge of the bounding box for the detected vehicle crosses another cross-sectional line, the vehicle's ID is recorded again. This process determines the outflow direction and ensures the vehicle is counted as a single unit.

Here, an example is explained for the case where a vehicle enters from L1 direction and exits from L3 direction. In determining the entry direction, it is assessed whether the vehicle has passed the cross-sectional lines and auxiliary lines by verifying if it satisfies equation (1). In this case, x_1, y_1 represents the intersection of L1 and L4, x_2, y_2 represents the intersection of L1 and L2, and x_p, y_p represents the midpoint of the lower edge of the bounding box in the previous frame. Next, the intersection between the line segment connecting the midpoints of the lower edges of the rectangle and L1 is determined using equations (2), (3), and (4). The CCW (Counter Clockwise) function defined in (2) is used to evaluate the geometric configuration of three points. When the result of this function is positive, the points are arranged in a counterclockwise order; when negative, they are arranged in a clockwise order; and when

zero, the points are collinear. Furthermore, when both equations (3) and (4) are satisfied, it can be determined that the two line segments intersect, indicating that there is an enters from the direction of L1. In this case, A represents the midpoint of the lower edge of the bounding box in the previous frame, B represents the midpoint of the lower edge of the bounding box in the current frame, C represents the intersection of L1 and L4, and D represents the intersection of L1 and L2. In determining the exit direction, equation (5) is used to assess whether the midpoint of the lower edge of the bounding box in the previous frame is located within the region enclosed by the cross-sectional lines. In this case, x_1, y_1 represent the intersection of L3 and L4, x_2, y_2 represent the intersection of L3 and L2, and x_p, y_p denote the midpoint of the lower edge of the bounding box in the previous frame. Furthermore, similar to the entry direction determination, equations (2), (3), and (4) are used to verify whether the line segment connecting the midpoints of the lower edges of the bounding boxes intersects with L3. If an intersection is confirmed, the vehicle is determined to have exited in the direction of L3.

$$(x_2 - x_1) \cdot (y_p - y_1) - (y_2 - y_1) \cdot (x_p - x_1) \geq 0 \quad (1)$$

$$\text{CCW}(A, B, C) = (y_C - y_A) \cdot (x_B - x_A) - (y_B - y_A) \cdot (x_C - x_A) \quad (2)$$

$$(\text{CCW}(A, B, C)) \cdot (\text{CCW}(A, B, D)) \leq 0 \quad (3)$$

$$(\text{CCW}(C, D, A)) \cdot (\text{CCW}(C, D, B)) \leq 0 \quad (4)$$

$$(x_2 - x_1) \cdot (y_p - y_1) - (y_2 - y_1) \cdot (x_p - x_1) < 0 \quad (5)$$

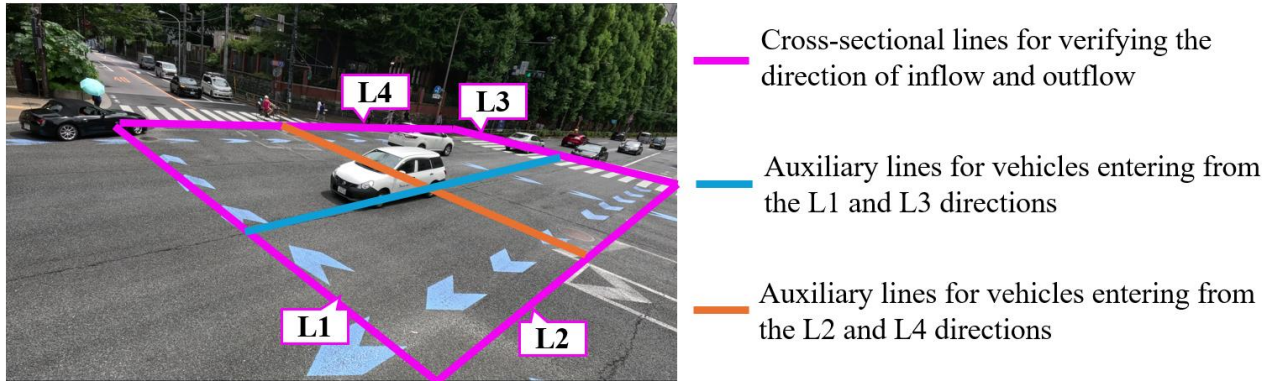
In the interpolation process, vehicles for which the inflow direction cannot be determined are supplemented by estimating their inflow direction, thereby addressing undercounting issues. The flow of this process is illustrated in Fig.3b. First, the inflow direction candidates are estimated for each time point based on the time when the counted vehicles crossed the second cross-sectional line and their travel direction. Next, for vehicles whose inflow direction cannot be determined due to occlusion, the inflow direction is uniquely estimated based on the vector information, including the sequence of timestamps and positions as the vehicle crosses the outflow cross-sectional line.

An example is provided here for the case where a vehicle enters from L2 direction and exits from L3 direction. First, the possible entry direction candidates are estimated based on the time when the target vehicle passed L3 and the time when the correctly counted vehicles passed the second section line. In this example, as shown in Fig. 3b, we assume that vehicles are entering from L2 and L4 directions during this time period. Then, when equation (6) is satisfied, the vehicle is estimated to have entered from the L4 direction, and when equation (7) is satisfied, it is estimated to have entered from the L2 direction. In this case, y_2 represents the y-coordinate of the midpoint of the lower edge of the bounding box when the vehicle passes L3, and y_1 represents the y-coordinate of the midpoint of the lower edge of the bounding box when the vehicle is first detected within the area enclosed by the section line.

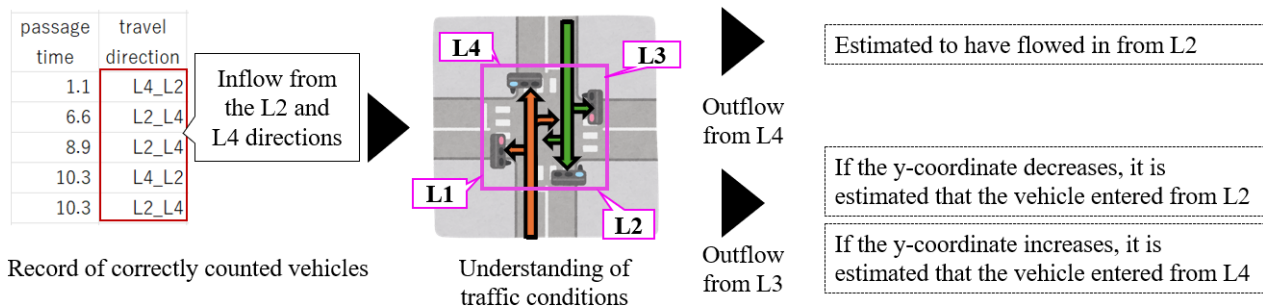
$$y_2 - y_1 > 0 \quad (6)$$

$$y_2 - y_1 < 0 \quad (7)$$

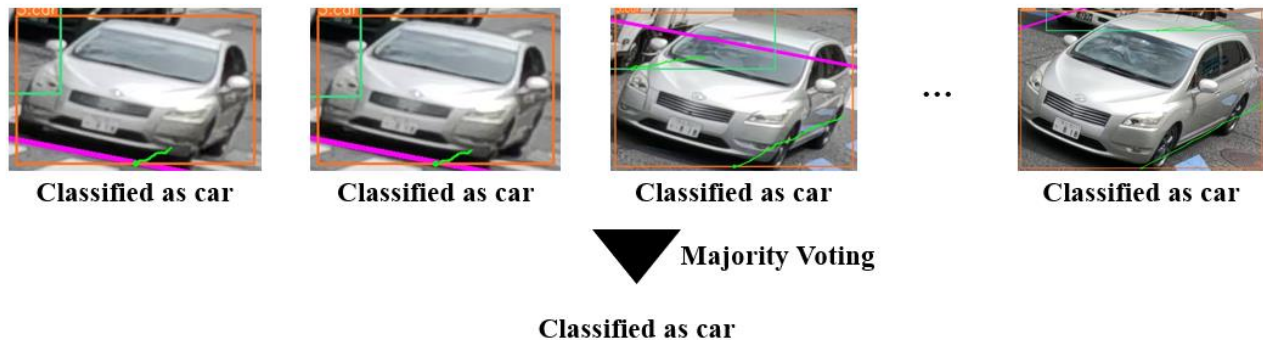
In the vehicle classification process, the counted vehicles are categorized into three classes: car, bus, and truck. The flow of this process is illustrated in Fig.3c. First, the classification results from the YOLOv8x model are recorded for vehicles detected within the area enclosed by the cross-sectional lines. Then, the recorded results are used to determine the vehicle type by applying majority voting to the classification outcomes for each vehicle ID, thereby finalizing the classification.



a. Example of cross-sectional and auxiliary line settings



b. Illustration of the interpolation process



c. Conceptual diagram of vehicle type classification process

Fig.3. Processing flow of the proposed method

2.3 Validation of the Proposed Method's Effectiveness

In this study, two validations were conducted to verify the effectiveness of the proposed method. In the first validation, to assess the effectiveness of the interpolation process in the proposed method, we applied both the existing method (Sumiyoshi et al., 2024) and the proposed method to video images of intersections and compared the counting accuracy of turning movement counts. In the second validation, to evaluate the vehicle classification accuracy of the proposed method, vehicle types were classified for the vehicles counted using the proposed method in the first validation. Both validations used video images recorded for 25 minutes at an intersection in Tokyo. The target road consisted of four lanes in total, with two lanes in each direction (see Fig.4). During the recording, approximately 33 vehicles per minute

were observed traveling through the intersection. The weather during the recording was cloudy. The video images were captured using a GoPro HERO11 mounted on a survey pole, which was extended to a height of approximately 4.0 meters above the ground. During the recording, the GoPro HERO11 was set to a resolution of 5.3K at 30 fps. In both validations, the number of correctly identified vehicles was verified through manual observation. Precision, recall, and F1-score were calculated to evaluate the performance. However, in Validation 1, vehicles exiting from L1 to L2 and from L3 to L4 had a passage count of zero, making it impossible to calculate evaluation metrics. Therefore, these cases were excluded from the evaluation.

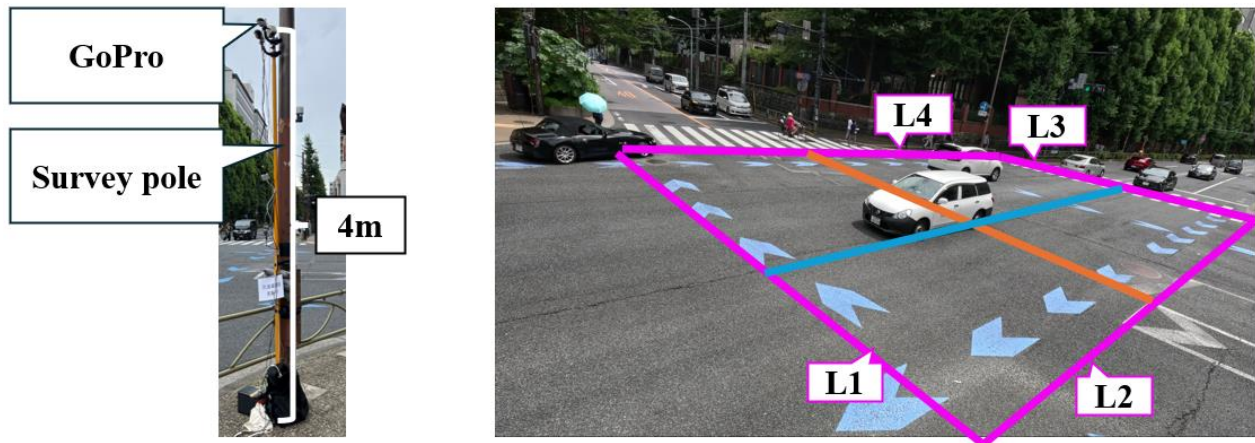


Fig.4. Equipment installation diagram and camera angle during shooting

3. Results

3.1 Validation of Counting Accuracy for Turning Movement Counts

The results of turning movement counts counting are shown in Table 1. First, upon examining the F1-scores, it was found that the proposed method achieved higher scores than the existing method across all directions. Furthermore, in the proposed method, the F1-scores for all directions except for vehicles traveling from L2 to L1 were 0.950 or higher, demonstrating an accuracy comparable to manual observations. Additionally, in the existing method, vehicles traveling in the L3 direction, such as from L1 to L3 and L4 to L3, exhibited low recall rates, indicating a higher incidence of undercounting. The likely cause is that L3 is the farthest cross-sectional line from the camera, making it more prone to occlusion. Similarly, vehicles traveling from L1 to L4 experienced undercounting due to the large number of vehicles traveling from L1 to L3, which caused frequent occlusions. On the other hand, examining the recall rates of the proposed method revealed improvements over the existing method, with vehicles traveling from L1 to L3 achieving a recall of 0.926, from L2 to L3 achieving 1.000, and from L4 to L3 achieving 0.969. Additionally, for vehicles traveling from L1 to L4, the recall rate was 1.000, indicating that detection omissions were successfully mitigated. This indicates that the implementation of the interpolation process in the proposed method, which estimates inflow directions from outflow directions, has the potential to count left-turning vehicles and occluded vehicles, addressing the challenges faced by the existing method. However, for vehicles traveling from L2 to L1, even the proposed method resulted in an F1-score below 0.800. Vehicles traveling from L2 to L1 pass closest to the camera, resulting in their upper sections being visible for only a short duration. This condition led to instances of undercounting. The intersection targeted in this experiment was a large one, with a distance of approximately 70 meters from the camera's position to the farthest crosswalk. Therefore, depending on the size of the intersection, it can be considered that installing two cameras along the diagonals of the intersection can ensure counting accuracy. Furthermore, for vehicles traveling from L1 to L4, fluctuations in the bounding boxes caused by straight-moving vehicles resulted in excessive counting when the midpoint of the lower edge of the bounding box crossed the sectional line (see Fig.5). In this case, because the straight-moving vehicles travel in front of the vehicles that are excessively counted, the upper edge of the bounding box exhibits less movement compared to the lower edge. Therefore, by focusing on the displacement of the upper edge of the bounding box, it may be possible to achieve improvements.

Table 1. Counting results of directional traffic volume

| Inflow Direction | Outflow Direction | Ground Truth (vehicles) | Existing Method | | | Proposed Method | | |
|------------------|-------------------|-------------------------|-----------------|--------|----------|-----------------|--------|----------|
| | | | Precision | Recall | F1-score | Precision | Recall | F1-score |
| L1 | L3 | 244 | 1.000 | 0.820 | 0.901 | 1.000 | 0.926 | 0.962 |
| | L4 | 44 | 0.909 | 0.909 | 0.909 | 0.917 | 1.000 | 0.957 |
| L2 | L1 | 29 | 0.905 | 0.655 | 0.760 | 0.909 | 0.690 | 0.784 |
| | L3 | 8 | 1.000 | 0.875 | 0.933 | 1.000 | 1.000 | 1.000 |
| | L4 | 101 | 1.000 | 0.980 | 0.990 | 1.000 | 1.000 | 1.000 |
| L3 | L1 | 223 | 1.000 | 0.960 | 0.979 | 1.000 | 0.973 | 0.986 |
| | L2 | 24 | 0.960 | 1.000 | 0.980 | 0.960 | 1.000 | 0.980 |
| L4 | L1 | 47 | 0.947 | 0.766 | 0.847 | 0.978 | 0.936 | 0.957 |
| | L2 | 72 | 1.000 | 0.903 | 0.949 | 1.000 | 0.931 | 0.969 |
| | L3 | 32 | 0.955 | 0.656 | 0.778 | 0.969 | 0.969 | 0.969 |
| All | | 824 | 0.986 | 0.880 | 0.930 | 0.989 | 0.949 | 0.968 |

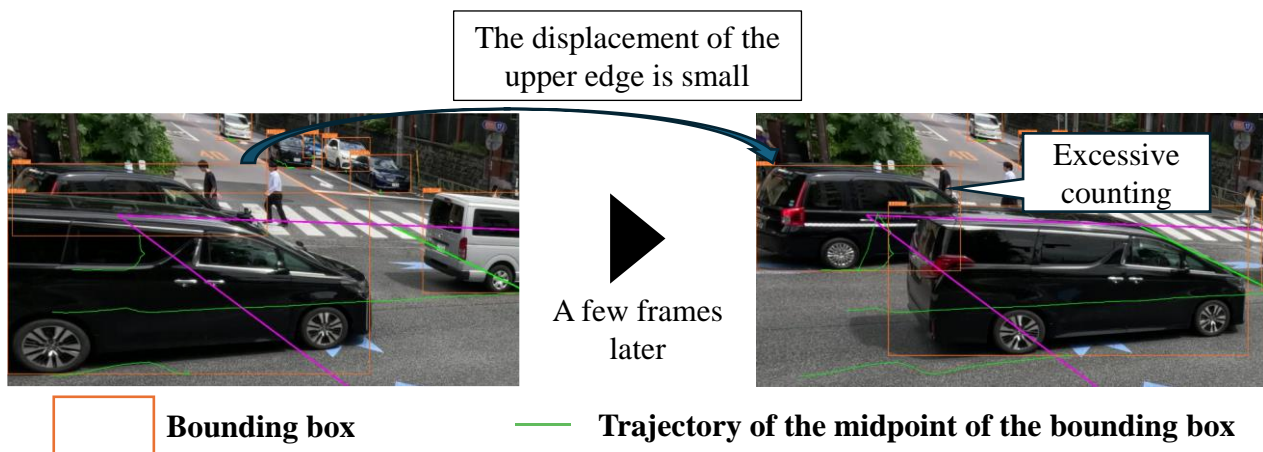


Fig.5. Examples of counting failures

3.2 Validation of Vehicle Classification Accuracy

The results of vehicle classification are shown in Table 2. Upon examining the results, it was found that the F1-scores for car, bus, and truck were 0.900 or higher. Furthermore, when aggregating the classification results across all classes, it was found that the F1-score was 0.973, demonstrating a higher accuracy than the manual counting accuracy of 95.0%. Furthermore, for vehicles that exhibited misclassifications during tracking, it was found that using time-series data allowed for correct classification through majority voting. Upon examining the images where trucks were misclassified as cars, it was observed that such misclassifications occurred predominantly in scenarios where the front of the vehicle was prominently visible. As shown in Fig.6, this issue could potentially be mitigated by collecting images that prominently feature the front view of vehicles and fine-tuning the YOLOv8x model accordingly. Furthermore, among the 12 trucks misclassified as cars, 11 were small-sized trucks. In turning movement counts surveys, it is a common practice to classify vehicles into categories such as small and large vehicles, with cars typically falling under the category of small vehicles. Therefore, from a practical application perspective, these 11 trucks can be considered to have been correctly classified. On the other hand, upon reviewing the images misclassified as trucks, it was found that a significant number featured boxcars. Similar to the case with trucks, this issue could potentially be addressed by creating training data from images containing boxcars and fine-tuning the model accordingly. Additionally, we have demonstrated that the application of deep-learning-based image classification methods enables highly accurate vehicle type classification when measuring cross-sectional traffic volume by vehicle type. Therefore,

when measuring turning movement counts by vehicle type, it is considered feasible to classify vehicles into small and large categories by extracting images of vehicles classified as trucks and applying image classification methods.

Table 2. Classification results by vehicle type

| Class | Ground Truth (Vehicles) | Predicted Count (Vehicles) | True Positive Count (Vehicles) | Precision | Recall | F1- score |
|-------|-------------------------|----------------------------|--------------------------------|-----------|--------|-----------|
| Car | 673 | 676 | 664 | 0.982 | 0.987 | 0.984 |
| Bus | 7 | 7 | 7 | 1.000 | 1.000 | 1.000 |
| Truck | 111 | 108 | 99 | 0.917 | 0.892 | 0.904 |
| All | 791 | 791 | 770 | 0.973 | 0.973 | 0.973 |



※The license plate is manually masked

Fig.6. Examples of images misclassified as car

4. Conclusion

In this study, a method for measuring turning movement counts by vehicle type was developed using deep learning techniques. The results of the empirical experiments demonstrated that implementing an interpolation process to estimate the inflow direction from the outflow direction improved the counting accuracy for left-turning vehicles and occluded vehicles, which had been a limitation of existing methods. Furthermore, it was demonstrated that, except for one direction, the method achieved a counting accuracy equivalent to or exceeding 95.0%, which is the accuracy level typically achieved through manual measurement. In addition, using the existing YOLOv8x model, the method successfully classified the three classes—car, bus, and truck—with an accuracy exceeding 90.0%. In the future, a method will be devised to prevent overcounting by focusing on the upper edge of the bounding boxes during detection. Furthermore, the generalizability of the proposed method will be validated by applying it to videos captured from various angles and under diverse traffic conditions. Additionally, a method will be developed for measuring turning movement counts separately for small and large vehicles using image classification techniques, aiming for practical application in turning movement counts surveys.

Author Contributions

Conceptualization, Y.Y., M.N., R.S., W.J., D.K., and R.I.; methodology, Y.Y., M.N., R.S., W.J., D.K., and R.I.; software, Y.Y., M.N. and R.S.; validation, Y.Y., M.N., R.S., W.J., D.K., and R.I.; formal analysis, Y.Y., M.N., R.S., W.J., D.K., and R.I.; investigation, Y.Y., M.N., R.S., W.J., D.K., and R.I.; resources, Y.Y., M.N., W.J., D.K., and R.I.; data curation, Y.Y., M.N., R.S., W.J., D.K., and R.I.; writing—original draft preparation, R.S.; writing—review and editing, Y.Y., M.N., R.S., W.J., D.K., and R.I.; visualization, Y.Y., M.N., R.S., W.J., D.K., and R.I.; supervision, R.I.; project administration, R.I.; funding acquisition, Y.Y., M.N., W.J., D.K., and R.I. All authors have read and agreed to the published version of the manuscript.

Funding

This research received no external funding.

A Study on the Development of a Traffic Volume Counting Method by Vehicle Type and Direction
Using Deep Learning

Yamamoto, Y., Nakahara, M., Sumiyoshi, R., Jiang, W., Kamiya, D. and Imai, R.

Acknowledgments

We would like to express our gratitude to SURVEY RESEARCH CENTER Co., Ltd., CHUO KENSETSU CONSULTANT. Co., Ltd., and NIPPON INSIEK Co., Ltd., for providing us with video images and advice for the practical application of this study.

Conflicts of Interest

The authors declare no conflicts of interest.

References

- Aharon, N., Orfaig, R. and Bobrovshy, B, Z. (2022). BoT-SORT: Robust associations multi-pedestrian tracking. <https://arxiv.org/abs/2206.14651>
- Hamamura, S., Abe, K., Yamane, S. and Nakamura, H. (2023). Development of a real-time cross-sectional traffic volume measurement system using AI. *Intelligence, Informatics and Infrastructure*, 4(3), 458-465. (in Japanese)
- Horii, D., Sugawara H., Kikuchi, Y. and Okubo J. (2022). A study on automatic measurement of precise traffic engineering indicators volume by intersection direction using deep learning. *Intelligence, Informatics and Infrastructure*, 3(J2), 819–825. (in Japanese)
- Japan International Cooperation Agency. (2018). Traffic surveys and traffic demand forecasting studies in developing countries. <https://openjicareport.jica.go.jp/pdf/12339867.pdf> (in Japanese)
- Jocher, G., Chaurasia, A. and Jing qiu. (2023). Ultralytics YOLOv8, <https://github.com/ultralytics/ultralytics>
- Metropolitan Police Department. (2023). Traffic Volume Statistics Table. https://www.keishicho.metro.tokyo.lg.jp/about_mpd/jokyo_tokei/tokei_jokyo/ryo.html (in Japanese)
- Ministry of Land, Infrastructure, Transport and Tourism. (2019). Direction of Traffic Volume and Travel Speed Survey Utilizing ICT. <https://www.mlit.go.jp/road/ir/ir-council/ict/pdf03/02.pdf> (in Japanese)
- Okubo, J., Sugawara, H., Fujii, J. and Ozasa, K. (2020). Object Tracking on Traffic Counting Improve Method. *Intelligence, Informatics and Infrastructure*, 1(1), 235-241. (in Japanese)
- Shiomi, Y. (2022). Estimation on Intersection Turning Volume by Using Traffic Detector and Probe Data. *Journal of Traffic Engineering*, 8(2), A_213-A_221. (in Japanese)
- Streetlight Data. (2024). Turning Movement Counts Explained: Leveraging TMC Analytics for Better, Safer Planning. <https://www.streetlightdata.com/turning-movement-count-analytics-explained/>
- Sumiyoshi, R., Imai, R., Yamamoto, Y., Nakahara, M., Kamiya, D. and Wenyuan, J. (2024). Fundamental Study on Automated Counting Method of Turning Movement Counts at Intersections Using Video Images. *Journal of Digital Life*. (in Japanese)
- Varghese, R. and Sambath, M. (2024). YOLOv8: A Novel Object Detection Algorithm with Enhanced Performance and Robustness, *2024 International Conference on Advances in Data Engineering and Intelligent Computing Systems*, 10.1109/ADICS58448.2024.10533619
- Watanabe, K., Nakano, K., Nakazawa, M. and Naganuma, K. (2023). Development and its evaluation of a counterline optimization method for directional traffic surveys using MOT. *Transactions of Information Processing Society of Japan*, 64(2), 511–520. (in Japanese)

Special Issue: Measurement, control, and analysis of motion using ICT and AI
Article

Detecting Near-Miss Actions and Estimating Physical Fatigue among Construction Workers Using Wearable Sensors

Yoshimasa Umehara ¹, Toshio Teraguchi ², Yuhei Yamamoto ³, Taiga Kobayashi ⁴ and Ryuichi Imai ^{5*}

¹Faculty of Business Administration, Setsunan University, 17-8 Ikeda-nakamachi, Neyagawa-shi, Osaka 572-8508, Japan

²Faculty of Economics, University of Marketing and Distribution Sciences, 3-1 Gakuen-nishimachi, Nishi-ku, Kobe-shi, Hyogo 651-2188, Japan

³Faculty of Environmental and Urban Engineering Department of Civil, Kansai University, 3-3-35 Yamate-cho, Suita-shi, Osaka 564-8680, Japan

⁴Graduate School of Engineering and Design, Hosei University, 2-33 Ichigaya-tamachi, Shinjuku-ku, Tokyo 162-0843, Japan

⁵Faculty of Engineering and Design, Hosei University, 2-33 Ichigaya-tamachi, Shinjuku-ku, Tokyo 162-0843, Japan

Abstract

Labor shortages in the construction industry have become a serious issue in developed countries, particularly in Japan, where workforce aging and declining recruitment of young workers are significant challenges. In this context, ensuring worker safety has become increasingly critical. While occupational accidents in Japan's construction industry have decreased annually due to proper safety measures, the construction industry still has the highest number of fatalities among all industries. Falls from height and falls on the same level are the leading causes of injuries and fatalities. Therefore, detecting near-miss incidents (such as tripping and slipping) that precede falls, along with physical fatigue, could help prevent occupational accidents. This study investigated the feasibility of detecting near-miss incidents and estimating fatigue levels using wearable sensors suitable for continuous monitoring at construction sites. We conducted validation experiments simulating near-miss actions and fatigue conditions. Results showed that applying a Convolutional Neural Network (CNN) to data collected from an iPhone[®] placed in workers' trouser pockets achieved an F1-score of 0.95 in detecting near-miss actions. Additionally, by comparing body sway magnitudes before and after fatigue, we confirmed the potential for estimating physical fatigue.

Keywords: *Machine Learning, Human Activity Recognition, Fatigue Estimation, Wearable Sensor, Near-Miss Action*

1. Introduction

While global economic growth has led to increased construction demand, the construction industry in developed countries faces severe labor shortages. In the United States, the Infrastructure Investment and Jobs Act of 2021 has outlined a \$1.2 trillion infrastructure development plan. However, 88% of U.S. construction companies are experiencing difficulties in securing construction workers (Associated General Contractors of America, 2023). Under these circumstances, Japan's Ministry of Land, Infrastructure, Transport and Tourism is promoting i-Construction to improve safety and labor productivity in the construction industry, resulting in a 6.6% decrease in workplace accidents compared to 2018 (Ministry of Health, Labour and Welfare, 2023a). This reduction can be attributed to the implementation of safety measures, such as KY (*Kiken Yochi*, or hazard prediction) activities that anticipate potential dangers at construction sites and 5S (Sort, Set in order, Shine, Standardize, and Sustain) activities that focus on organization and cleanliness, which are well-known among site managers. Moreover, the Ministry of Health, Labour

Received: 21 November 2024, Revised: 29 January 2025, Accepted: 27 February 2025, Published: 26 March 2025

* Correspondence: imai@hosei.ac.jp

Publisher's Note: JOURNAL OF DIGITAL LIFE. stays neutral with regard to jurisdictional claims in published maps and institutional affiliations.



Copyright: © SANKEI DIGITAL INC. Submitted for possible open access publication under the terms and conditions of the Creative Commons Attribution (CC BY) license (<https://creativecommons.org/licenses/by/4.0/>).

and Welfare formulated the 14th Occupational Safety & Health Program (Ministry of Health, Labour and Welfare, 2023b) in April 2023, which emphasizes the promotion of digital transformation. This program encourages the introduction of cutting-edge technologies for safety measures, such as proximity detection of workers using ICT construction machinery and management of workers' locations and vital data using wearable sensors. These initiatives are believed to contribute to the reduction in the number of occupational accidents. However, the construction industry still has the highest number of fatalities among all industries (Ministry of Health, Labour and Welfare, 2023a). This can be attributed to the inherently high-risk nature of construction work, which involves tasks such as working at heights and operating heavy machinery. Furthermore, physical fatigue resulting from manual labor is believed to affect workers' attentiveness and concentration levels, potentially leading to accidents. According to Heinrich's Law (Heinrich, 1931), a well-known empirical rule in occupational safety, for every serious accident, there are 29 minor accidents, and behind these, there are 300 near-miss incidents. Near-miss incidents in the construction industry include reports of cargo collapse during material loading and cases where outriggers, used to ensure the stability of mobile cranes, sink into the ground (Ministry of Health, Labour and Welfare, 2012). Furthermore, focusing on the factors of occupational accidents that occur in the construction industry, falls from height are the most frequent, followed by falls on the same level (Ministry of Health, Labour and Welfare, 2023a). Therefore, it can be inferred that safety management through dynamic monitoring of construction workers is important. Thus, detecting near-miss actions such as stumbles and slips, which are precursors to falls and trips, could enable the prevention of occupational accidents before they occur. Moreover, estimating the fatigue level of construction workers could help reduce the risk of occupational accidents. By detecting near-miss actions and estimating worker fatigue, the number of occupational accidents can be decreased, and fatalities can be prevented, thereby contributing to the improvement of safety at construction sites. Moreover, estimating the fatigue level of construction workers could help reduce the risk of occupational accidents. By detecting near-miss incidents and estimating worker fatigue, the number of occupational accidents can be decreased, and fatalities can be prevented, thereby contributing to the improvement of safety at construction sites.

In existing research, detecting near-miss actions and estimating physical fatigue have been approached through distinct methodologies. First, focusing on the detection of near-miss actions among construction workers, given that occupational accidents in the construction industry frequently involve falls from height and falls on the same level (Ministry of Health, Labour and Welfare, 2023a), the implementation of wearable sensors has been proposed as a means of detecting falls. Notable examples of wearable sensors currently deployed at construction sites include the Spot-r by Triax Technologies, Inc., and the fall detection device by Takenaka Engineering Co., Ltd. On the other hand, fall detection methods using cameras and LiDAR, which offer higher visibility compared to wearable sensors, have become widespread in the healthcare and welfare sectors, notably the mirAI-EYE by GLORY Ltd., and fall detection sensor for elderly people by FAJ Inc. However, these methods are designed for care recipients and can only be applied in stable environments without blind spots, with a detection range of within 7 meters. Therefore, their adoption in construction sites is hindered by the occurrence of blind spots due to complex structures and the difficulty of wide-area detection. Murata Manufacturing Co., Ltd., has developed a worker safety monitoring system as a wearable sensor capable of detecting near-miss incidents such as trips and slips that may precede falls on construction sites. However, the specific definitions of near-miss actions and their detection algorithms have not been made public. Therefore, we focus on fall and near-miss action detection methods in the sports and welfare fields, where action recognition research has been advancing. In the field of sports, a method for detecting falls of soccer players using the deep learning model LSTM (Naruo et al., 2023) has been devised. The reason this method is effective is that soccer has a limited duration and range of movement, and the players' motion patterns are relatively consistent. On the other hand, LSTM learns patterns from long-term time-series data. Therefore, we infer that it would be difficult to apply this method to construction workers, whose behavior varies greatly depending on differences in site terrain, structure, equipment used, and job type. In the welfare field, methods for detecting near-miss actions using machine learning models, such as SVM and Decision Tree, as well as thresholds (Pang et al., 2019), have been devised. However, these methods are limited to elderly individuals during walking or daily activities. Consequently, they are difficult to apply to construction workers, who exhibit a wide range of complex behaviors, such as working at heights or operating heavy machinery. Therefore, we believe that by proposing a method suitable for detecting near-miss actions of construction workers who perform a wide variety of tasks, we can contribute to the prevention of occupational accidents.

Next, we focus on estimating the fatigue level of construction workers. Generally, in fatigue level estimation, analyses based on physiological indicators from vital sensors, such as heart rate, electromyography, and oxygen consumption, are conducted. However, the utilization of vital sensors remains challenging on construction sites due to factors such as the impact on heart rate for specific occupations (Akagawa et al., 2020) and the contact between fall protection equipment and vital sensors. Consequently, there are still issues hindering their widespread adoption. In the field of sports, where research on fatigue level estimation has been advancing, it is possible to estimate fatigue levels based

on exercise load by calculating the amount of exercise from the distance and speed of movement during play, measured using wearable sensors (Yamada et al., 2023). However, the amount of exercise used for estimating fatigue levels is currently calculated from the distance traveled obtained by GNSS positioning (Yamada et al., 2023). This method is difficult to apply to construction sites with complex structures where multipath effects are likely to occur. As a fatigue estimation method that does not use GNSS positioning, there is a method for estimating fatigue levels by measuring body sway using a force plate, since body sway increases with muscle fatigue (Paillard, 2012). Specifically, body sway is measured by having subjects stand upright on a force plate for 30 seconds before and after fatigue. The fatigued state is reproduced by running on a treadmill for 30 minutes, and the results of the experiment show that body sway significantly increases after fatigue (Derave et al., 2002). However, current methods for measuring body sway are limited to precise methods using force plates or cameras, and a method for measuring body sway using wearable sensors has not yet been established. Therefore, if it becomes clear that the fatigue level of construction workers can be estimated based on body sway, which can be measured by wearable sensors, it will be possible to take breaks and reallocate workers according to their fatigue level, which is expected to help prevent the risk of occupational accidents.

Based on the above, this study aimed to investigate the possibility of detecting near-miss actions and estimating fatigue levels by measuring body sway using wearable sensors that enable continuous monitoring even on construction sites where environmental conditions change daily due to ongoing construction work.

2. Methods

2.1 Methods for Detecting Near-Miss Actions

Near-miss action detection is performed utilizing a deep learning model that has been trained to recognize near-miss action patterns. Our approach to near-miss action detection draws upon anomaly detection methodologies from medical and mechanical domains (Masetic et al., 2016), as well as action recognition techniques employing wearable sensors (Inoue, 2016). In accordance with the methodologies, our study employed wearable sensors to acquire triaxial acceleration and triaxial angular velocity measurements. Subsequently, machine learning models were applied to the acquired data. The study evaluated two candidate machine learning models—Random Forest and Convolutional Neural Network (CNN) classifiers—through empirical experimentation to determine the most effective approach for near-miss action detection. The rationale for employing Random Forest lies in its dual advantages: superior generalization performance with overfitting prevention, and computational efficiency. Our Random Forest data application process involves converting and standardizing integer raw data. During the segmentation phase, we calculate statistical features such as maximum, minimum, mean, standard deviation, and interquartile range. In addition to these features, the unit-converted raw data is used as explanatory variables. The reason for using these features is that previous research (Bao et al., 2004) suggests the possibility of classifying operations with high accuracy. Furthermore, although previous research (Bao et al., 2004) indicates the potential effectiveness of FFT-based features, we do not use them in this study because our preliminary experiments showed that similar features were obtained during near-miss incidents and work operations, which could negatively affect model training. The Random Forest parameters were set according to previous research (Breiman, 2001) as follows: the number of trees was set to 100, the random seed was fixed at 42, the Gini function was used as the split criterion, while both the maximum tree depth and the number of features were set to auto-tune.

The adoption of Convolutional Neural Network (CNN) is justified by their capability to effectively learn spatiotemporal features from sensor data through convolutional and pooling layers, as well as their superior performance in action and image recognition tasks. The data processing pipeline for CNN implementation involves unit conversion of raw integer data followed by standardization to generate the explanatory variables. The CNN architecture consists of three convolutional layers and two fully connected layers, following the structure proposed by Zeng (2014). The CNN hyperparameters were configured based on Zeng (2014) as follows: learning rate was set to 0.001 with Adam optimizer for learning rate decay, ReLU was used as the activation function, and cross-entropy was employed as the loss function. The batch size was set to 10, and the model was trained for 1,000 epochs. For early stopping, we set the patience parameter to 30 with a delta value of 0.00001.

2.2 Methods for Estimating Fatigue Levels

In this study, fatigue levels are defined as the amount of change in body sway before and after exercise, and evaluated by comparing the measurement results of body sway before and after exercise. The method for measuring body sway draws from measurement techniques in medical research, including postural sway measurement during quiet standing (Demura et al., 2006) and gait analysis methods based on long-duration walking rhythm patterns (Higashi et al., 2011). These methods analyze parameters such as the geometrical patterns of the center of gravity sway plotted in two dimensions and peak acceleration during the swing phase. However, these methods are difficult to apply to measuring

construction workers' body sway as they were conducted under stable conditions that substantially differ from construction site environments. Therefore, this study aims to investigate the feasibility of fatigue estimation by developing a robust and easily applicable method for measuring body sway that can accommodate the variable conditions of construction sites, considering fatigue induced by construction work. The body sway measurement method proposed in this study calculates the mean of differences between moving maximum and minimum values at 3-second intervals from tri-axial acceleration and tri-axial angular velocity data obtained through wearable sensors. If this mean value changes in accordance with the accumulation of worker fatigue and increased physical load, we hypothesize that fatigue levels could potentially be estimated through body sway measurements.

3. Experiment

3.1 Detecting Near-Miss Actions Experiment

The objective of this experiment was to investigate the feasibility of detecting near-miss actions by having participants perform simulated near-miss actions while wearing three different types of wearable sensors.

3.1.1 Experimental Setup and Procedure

The experiment was conducted in front of the Hosei University Shinmitsuke building, under experimental conditions, where near-miss actions and work actions were simulated and performed. By applying Random Forest and CNN to the tri-axial acceleration and tri-axial angular velocity data acquired by three types of wearable sensors during the execution of each action, we verified the wearable sensor and machine learning model suitable for detecting near-miss actions. Table. 1 shows the defined near-miss actions and work actions. Near-miss actions were defined as fall, trip, slip, stagger, and run, which are the most common precursors to falls from height and falls on the same level, which are the most frequent causes of occupational accidents. In addition, there are a vast number of types of work actions performed by construction workers. Therefore, in this study, in order to verify the usefulness of the proposed method, work actions similar to near-miss actions were selected. The work actions were defined as stand up, squat down, sit down, get on all fours, lie down, walk, walk while squatting, crawl under obstacles, and step over obstacles. By simulating the execution of these defined actions and classifying them into two categories: work actions and near-miss actions, we attempted to detect near-miss actions. The number of measurements was 5 times for each of the 9 types of work actions and 10 times for each of the 5 types of near-miss actions per person. By visually checking the videos taken during these measurements and extracting the moments of action, ground truth labels were assigned. The

Table.1 Defined work action and near-miss action

| Category | Action |
|------------------|-----------------------|
| Near-Miss Action | Fall |
| | Trip |
| | Slip |
| | Stagger |
| | Run |
| Work Action | Stand up |
| | Squat Down |
| | Sit down |
| | Get on all fours |
| | Lie down |
| | Walk |
| | Walk while squatting |
| | Crawl under obstacles |
| | Step over obstacles |

measurement time of the extracted work actions and near-miss actions was approximately 3 minutes per person for both.

3.1.2 Materials and Participants

The three types of wearable sensors used in this experiment were: the xG-1 (Yamada et al., 2023) by xSENSING Co., Ltd., as a sports activity tracker used for analyzing exercise and play activities; the iPhone® 12 Pro by Apple Inc. as a smartphone sensor integrated into daily life; and the Apple Watch® Ultra by Apple Inc. as a smartwatch capable of measuring vital signs. The positioning of the wearable sensors is shown in Fig. 1. These three types of wearable sensors were selected because each possesses distinct characteristics, allowing us to determine which wearable sensor is most suitable for detecting near-miss actions. The specific characteristics of each wearable sensor are as follows: the xG-1, attached to the back of the body using a dedicated vest, can acquire high-precision motion data during physical activities; the iPhone® can easily collect everyday motion data; and the Apple Watch® can capture hand movement data during tasks. These wearable sensors were used to collect three-axis acceleration and three-axis angular velocity data at a sampling rate of 50 Hz. The subjects were eight male university students in their 20s, all of whom performed near-miss actions and work actions.

3.1.3 Data Processing and Evaluation

When applying machine learning models, segmentation must be performed on the wearable sensor data where action boundaries are ambiguous before data can be processed. The segmentation process is conceptually illustrated in Fig. 2. As reported in existing literature (Inoue, 2016), conventional segmentation methods typically employ fixed-size windows with constant overlap ratios for data processing. In previous research (Huynh et al., 2005), daily actions were identified by fixing the window slide width to 250ms and setting the window size to 250ms, 500ms, 1,000ms, 2,000ms, and 4,000ms. However, it has been shown that the optimal window size varies for each action, and appropriate settings for the detection target are important. Similarly, the window overlap ratio also requires settings appropriate for the detection target (Inoue, 2016). Based on these findings, since near-miss actions are instantaneous actions, we set the window size to 200ms, 500ms, 1,000ms, and 2,000ms, which are narrower than those in previous research (Huynh et al., 2005), and the overlap ratio to 0%, 30%, 60%, and 90%. We constructed 16 models for each of Random Forest and CNN, for a total of 32 models. By verifying the detection accuracy of near-miss actions using these 32 models, we aim to identify the machine learning model and the window size/overlap ratio during segmentation that are suitable for detecting near-miss actions. The training data for model construction consisted of 7 out of 8 subjects, and the test data consisted of the remaining 1 subject.

For detection accuracy evaluation, we use the F1-score, which is the harmonic mean of precision and recall, with values closer to 1 indicating higher accuracy. The evaluation method compares predicted labels from each window with ground truth labels at each data point. When windows overlap, resulting in multiple predictions for a single data point, the final prediction is determined by majority voting.



Fig.1 Placement of wearable sensors

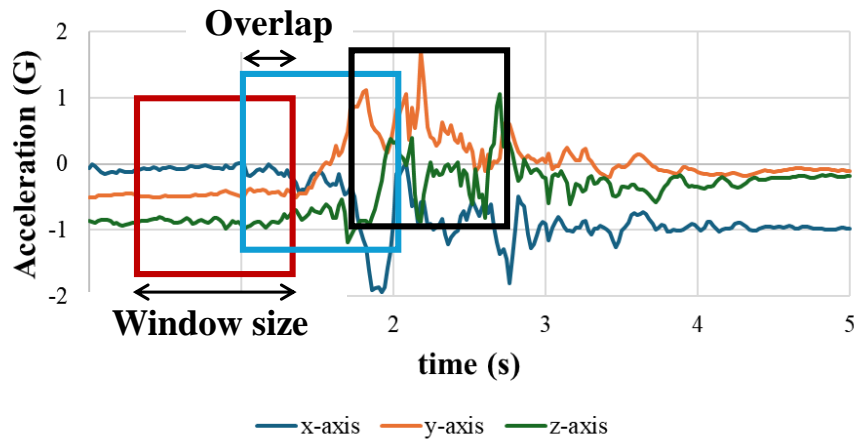


Fig.2 Segmentation image during data loading

3.2 Estimating Fatigue Levels Experiment

The objective of this experiment is to investigate the possibility of estimating fatigue levels by measuring and comparing body sway before and after fatigue using wearable sensors.

3.2.1 Experimental Setup and Procedure

The experiment was conducted in front of the Hosei University Sinmitsuke building. The subject ran 5 km in approximately 20 minutes to induce a state of fatigue. The same actions were performed before and after fatigue, and the change in the amount of body sway was compared. The actions for measuring body sway before and after fatigue were walk, transport, upstairs, and downstairs, which were considered easy to measure body sway due to periodic movements, assuming actual operation at construction sites. Each action was performed at the same pace for 30 seconds before and after fatigue, and data on triaxial acceleration and triaxial angular velocity were acquired.

3.2.2 Materials and Participants

We used xG-1 (Yamada et al., 2023) from xSENSING Co., Ltd., as the wearable sensor. The xG-1 is a sports activity tracker used for analyzing exercise and play patterns, making it suitable for measuring body sway. The sensor placement and data collection methods are identical to those described in Section 3.1.2. The subject was one male student in his 20s.

3.2.3 Data Processing and Evaluation

Since the acquired raw data of triaxial acceleration and triaxial angular velocity are integer values, the integer value of acceleration is converted to G, and the integer value of angular velocity is converted to deg/s. Then, using the proposed method, body sway before and after fatigue is compared, and if a difference is observed between before and after fatigue, it is evaluated that it is possible to estimate the fatigue levels.

4. Results & Discussion

4.1 Experimental Results and Discussion on Detecting Near-Miss Actions

The results of Random Forest application are shown in Fig. 3. In Fig. 3, the left horizontal axis represents the window size, the right horizontal axis shows the overlap rate, and the vertical axis indicates the F1-score, where higher plot points represent higher detection accuracy. The highest detection accuracy was achieved with the xG-1 sensor, using a window size of 200ms and an overlap rate of 90%, resulting in an F1-score of 0.45, indicating that Random Forest could hardly detect near-miss actions. These results suggest that near-miss action detection using Random Forest is challenging. The low detection accuracy of Random Forest can be attributed to two main factors: insufficient utilization of time-series data characteristics and inadequate feature extraction and selection. While Random Forest excels at handling correlations between individual features, it struggles to directly model temporal dependencies. This limitation likely resulted in missing crucial information when detecting near-miss actions, which involve subtle movement changes over short periods. The results of the CNN implementation are presented in Fig. 4. The highest

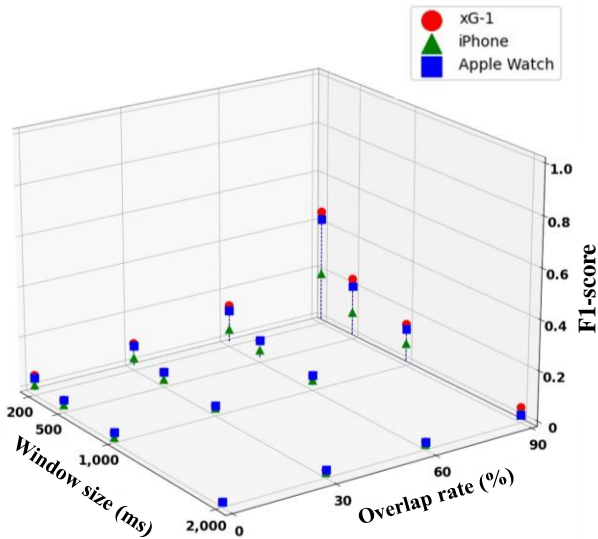


Fig.3 F1-scores for each parameter obtained during Random Forest validation

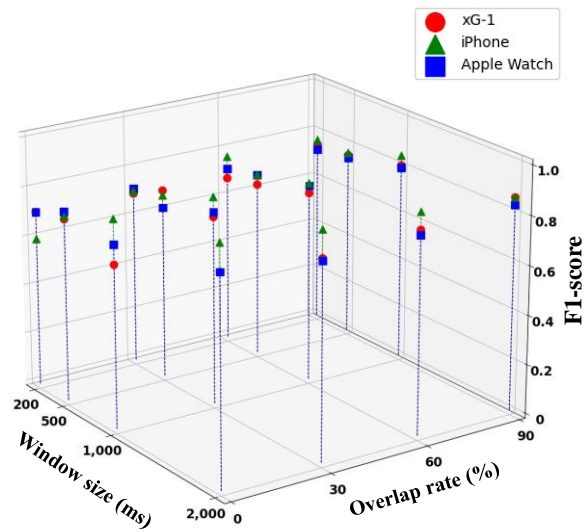


Fig.4 F1-scores for each parameter obtained during CNN validation

detection performance was obtained when using an iPhone® with a window size of 2,000ms and a 0% overlap, achieving an F1-score of 0.95, indicating that CNN effectively detects near-miss actions with high precision. The substantial enhancement in F1-score through CNN implementation can be explained by CNN's inherent capability to recognize local patterns within multidimensional data. The improvement in F1-scores with larger window sizes can be attributed to the increased number of data points, enabling the learning of more features and recognition of overall motion patterns. The F1-score peaked at 0% overlap because each window remains independent, preventing prediction labels from being influenced by other windows. Conversely, when overlap exists, identical data points may be included in multiple windows, potentially resulting in different prediction labels for each window. In this case, prediction labels for identical data points are determined by majority voting, causing incorrect predictions to affect the overall results and decrease accuracy. Therefore, when different prediction labels are obtained for the same data point, alternative methods to majority voting should be considered for label determination. Among wearable sensors, the iPhone® showed the highest detection accuracy when applying CNN. This is likely because near-miss action characteristics are more prominently displayed around the waist area. Furthermore, when comparing detection accuracy across different types of near-miss action, falling motions showed the lowest accuracy. This can be attributed to the similarity between falling motions and lying down actions performed during work tasks.

4.2 Experimental Results and Discussion on Estimating Fatigue Levels

Fig. 5 and 6 present quantitative analyses of relative changes in body sway magnitude, measured via three-axis acceleration and angular velocity, comparing pre- and post-fatigue conditions. The coordinate system establishes the x-axis as an anteroposterior, y-axis as vertical, and z-axis as mediolateral directions. Analysis revealed a consistent pattern of increased post-fatigue body sway across multiple movement patterns, with particular emphasis on carrying out tasks designed to simulate construction worker activities. Stair descent movements exhibited a pronounced susceptibility to increased body sway magnitude. Differential analysis of fatigue-induced changes across individual axes demonstrated minimal perturbation along the vertical y-axis, while substantial variations were observed in both the anteroposterior (x-axis) and mediolateral (z-axis) directions. This axis-specific response pattern can be attributed to the inherent stability of vertical components versus the heightened susceptibility of horizontal plane movements to fatigue-induced oscillations. Of particular significance, stair descent movements demonstrated markedly elevated fatigue-induced body sway compared to other assessed movements, suggesting enhanced sensitivity to physical fatigue. This heightened response during stair descent can be mechanistically linked to the substantial energetic demands associated with controlled vertical displacement during the movement sequence.

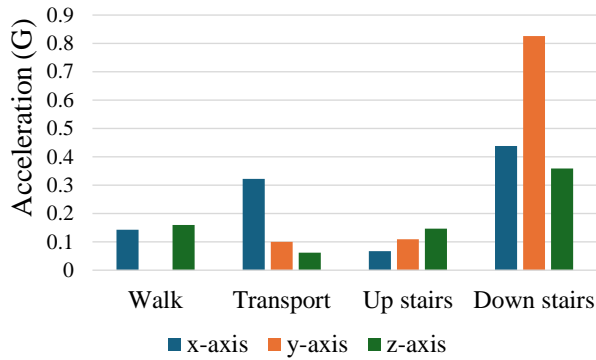


Fig.5 Relative changes in acceleration before and after fatigue

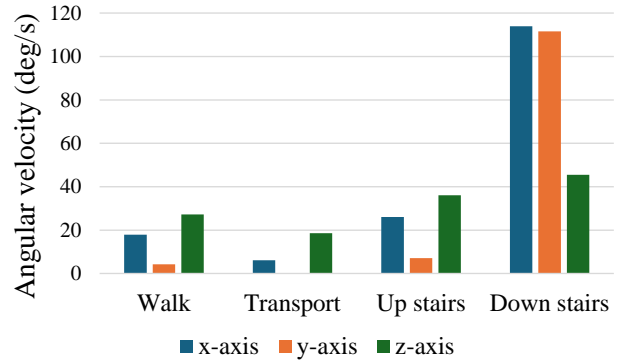


Fig.6 Relative changes in angular velocity before and after fatigue

4.3 Discussion on Generalizing to Actual Construction Environments

In this study, we verified the possibility of detecting near-miss actions and estimating fatigue levels in an experimental environment with limited actions. However, since actual construction sites involve a vast variety of actions and diverse environments, we will discuss how the findings obtained in this study can be generalized.

In detecting near-miss actions, actual construction sites involve work at heights, work in unstable locations such as scaffolding, and work performed by multiple people. Therefore, even if the same action is performed, the actual behavior may differ. Thus, we infer that the robustness of near-miss actions detection can be improved by collecting comprehensive action data of actual construction workers and building a model.

In estimating fatigue levels, this study measured body sway for periodic actions. Since it was shown that body sway increases after fatigue in the action of going down the stairs, the proposed fatigue level estimation method may be applicable to actions that are periodic and require balance at actual construction sites. However, this study used student subjects in their 20s, and it is necessary to consider individual differences due to the diverse age groups and physiques of construction workers in actual operation. Therefore, it is considered that it is possible to estimate the fatigue levels corresponding to individual differences by measuring the body sway data in the state before fatigue of each individual and calculating the amount of increase in body sway by comparing it with that.

5. Conclusion

In this study, we investigated the feasibility of detecting near-miss actions and estimating physical fatigue levels using wearable sensors suitable for continuous monitoring at construction sites. Initially, we evaluated various wearable sensors, machine learning models, and segmentation methods appropriate for near-miss action detection. The results demonstrated that applying CNN to data collected from an iPhone® placed in a trouser pocket achieved near-miss action detection with an F1-score of 0.95. This suggests that our proposed detection method could effectively identify near-miss actions at construction sites. Furthermore, the use of smartphones as familiar, unobtrusive sensors integrated into daily life could facilitate widespread adoption among construction workers, potentially contributing to accident prevention in construction environments.

Subsequently, we examined the possibility of fatigue estimation using the xG-1 sports activity tracker. The results indicated that physically demanding activities, such as descending stairs and carrying loads, exhibited notably increased body sway under fatigue conditions. This suggests the potential for estimating construction workers' fatigue levels during their duties. Such fatigue estimation could enable improved site management through appropriate worker allocation, particularly for those prone to fatigue, thereby preventing accidents proactively.

Future research will focus on validating near-miss action detection and fatigue estimation capabilities using data collected from actual construction sites. Additionally, we plan to estimate near-miss action locations through GNSS positioning and correlate them with site conditions to establish the practical applicability of our detection method. Furthermore, we will assess the effectiveness of our fatigue estimation approach by comparing estimated fatigue levels with subjective fatigue assessments obtained through worker questionnaires.

Author Contributions

Conceptualization, Y.U., T.T., Y.Y., T.K. and R.I.; methodology, Y.U., T.T., T.K. and R.I.; validation, Y.U., T.T., Y.Y., T.K. and R.I.; formal analysis, Y.U., T.T., Y.Y., T.K. and R.I.; investigation, T.K.; resources, R.I.; data curation, T.K.; writing—original draft preparation, T.K.; writing—review and editing, Y.U., T.T., Y.Y., T.K. and R.I.; project administration, R.I.; All authors have read and agreed to the published version of the manuscript.

Funding

This research received no external funding.

Institutional Review Board Statement

The study was conducted according to the Declaration of Helsinki.

Informed Consent Statement

Informed consent was obtained from all subjects involved in the study.

Acknowledgments

We would like to express our gratitude to xSENSING Co., Ltd., for providing valuable insights into the data characteristics of wearable sports sensors during the execution of this study.

Conflicts of Interest

The authors declare no conflicts of interest.

References

- Akagawa, H., Kasai, Y., Iizuka, K., Yamada, S. and Morikawa, N. (2020). Study on Heart Rate Characteristics of Construction Workers Under Hot Conditions. *Report of Obayashi Corporation Technical Research Institute*, 84(1). (in Japanese)
- Bao, L. and Intille, S. S. (2004). Activity Recognition from User-Annotated Acceleration Data. *Lecture Notes in Computer Science*, 3001, 1-17.
- Breiman, L. (2001). Random Forests. *Machine Learning*, 45(1), 5-32.
- Demura, S., Kitabayashi, T. and Noda, M. (2006). Measurement and Evaluation of Healthy People's Body-sway. *The Journal of Education and Health Science*, 51(3), 223-233. (in Japanese)
- Derave, W., Tombeux, N., Cottyn, J., Pannier, J. L., and De Clercq, D. (2002). Treadmill Exercise Negatively Affects Visual Contribution to Static Postural Stability. *International Journal of Sports Medicine*, 23(1), 44-49.
- Heinrich, H. W. (1931). *Industrial Accident Prevention: A Scientific Approach*, McGraw-Hill.
- Higashi, H., Shigeoka, T., Itokawa, T., Kitasuka, T. and Aritsugi, M. (2011). A Consideration of Features for Fatigue Estimation by Gait Analysis Using Accelerometer. *The Special Interest Group Technical Reports of IPSJ*, 2011-MBL-57(27), 1-8. (in Japanese)
- Huynh, T. and Schiele, B. (2005). Analyzing Features for Activity Recognition. *Proceedings of the 2005 Joint Conference on Smart Objects and Ambient Intelligence: Innovative Contextaware Services: Usages and Technologies (sOc-EUSAI '05)*. 159-163.
- Inoue, S. (2016). Human Sensing with Wearable Sensors. *Journal of Japan Society for Fuzzy Theory and Intelligent Informatics*, 28(6), 170-186. (in Japanese)
- Ishioka, H. (2020). AI for Digitization of Construction Management: Single Camera Worker Detection, Tracking and Action Recognition in Construction Site. *Technical Research Report of Shimizu Construction Co., Ltd.*, 98(1), 21-30. (in Japanese)

- Masetic, Z. and Subasi, A. (2016). Congestive Heart Failure Detection Using Random Forest Classifier. *Computer Methods and Programs in Biomedicine*, 130, 54-64.
- Ministry of Health, Labour and Welfare. (2012). Visualization of Near-Miss Cases for Participation in Safety and Health Activities, https://safeconsortium.mhlw.go.jp/anzenproject/concour/2012/sakuhin4/images/n096_2.pdf (in Japanese)
- Ministry of Health, Labour and Welfare. (2023a). Analysis of Occupational Accidents in 2023. <https://www.mhlw.go.jp/content/11302000/001099504.pdf> (in Japanese)
- Ministry of Health, Labour and Welfare. (2023b). The 14th Occupational Safety & Health Program. <https://www.mhlw.go.jp/content/11200000/001253683.pdf>
- Naruo, T., Yamamoto, Y., Jiang W., Sakamoto, K., Nakamura, K., Tanaka, S., Okazaki, Y. and Yamazaki, Y. (2023). "Research for Detecting Falling of Soccer Players from IMU using LSTM". *Proc. 85th National Convention of IPSJ*, 331-332. (in Japanese)
- Paillard, T. (2012). Effect of General and Local Fatigue on Postural Control: A Review: *Neuroscience & Biobehavioral Reviews*, 36(1), 162-176.
- Pang, I., Okubo, Y., Sturnieks, D., Lord, S. R. and Brodie, M. A. (2019). Detection of Near Falls Using Wearable Devices: A Systematic Review. *Journal of Geriatric Physical Therapy*, 42(1), 48-56.
- Yamada, T., Masaki, H., Matsubayashi, Y., Tanaka, S., Imai, R., Naruo, T., Nakamura, K., Yamamoto, Y., Jiang, W. and Tanaka, C. (2023). Development of Sensing Unit "xG-1" for Visualizing Team Plays. *Journal of Digital Life*, 3, 10.
- Zeng, M., Nguyen, L. T., Yu, B., Mengshoel, O. J., Zhu, J., Wu, P. and Zhang, J. (2014). Convolutional Neural Networks for Human Activity Recognition Using Mobile Sensors. *Proceedings of the 6th International Conference on Mobile Computing, Applications and Services (MobiCASE)*, 197-205.

Special Issue: Measurement, control, and analysis of motion using ICT and AI
Article

Challenges of Tourists Evacuation in Tsunami Considering with Population Distribution

Atsushi Uechi ^{1*}, Daisuke Kamiya ¹ and Rinka Arakaki ¹

¹Faculty of Engineering, University of the Ryukyus, 1 Senbaru, Nishihara, Okinawa, 903-0213, Japan

Abstract

Tourist attractions on islands are concentrated in coastal areas, and tourists are at high risk of being struck by a tsunami. It is acknowledged that tourists, due to their unfamiliarity with the area, may benefit from the evacuation guidance provided by residents. However, it is important to note that numerous issues persist within the current disaster risk reduction measures. In this study, the number of disaster victims was clarified based on the distribution of people by time of day in Ishigaki city and Miyakojima city, Okinawa Prefecture. From the perspective of evacuation support, the overlap between residents and tourists was analyzed using a “niche overlap index” to identify areas where evacuation guidance by residents is difficult and areas and time periods where support can be expected.

Keywords: evacuation assistance; resident; tourist; tsunami evacuation; island tourism region.

1. Introduction

The 2004 Sumatra earthquake resulted in an unparalleled tsunami that caused damage to countries along the Indian Ocean coast (Kawata, 2005). The tsunami that struck Phuket, Thailand, a world-class tourist destination, resulted in the loss of life not only among the local population but also among numerous tourists from abroad. This large-scale disaster has served to underscore the critical importance of “tourism risk management” in tourist destinations on a global scale.

The concept of tourism crisis management has been a subject of active discussion in countries where tourism constitutes a significant industry. The establishment of a crisis management system is imperative to ensure the sustainability of the tourism industry. Beirman, D., “Crisis Management in Tourism” aims to present theories and measures for a clearer understanding of consumer, economic, and environmental reactions to crises, and to provide guidelines for relevant operators to prepare for such situations and learn how they should operate during a crisis (Beirman, 2020). It offers a comprehensive guide to assist businesses in preparing for and managing operations during a crisis. (Glaesser, 2006).

Japan is a country that is susceptible to earthquakes, and the resulting tsunami disasters can have a significant impact on regional sustainability. In response to such disasters, hard measures, such as tsunami breakwaters, are being developed. Soft measures are also being implemented, including free pamphlets featuring hazard maps, multilingual evacuation information apps, and voice guidance. However, there are concerns that the construction of tsunami breakwaters in coastal tourist areas will spoil the scenery. Additionally, free newspapers and apps often fail to reach visitors who do not actively seek out information. Furthermore, it takes time for audio guidance to convey information, which poses challenges in terms of effectiveness. As complementary solutions to these limitations, physical support measures such as highly visible pictogram-based evacuation signs and pavement markings are considered effective. These tools are language-independent and involve relatively low costs for installation and maintenance, making them highly feasible even in diverse tourist settings where resources and infrastructure may vary.

Received: 21 November 2024, Revised: 8 July 2025, Accepted: 13 August 2025, Published: 16 September 2025

* Correspondence: uechi_fn9s@cs.u-ryukyu.ac.jp

Publisher's Note: JOURNAL OF DIGITAL LIFE. stays neutral with regard to jurisdictional claims in published maps and institutional affiliations.



Copyright: © SANKEI DIGITAL INC. Submitted for possible open access publication under the terms and conditions of the Creative Commons Attribution (CC BY) license (<https://creativecommons.org/licenses/by/4.0/>).

Tourists, who are generally unfamiliar with the local geography, often do not recognize whether they are located within tsunami inundation zones, and their understanding of evacuation sites tends to be insufficient. Verbal evacuation guidance provided by residents is therefore regarded as a crucial means of supporting the evacuation of tourists. As illustrated by the “Kamaishi Miracle (Katada & Kanai, 2016; Ohsumi et al. 2019)”, verbal evacuation guidance has been shown to exert a more significant psychological effect than announcements disseminated through applications or outdoor speakers. This phenomenon can be attributed to the fact that individuals can physically observe the voices and figures of others fleeing, which serves as a more salient and impactful stimulus.

However, it is impossible to provide verbal evacuation guidance in areas where there are no residents, and it is unrealistic to expect residents to voluntarily evacuate, to reduce the risk of a disaster affecting the entire community, evacuation guidance must be provided in areas without residents. In such areas, highly visible evacuation signs (pictograms) and other means are necessary. When establishing these signs, focus on the temporal and spatial overlap between residents and tourists, and design and place them effectively.

This study aims to clarify the possibility of residents providing evacuation support to tourists in the event of a disaster by analyzing the spatial and temporal overlap between residents and tourists. This will provide basic knowledge for reconsidering evacuation guidance methods in areas and at times when evacuation support from residents cannot be expected and will contribute to the design of disaster mitigation plans and signage plans for tourist destinations.

The structure of this paper is as follows: Section 2 reviews previous studies and presents the position of the present study. Section 3 summarizes the target area for analysis and the outline of the data used. Section 4 clarifies the distribution of the population staying in the target area. Section 5 evaluates evacuation guidance based on the spatiotemporal overlap between residents and tourists using a niche overlap index. Finally, Section 6 discusses the results obtained and future issues. The sixth Section of the study presents the results obtained from research and discusses future issues that require attention.

2. Review of Previous Studies and Positioning of This Study

There are various methods for analyzing human overlaps. For example, there are methods to estimate and visualize spatial human flow density using kernel density estimation (Silverman, 1986), and methods to evaluate coexistence status and degree of concentration using Shannon entropy, an ecological diversity index (Lou, 2006). Kernel density estimation is a statistical method that allows for the evaluation of the spatial density of individual objects. However, it is challenging to demonstrate the overlap between different groups. Additionally, while the Shannon entropy index is capable of quantifying spatial diversity and dispersion, it is challenging to assess the strength of the overlap.

In the domain of mathematical ecology, or ecostatistics, the analysis of niche overlap, which examines the intersection of species' distributions, has been a subject of study since the late 1950s. This field has witnessed the development of numerous overlap indices. In recent years, these indices have been applied to various fields, including biological approaches (Jiménez-Guevara et al., 2024; Shinohara, 2021), studies that evaluated the impact of human activities on local communities (Kajitani et al. 2002), and studies that used them to evaluate urban disaster risks (Okada & Maekawa, 1997).

In the fields of urban planning and transportation, the use of human flow data, which visualizes the movement of people and goods, can be used to provide public transportation services that meet the needs of users and to promote sustainable urban development and regional revitalization. In the field of disaster prevention, human flow data can be used to assess disaster risk and formulate evacuation plans and is becoming increasingly important.

In this study, we examine the “niche overlap index” from the perspective of evacuation support and analyze the overlap in the spatial and temporal distributions of residents and tourists. We believe this approach can evaluate the possibility of residents providing evacuation guidance to tourists and propose a new method for tourists' preliminary risk assessment in the event of a tsunami.

3. Overview of Study Area and Data Used

3.1 Overview of Study Area

As illustrated in Fig. 1, Ishigaki Island and Miyako Island, the target areas of this study, are situated between Okinawa Island and Taiwan, thereby serving as geographical nodes that facilitate connectivity between Japan and Asia. The population of both islands is less than 50,000, and Ishigaki Island receives approximately 1.18 million tourists per year (Ishigaki city, 2023), while Miyako Island receives approximately 930,000 tourists (Miyakojima city, 2023).



Fig.1. Location Map

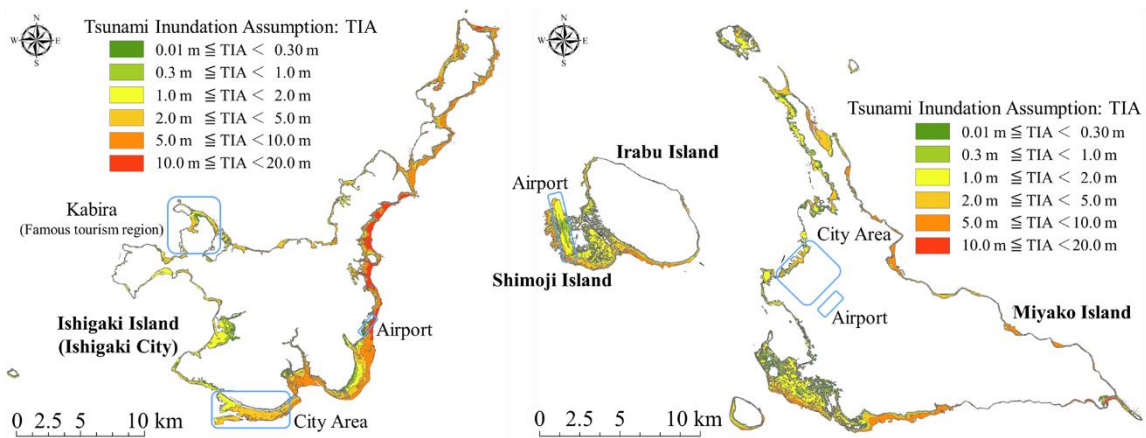


Fig.2. Tsunami inundation assumption map (left: Ishigaki city, right: Miyakojima city)

Table 1. Numbers of data and IDs

| | | Residents | | Tourists | |
|-----------------|---------|----------------|---------------|----------------|---------------|
| | | Number of Data | Number of IDs | Number of Data | Number of IDs |
| Ishigaki city | Spring* | 3,426,058 | 1,102 | 2,099,904 | 9,617 |
| | Summer* | 6,209,351 | 1,582 | 5,397,533 | 13,782 |
| Miyakojima city | Spring* | 3,990,588 | 2,004 | 1,539,528 | 6,209 |
| | Summer* | 10,782,673 | 2,557 | 4,129,987 | 10,067 |

*Spring:2019.02.11~04.07 (56 days), Summer:2019.07.15~09.08 (56 days)

As illustrated in Fig. 2, the eastern coast of Ishigaki city is projected to experience inundation with a height exceeding 20 meters, encompassing the city center and the airport within the tsunami inundation zone. Furthermore, the minimum arrival time of the initial tsunami wave is estimated to be a mere five minutes (Okinawa Prefecture, 2015), underscoring the imperative for expeditious evacuation measures. Conversely, Miyakojima city has a limited area that is expected to be inundated with more than 10 meters of water compared to Ishigaki city. The urban area and the airport are located outside the expected inundation zone. The initial arrival time of the tsunami wave is estimated to be 16 minutes at its shortest, as reported by Okinawa Prefecture in 2015. The potential for damage is lower than that observed in Ishigaki city.

3.2 Overview of Data Used

The data used in this study were application location data provided by Blog Watcher, Inc., and were generated based on information obtained from the GPS capabilities of mobile phones and other devices (Blog Watcher Inc.).

These data were compiled and analyzed for each 500-m grid. The estimated residence of each island was assigned as a resident if inside the island and a tourist if outside the island, and the attribute information was assigned to each

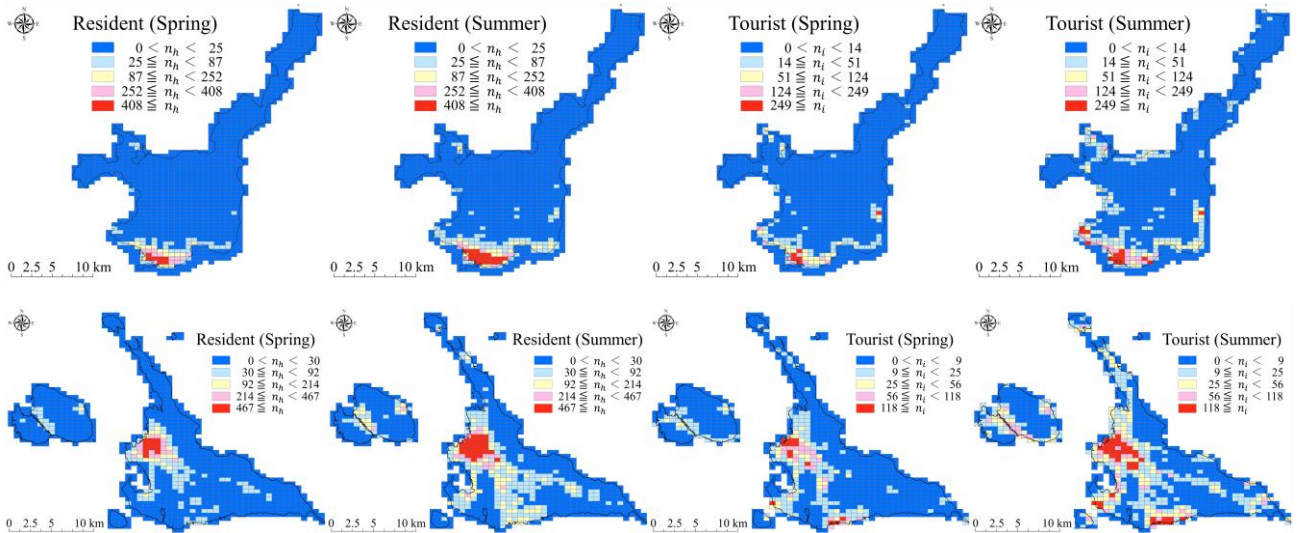


Fig.3. Daily stay population distribution by season (top: Ishigaki city, bottom: Miyakojima city)

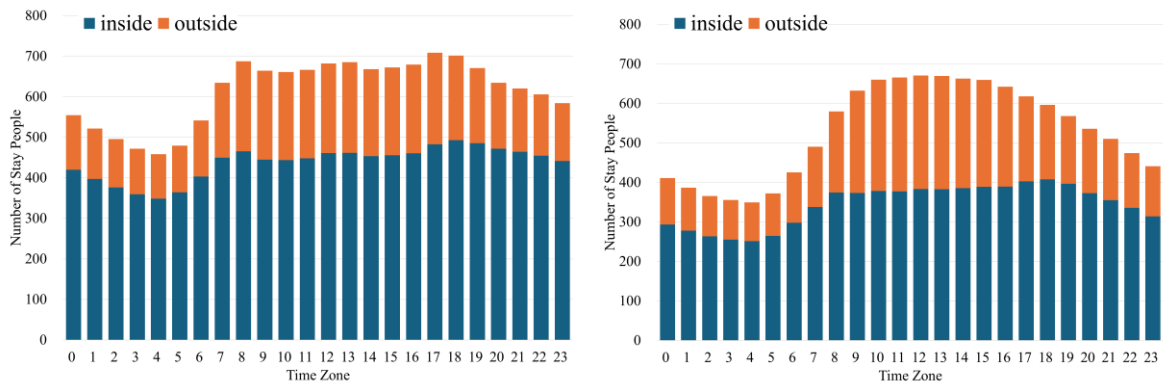


Fig.4. Stay population by time zone in Ishigaki city (left: Resident, right: Tourist)

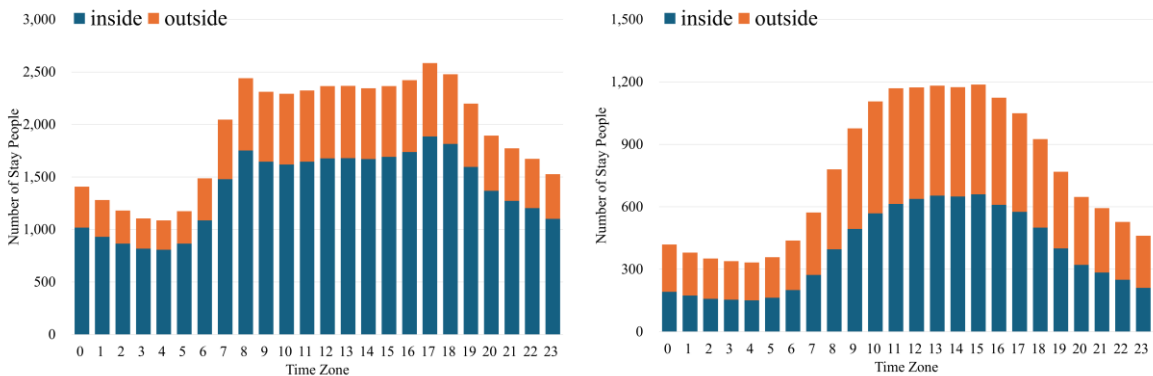


Fig.5. Stay population by time zone in Miyakojima city (left: Resident, right: Tourist)

island. A summary of these data is presented in Table 1. The number of networks analyzed was 1,011 in Ishigaki City and 895 in Miyakojima city.

4. Stay Population Analysis

4.1 Analysis by Season

First, in order to clarify the seasonal differences in the population of residents on the two islands, the daily population of residents by season was calculated. As illustrated in Fig. 3, the distribution of the daily population is examined. A close examination reveals that the distribution of both residents and tourists varies according to the season. A comparison of Ishigaki city and Miyakojima city reveals that the former is particularly concentrated around the urban area, suggesting that tourists are widely distributed in both islands during the summer season.

4.2 Analysis by Time Zone

The population of the two islands by time of day is shown in Fig. 4 for Ishigaki city and Fig. 5 for Miyakojima city. Fig. 4 and 5 illustrate the population of Ishigaki city and Miyakojima city, respectively. A substantial proportion of the population -more than 70% of residents and tourists -resided within the tsunami inundation zone during all time periods. In Miyakojima city, the proportion of residents who remained within the tsunami inundation zone tended to be higher during the nighttime and early morning hours (21:00 to 7:00).

5. Niche Overlap Analysis

5.1 Evaluation Approach

If residents support the evacuation behavior of tourists, this study clarifies the time and areas where evacuation guidance becomes difficult.

In this study, we consider residents and tourists as different species in a tourist area and use the niche overlap index a_{hit} , which is an index of the spatiotemporal overlap of people, to evaluate the risk of tsunami damage to tourists. The index is expressed by the following equations (1) – (3).

$$a_{hit} = \frac{\sum_{j=1}^L \sum_{t=1}^M P_{hjt} P_{ijt}}{\sqrt{\sum_{j=1}^L \sum_{t=1}^M P_{hjt}^2 \sum_{j=1}^L \sum_{t=1}^M P_{ijt}^2}} \quad (1)$$

$$P_{hjt} = \frac{n_{hjt}}{\sum n_{hjt}} \quad (2)$$

$$P_{ijt} = \frac{n_{ijt}}{\sum n_{ijt}} \quad (3)$$

where, n_h represents the number of residents and n_i represents the number of tourists, $j = 1 \cdots L$ represents space, and $t = 1 \cdots M$ represents time. This index takes values between 0 and 1. Using these indexes, we evaluate the risk of tsunami damage based on the overlap between residents and tourists. A large overlap means that the number of residents and tourists is similar, and thus evacuation guidance is possible; a small overlap means that evacuation guidance by residents is difficult due to a bias toward one side or the other.

5.2 Analysis of Spatial Overlap

In this section, the overlap between residents and tourists for each mesh is clarified.

The niche index values were calculated at 4:00 (early morning), 12:00 (noon), 19:00 (evening), and 22:00 (night) for the summer holidays, when many both residents and tourists were observed. Fig. 6 presents the distribution map of the index calculation results, while Fig. 7 illustrates the discrepancy in the number of residents and tourists. The indexes are expressed by the following equations (4) – (6).

$$a_{hid} = \frac{\sum_{j=1}^L \sum_{d=1}^D P_{hjd} P_{ijd}}{\sqrt{\sum_{j=1}^L \sum_{d=1}^D P_{hjd}^2 \sum_{j=1}^L \sum_{d=1}^D P_{ijd}^2}} \quad (4)$$

$$P_{hjd} = \frac{n_{hjd}}{\sum n_{hjd}} \quad (5)$$

$$P_{ijd} = \frac{n_{ijd}}{\sum n_{ijd}} \quad (6)$$

where, n_h represents the number of islanders, n_i represents the number of tourists, $j = 1 \dots L$ represents the space, and $d = 1 \dots D$ represents the date.

The overlap was high in Ishigaki city because most of the residents stayed within the tsunami inundation zone at any time of the day, while most of the residents stayed outside the tsunami inundation zone in Miyakojima city. In Ishigaki city, the overlap was high in the southern part of the island and low in the central and northern parts, while in Miyakojima city, the overlap was high throughout the island.

In the “Kabira” district in the northwestern part of Ishigaki Island, which is famous as a tourist destination, the number of residents was higher during the evening and early morning hours, while the number of tourists was higher during the daytime hours. At Shimoji Airport on Shimoji Island, the number of tourists was higher from noon to evening. This is thought to be because many tourists visit the airport during the daytime and the airport is in operation, while tourists visit lodging facilities and the city center during the nighttime.

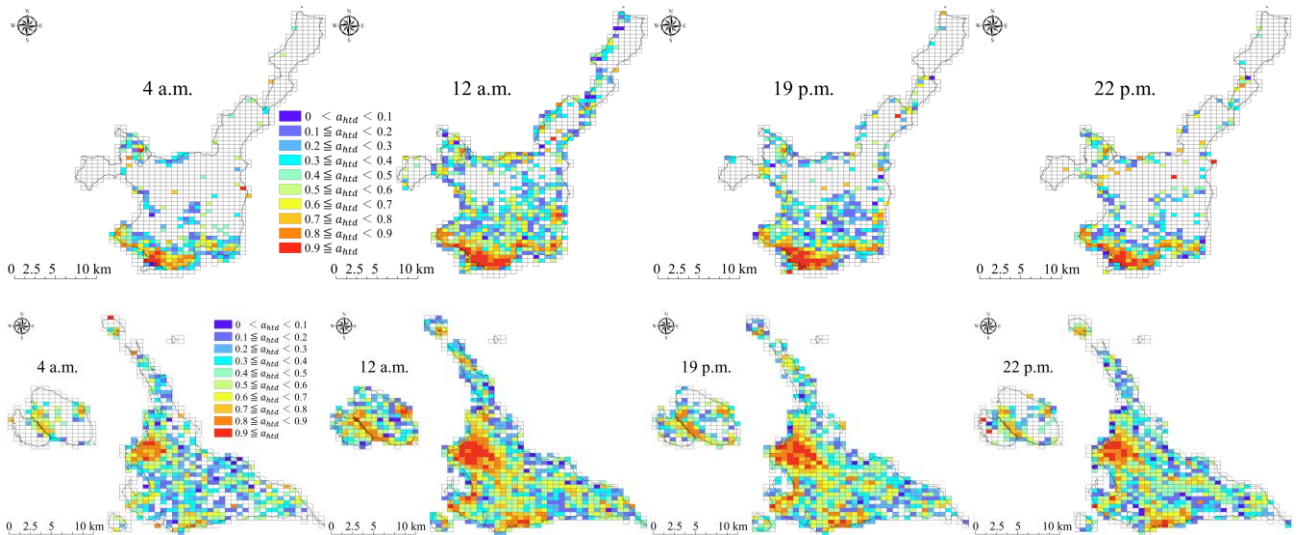


Fig.6.Results for the niche overlap index during summer holidays (top: Ishigaki city, bottom: Miyakojima city)

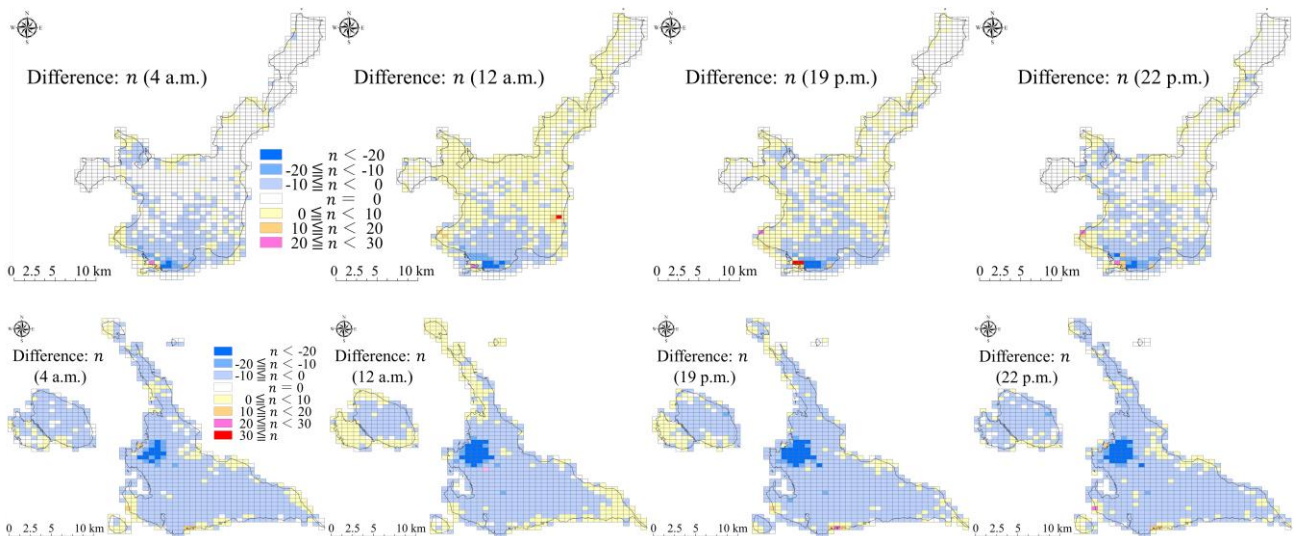


Fig.7.Difference in the number of residents and tourists (top: Ishigaki city, bottom: Miyakojima city)

5.3. Considerations for Disaster Mitigation

The results of the previous section index that more tourists than residents stay in the central and northern part of Ishigaki city, and that the overlap of tourists and residents is small during most of the time. This indicates that it is difficult to expect residents to evacuate tourists in this area.

In places where the overlap between residents and tourists is small, it is not realistic to expect residents to go to the tourists and guide them to evacuate in the event of a disaster. In addition, multilingual audio announcements can be difficult to understand even during normal times, and the more languages that are available, the longer it takes to convey information. Therefore, in such areas, physical support measures such as highly visible signs, road surface markings, and pictograms can be effective evacuation guidance measures for tourists, rather than relying on human assistance.

In certain areas, such as the "Kabira" district in the northwestern part of Ishigaki city and "Shimojijima Airport" on Shimojijima Island, the overlap between residents and tourists varied significantly depending on the time of day. In such areas, it is necessary to flexibly change the priority of evacuation support according to the time of day to increase the effectiveness of evacuation support. Specifically, during the day when tourists concentrate on tourist attractions and airports, the evacuation support should be given priority to the areas around these facilities. Conversely, the period from late at night to early in the morning is characterized by a higher propensity among tourists to patronize lodging facilities, thereby augmenting the necessity for the provision of evacuation support in the surrounding areas. Consequently, the provision of evacuation support in tourist areas must be informed not only by spatial considerations but also by temporal shifts.

6. Conclusion

This study aimed to clarify the possibility of residents assisting tourists with evacuation during disasters. To this end, we conducted a population retention analysis using app location data in Ishigaki City and Miyakojima City in Okinawa Prefecture. We focused on the distribution of residents and tourists by time and region, as well as the overlap between them, to evaluate the possibility of residents guiding tourists to evacuation sites and to consider the priority of evacuation assistance.

The analysis using the niche overlap index revealed that Ishigaki City faces a higher tsunami disaster risk than Miyakojima City. It also identified times and areas with little overlap between residents and tourists, indicating times and areas where providing evacuation support would be challenging. In these areas, establishing physical support measures, such as highly visible signs and road markings, is important. This study's methodology is an effective means of pre-evaluating the possibility of providing evacuation support, and it is believed to have provided useful information for developing disaster mitigation and signage plans in tourist areas.

In future analysis, we will consider land use and facility placement, and we will also examine the applicability of this model in other regions.

Author Contributions

Conceptualization, D.K. and A.U.; methodology, D.K.; writing—original draft preparation, D.K. and A.U.; writing—review and editing, D.K. and A.U.; project administration, D.K.; funding acquisition, D.K.
All authors have read and agreed to the published version of the manuscript.

Funding

This research was supported by the Japan Society for the Promotion of Science (JSPS) Grants-in-Aid for Scientific Research (JP22H00222, JP23H00197, and JP24K15538).

Conflicts of Interest

The authors declare no conflict of interest.

References:

- Beirman, D. (2020). Restoring tourism destinations in crisis: A strategic marketing approach. <https://doi.org/10.4324/9781003117148>
Blog Watcher Inc. <https://www.blogwatcher.co.jp/> (accessed 2021.01.01)

- Glaesser, D. (2006). Crisis management in the tourism industry.
- Jiménez-Guevara, C.D. et al. (2024). Geographical and ecological allopatry effects on niche change in two sister species pairs of hummingbirds in western North America, *Journal of Arid Environment*, 224. <https://doi.org/10.1016/j.jaridenv.2024.105236>
- Kajitani, Y. et al. (2002). Spatial Temporal Analysis of Human Activity Distribution in Disaster Recovery Processes, *Infrastructure Planning Review*, 19(2). (in Japanese)
- Katada, T. & Kanai, M. (2016), The Schol Education to Improve the Disaster Response Capacity: A Case of “Kamaishi Miracle”, *Journal of Disaster Research*, 11(5), pp. 845-856. <https://doi.org/10.20965/jdr.2016.p0845>
- Kawata, Y. (2005). Sumatra-Andaman Islands Earthquake of 26 December 2004, *Annals of Disas. Prev. Res. Inst., Kyoto Univ.*, 48 A. (in Japanese)
- Lou, J. (2006). Entropy and diversity, *OIKOS*, 13(2). <https://doi.org/10.1111/j.2006.0030-1299.14714.x>
- Miyakojima City (2023). Number of Tourists entering the area, <https://www.city.miyakojima.lg.jp/gyosei/toukei/kankouyaku.html> (in Japanese, accessed 2024.10.10)
- Ohsumi, T. et al. (2019). Damage Related to the 2011 Tohoku Earthquake in and Around Kamaishi City- Beyond the Tsunami Disaster-, *Journal of Disaster Research*, 14(9), pp. 1185-1200. <https://doi.org/10.20965/jdr.2019.p1185>
- Okada, N. & Maekawa, K. (1997). Niche Analysis Applied to Assessment of Urban Disaster Risk – A Basic Approach, *Annals of Disas. Prev. Res. Inst., Kyoto Univ.*, 40 B-2. (in Japanese)
- Okinawa Prefecture (2015). About Okinawa Tsunami inundation assumption, <https://www.pref.okinawa.jp/bosaiizen/bosai/1003500/1020541.html> (in Japanese, accessed 2022.01.01)
- Omori, H. et al. (2017). Human Response to Emergency Communication: A Review of Guidance on Alerts and Warning Messages for Emergencies in Buildings, *Fire Technology*, 53, pp. 1641-1668. <https://doi.org/10.1007/s10694-017-0653-3>
- Shinohara, N. & Yamamichi, M. (2021). A modern synthesis of coexistence mechanisms in community ecology, *Japanese Journal of Ecology*, 71, pp. 39-63. https://doi.org/10.18960/seitai.71.2_35 (in Japanese)
- Silverman, B. W. (1986). Density estimation for statistics and data analysis, *Monographs on Statistics and Applied Probability*, <https://ned.ipac.caltech.edu/level5/March02/Silverman/paper.pdf>

Special Issue: Measurement, control, and analysis of motion using ICT and AI

Article

Study on Automatic Detection of Dust Mask Wearing Status in Factories

Wenyuan Jiang ^{1*}, Yuhei Yamamoto ², Hajime Tachibana ³, Keisuke Nakamoto ³, Kunihiro Katai ³, Naoya Nakagishi ⁴ and Hikaru Muranaka ⁴

¹Faculty of Architectural and Environmental Design, Osaka Sangyo University, 3-1-1 Nakagaito, Daito-shi, Osaka 574-8530, Japan

²Faculty of Environmental and Urban Engineering, Kansai University, 3-3-35 Yamate-cho, Suita-shi, Osaka 564-8680, Japan

³Komaihaltec Inc., 1-19-10 Ueno, Taito-ku, Tokyo 110-8547, Japan

⁴Formerly with Faculty of Engineering, Osaka Sangyo University, 3-1-1 Nakagaito, Daito-shi, Osaka 574-8530, Japan

Abstract

In construction and industrial work environments, workers are mandated to wear dust masks to ensure their health and safety. However, in actual field conditions, many workers neglect this requirement due to breathing discomfort and the heat and humidity within the factory. To address this issue, it is necessary to detect workers who are not wearing masks in real time and prompt them to put them on. Therefore, this study proposes a method to determine the wearing status of dust masks using deep learning based on video footage captured within the factory.

Keywords: Automatic safety management; Dust mask; Deep learning; Wearing status classification.

1. Introduction

In construction and industrial work environments, the Industrial Safety and Health Act was enacted in 1972 (Ministry of Health, Labour and Welfare, 2024) to prevent health hazards among workers. Under this law, the use of protective equipment is mandatory to prevent exposure to dust and hazardous substances. In particular, tasks such as concrete drilling and demolition generate large amounts of dust, and it has been pointed out that prolonged exposure can lead to serious occupational diseases such as pneumoconiosis and lung cancer. As a countermeasure, wearing dust masks is considered one of the most fundamental and important safety practices. However, in actual worksites, some workers neglect to wear masks due to discomfort when breathing and the intense heat and humidity of factory interiors and outdoor environments during the summer season. It is also common for workers to return to work after a break without putting their masks back on. These situations accumulate over time, resulting in workers being continuously exposed to dust and eventually developing respiratory illnesses.

In recent years, such health issues have increasingly led to official recognition as work-related injuries or even legal disputes. In fact, there have been court cases (Supreme Court of Japan, 2020; Takamatsu District Court, c. 2024) in which the development of illness due to the lack of dust mask usage became the central issue, with the employer's failure to ensure safety being called into question. Despite the critical importance of dust masks in preventing health hazards, managing their proper usage in the field remains a difficult challenge. Against this background, increasing attention has been given in recent years to the enhancement of safety management at worksites through the application of ICT (Information and Communication Technology) (JNIOH, 2021). Studies involving the use of cameras and sensors to track worker positions, recognize actions, and monitor the use of protective equipment have become more active. With the help of AI-based automatic detection systems, it is becoming possible to monitor and record the conditions of workers in real time.

Received: date, 3 July 2025, Revised: 28 July 2025, Accepted: 21 August 2025, Published: 17 October 2025

* Correspondence: kyo@aed.osaka-sandai.ac.jp

Publisher's Note: JOURNAL OF DIGITAL LIFE. stays neutral with regard to jurisdictional claims in published maps and institutional affiliations.



Copyright: © SANKEI DIGITAL INC. Submitted for possible open access publication under the terms and conditions of the Creative Commons Attribution (CC BY) license (<https://creativecommons.org/licenses/by/4.0/>).

Previous studies have proposed mask detection methods based on deep learning models such as MobileNet (Elnady et al., 2021) and YOLO (Loey et al., 2021), which are capable of detecting the presence or absence of mask usage with a certain level of accuracy. However, at construction sites, instances of improper mask wearing, such as the nose or mouth being exposed, have been observed. Although models such as MobileNet and YOLOv3 are relatively lightweight, they have limitations in representational capacity, making it difficult to extract complex features, such as the degree of mask displacement or the boundary between the mask and the face. In particular, their architectures are less effective for recognizing small objects, which is disadvantageous for classifying masks that cover only part of the face. Therefore, it is considered challenging to apply these techniques directly.

Therefore, this study investigates a method for automatically determining the dust mask wearing status of workers using deep learning-based detection techniques.

2. Related Works

In recent years, the application of deep learning technologies for detecting mask wearing conditions has been actively studied in various research fields. In particular, the spread of COVID-19 and the growing emphasis on safety in work environments have accelerated research on mask detection using surveillance footage and images.

Elnady et al. (2021) proposed a lightweight mask detection model based on MobileNetV2 (Sandler et al., 2018), which achieved high classification accuracy on frontal facial images.

Loey et al. (2021) developed a real-time mask detection method combining YOLOv3 (Redmon et al., 2018) and transfer learning, demonstrating its effectiveness in surveillance video analysis.

Ullah et al. (2022) introduced an integrated model using DeepMaskNet, capable of both detecting the presence or absence of masks and performing face recognition even when a mask is worn, thus maintaining high recognition accuracy under masked conditions.

Pan et al. (2023) proposed a deep learning-based binary classification model to determine mask wearing status from facial images. Based on YOLOv5 (Ultralytics, 2020), the model was optimized for lightweight implementation and accuracy improvement, achieving practical applicability in actual worksites settings.

However, these studies are limited to binary classification—detecting whether a mask is worn or not—and do not address the issue of “improper mask wearing” (e.g., nose uncovered or mask worn under the chin), which is frequently observed in actual work environments. Improper wearing is often excluded from training datasets, resulting in a high likelihood of being misclassified as “properly worn.”

To address this issue, Campos et al. (2022) proposed a ternary classification model that includes “improper wearing” as a third category and demonstrated its effectiveness in reducing misclassification. However, their model was designed for images in which the subject’s head appears relatively large (typically 500 to over 1000 pixels), making it unsuitable for wide-angle surveillance footage in which the head size may be as small as 100 pixels. Moreover, there are various patterns of improper mask wearing, and under the complex conditions typical of actual worksites environments, the classification accuracy remains insufficient for practical implementation.

As described above, while existing mask detection studies have shown a certain level of effectiveness under controlled conditions, they fall short in addressing actual challenges such as improper mask usage at construction and industrial sites. Thus, their applicability in practical scenarios remains limited.

Such improper wearing has been observed in approximately 20–30% of cases (Kagawa Occupational Health Promotion Center, 2002; Ministry of Health, Labour and Welfare, 2020). In addition, in locations where there is a risk of dust exposure, mask wearing from the entrance is required, making entrance checks necessary.

Therefore, in this study, we assume the scenario of checking mask wearing status at the entrance as a dust control measure, and aims to develop an AI-based system to automatically detect mask wearing conditions in the context of dust protection in work environments. The primary focus is on detecting difficult cases such as “improper wearing” (e.g., nose exposed, chin wearing), which are commonly observed on-site and are challenging to detect using existing technologies.

3. Methods

3.1. Overview of Proposed Method

In this study, we propose a method for determining the mask wearing status of workers in videos captured at construction sites and similar environments. In particular, the method needs to account for multiple patterns of "improper wearing." Considering the potential future expansion in the number of such patterns, it would be difficult to handle all cases using a single detection model alone.

Therefore, it is considered difficult to realize the judgment of multiple wearing states solely with detection techniques such as YOLO. In this study, we propose a two-stage approach in which head detection and mask-wearing state classification are separated, incorporating a flexible classification method capable of handling complex wearing states (correctly worn, below nose, below mouth and no mask).

In addition to ensuring classification accuracy, this study aims to reduce implementation costs by utilizing surveillance cameras, while achieving quasi-real-time alerts for improper mask wearing. Furthermore, on-site managers have requested processing at least once per second, making it essential to adopt a method that offers a well-balanced trade-off between accuracy and processing speed.

3.2. Method Selection

Object detection methods such as the YOLO (Redmon et al., 2016) series, SSD (Liu et al., 2016) and RetinaNet (Lin et al., 2017) are widely used. In addition, two-stage detection methods such as Faster R-CNN (Ren et al., 2015) are often employed to improve accuracy; however, these approaches have the drawback of high computational cost and limited real-time performance. As near-real-time processing is also required in practical settings, it is necessary to adopt a method that offers a good balance between accuracy and speed. Among these, the YOLOv5-v9 series achieves both high speed and high accuracy, making it advantageous for deployment in surveillance systems and edge devices that require real-time processing. In particular, YOLOv8 (Ultralytics, 2023) supports multi-scale learning, which improves detection performance for small objects such as faces and masks, and has recently seen increased application in personal protective equipment detection.

On the other hand, classification methods mainly utilize deep convolutional neural networks such as MobileNet (Howard et al., 2017), ResNet (He et al., 2016), DenseNet (Huang et al., 2017), VGGNet (Simonyan and Zisserman, 2015), and Vision Transformer (ViT) (Dosovitskiy et al., 2021).

MobileNet is lightweight and easy to implement; however, it tends to have limited representational power for complex features. VGGNet, while more computationally intensive, has a simple architecture and consistently demonstrates high classification performance, making it effective for tasks involving visually distinctive features. In particular, VGG19 (Simonyan and Zisserman, 2015), with its deeper architecture, enables higher-level feature extraction and is considered well-suited for distinguishing subtle differences in improper mask wearing conditions (e.g., nose exposed or chin wearing). Moreover, since actual worksite applications in this study do not require frame-by-frame real-time processing, the high-accuracy VGG19 is considered the most suitable option.

Based on the above considerations, in this study, to achieve quasi-real-time performance with processing every second, we adopt YOLOv8 in the detection stage for its excellent balance between detection accuracy and processing speed for small objects, and VGG19 in the classification stage for its high accuracy in identifying complex mask wearing conditions, including improper wearing.

3.3. Proposed System

3.3.1 Overview of Proposed System

The proposed system is shown in Fig. 1. The proposed system is divided into a Training Component and a Classification Component. The Training Component consists of two functions: Head Training Data Generation Function and Mask Classification Training Data Generation Function. The Classification Component consists of three functions: Head Detection Function, Head Region Extraction Function and Mask wearing Classification Function.

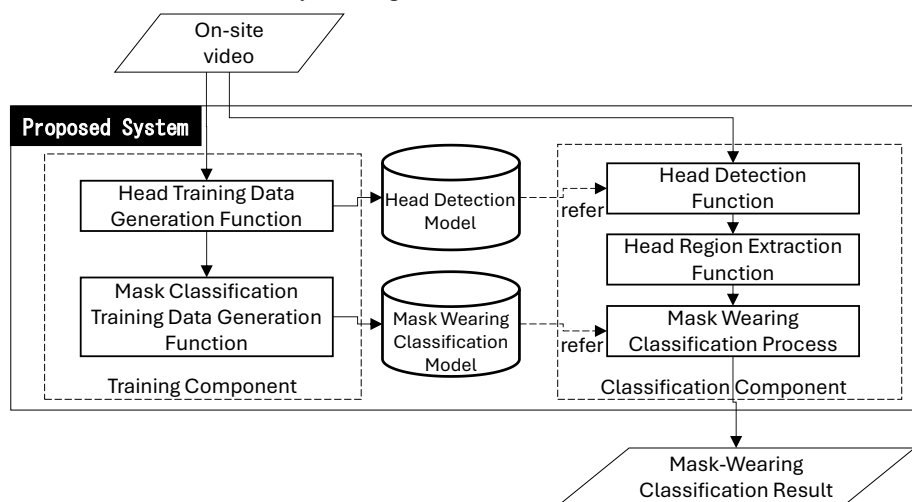


Fig.1. Proposed System

3.3.2 Head Training Data Generation Function

In this function, training data for head detection is generated by manually annotating the heads of workers in video images, as shown in Fig. 2. Then, a Head Detection Model is trained using YOLOv8 based on the annotated data.



Fig.2. Image for Annotation

3.3.3 Mask Classification Training Data Generation Function

In this function, head images are first manually cropped from each frame of the video using the head training data generation function. Next, based on the opinions of on-site factory managers, each head image is labeled with one of four commonly observed categories (Fig.3): Worn Correctly, Worn below Nose, Worn below Mouth, and No Mask. Then, a Mask wearing Classification Model is trained using VGG19 based on these labeled head images.



Fig.3. Four Mask Wearing Status Categories

3.3.4 Head Detection Function

In this function, the heads of workers are detected from site videos in order to determine their mask wearing status, and their position coordinates and sizes are obtained. This is accomplished using a YOLOv8-based Head Detection Model.

3.3.5 Head Region Extraction Function

In this function, head images are extracted to enable the classification of mask wearing status. Specifically, the detected position and size information from the head detection function are used to extract the head regions from the full images.

3.3.6 Wearing Classification Function

In this function, the head images are analyzed using the Mask wearing Classification Model to determine the mask wearing status. Specifically, the model classifies each head image into one of four categories: worn correctly, worn below nose, worn below mouth, or No mask.

4. Results

4.1 Overview of Experiment

To verify the effectiveness of the proposed method, this study conducts three experiments. The first is the Factory Entrance Verification Experiment. The second is the Factory Interior Verification Experiment. The third is the Generalization Verification Experiment.

In this study, when surveillance camera footage was used as training data, many scenes contained only a single person or none at all, making it difficult to collect data covering all patterns. Furthermore, since workers are engaged in their tasks, they face the camera only for short periods, making it challenging to obtain sufficient footage from various angles. Therefore, to ensure an adequate quantity and variety of training data, newly recorded videos were used.

4.2 Factory Entrance Verification Experiment

This experiment simulates a scenario in which mask wearing status is inspected at the entrance of a factory. An example of experimental image is shown in Fig. 4. The video was recorded in Full HD at 30 fps.



Fig.4. Image of Experimental Video at Factory Entrance

The head detection training data consisted of annotated head images extracted from a 58 seconds video in which the five individuals shown in Fig. 5 moved freely within the factory. One frame was sampled every second, resulting in 58 images.

For the mask classification training data, as shown in Fig. 5, each of the five subjects was recorded while rotating 360 degrees under four different mask-wearing conditions. From these videos, 20 head images per class were manually extracted for each individual, yielding a total of 400 images, which were used as the training data.



Fig.5. Sample Image of Training Data Video at the Factory Entrance

The verification video, as shown in Fig. 4, was recorded by capturing five individuals passing through an entrance in various mask wearing conditions. Among them, two workers were wearing their masks below mouth, while the other three represented the remaining categories, one for each. For the verification, 22 images were extracted from the entrance-passing scenes, ensuring representation of all four mask wearing categories. A maximum of three images per individual was used. The purpose was to evaluate whether the system could correctly classify the mask wearing status. The results of the verification are shown in Table 1.

Table 1. Results of Factory Entrance Verification

| Prediction \ Ground truth | Worn correctly | Worn below nose | Worn below mouth | No mask |
|---------------------------|----------------|-----------------|------------------|---------|
| Worn correctly | 3 | 3 | 0 | 0 |
| Worn below nose | 0 | 3 | 0 | 0 |
| Worn below mouth | 0 | 0 | 3 | 0 |
| No mask | 0 | 1 | 2 | 7 |

In the YOLO detection results, the heads of all 22 workers appearing in the 22 images were successfully detected. Therefore, it was confirmed that YOLO can be used to detect workers' heads at the factory entrance.

In the VGG verification results, it showed that the four-class classification achieved an accuracy of 0.73. In addition, since no cases of other patterns were misclassified as “worn correctly,” it can be considered that improper wearing and no mask were detected without omission. The primary causes of misclassification were that the mask color was similar to the background, as shown in Fig. 6, and that the color of the worn mask differed from the training data, as shown in Fig. 7. To address these issues, it is possible to improve the system by incorporating temporal data for sequential analysis or by adding training data with masks of various colors.



Fig.6. Examples Where Background and Mask are of Similar Color



Fig.7. Example Where Mask Color Differs from Training Data

4.3 Factory Interior Verification Experiment

From the results of the second experiment, it was found that when the back of the head—where the mask is not visible—is captured, accurate classification is difficult. In addition, when the side of the head is captured, a decrease in classification accuracy may also be observed. Therefore, in this experiment, we verify the range of head orientations (angles) from which the mask-wearing status can be accurately determined, in order to confirm how much the mask's visibility affects classification accuracy.

This experiment simulates a scene in which the mask wearing status of workers is inspected during work inside a factory. An example of the test video is shown in Fig. 8. The video is approximately 20 seconds long and was recorded in Full-HD at 30 fps. For evaluation, a total of 122 images were extracted from the video at intervals of every five frames. The purpose of the verification is to evaluate the detection accuracy of YOLO and the classification accuracy of VGG. In this scene, there are consistently 1–3 workers, with a total of 282 detection instances obtained.

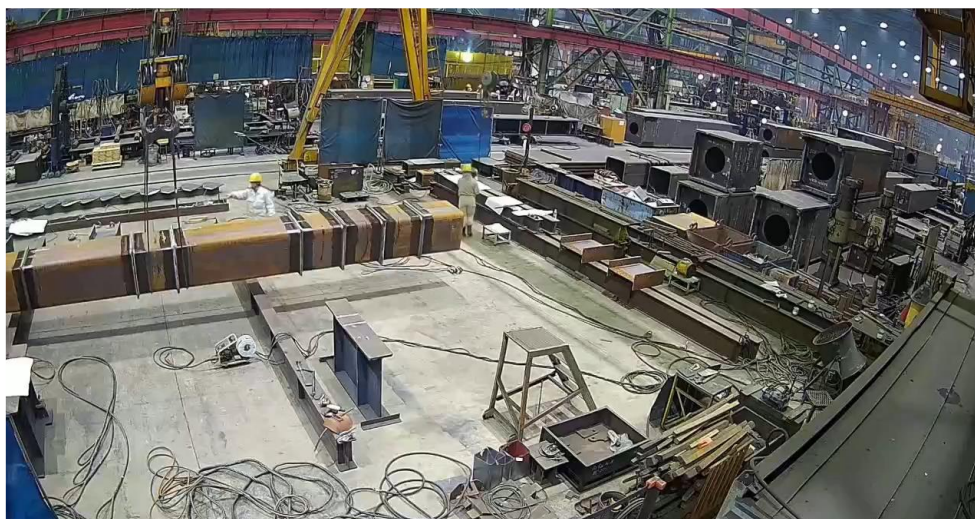


Fig.8. Image of Experimental Video in Factory

The YOLO detection results showed that out of 122 frames, only 49 frames were detected as heads. Accordingly, 31 heads were correctly detected out of a total of 282 individuals. There were also 23 false detections. For the three workers involved, their heads were detected 5, 26, and 0 times, respectively. The detection performance yielded a recall of 0.11, a precision of 0.57, and an F1-score of 0.18. These results indicate that the detection accuracy of YOLO is low in this context. A possible cause is that, in the images captured by the actual surveillance cameras, the workers' heads (average size: approximately 28×28 pixels) are smaller than those in the training data (average size: approximately 42×42 pixels) of the same color, and that the factory background is complex, with the rust color of the pipes (average RGB values: 209, 180, 116) being similar to the color of the helmets (average RGB values: 189, 181, 144).

The classification accuracy of VGG is shown in Table 2.

Table 2. VGG Classification Accuracy in Factory

| Prediction Ground truth | Worn correctly | Worn below nose | Worn below mouth | No mask |
|------------------------------|----------------|-----------------|------------------|---------|
| Worker A (No mask) | 0 | 0 | 0 | 5 |
| Worker B (Worn correctly) | 6 | 0 | 0 | 20 |

In terms of classification accuracy using VGG, the correct prediction rate for the 31 detected head images was 0.35. Upon closer examination, these 31 head images corresponded to two workers. For one worker, five frames were detected, all of which were correctly classified. For the other worker, only 6 out of 26 detected frames were classified correctly.

An analysis of the misclassified images revealed that all of them showed the back or side of the workers' heads (Fig. 9.). This suggests that accurate classification is possible when the majority of the mask is visible in the image. On the other hand, considering that misclassification may lead to false alarms, it is deemed necessary to introduce a new category such as "unclassifiable" for cases where the mask cannot be seen clearly, such as when only the back of the head is visible.



Fig.9. Example of a Captured Back of Head

4.4 Generalization Verification Experiment

When the side of the head is captured, the mask may or may not be recognizable. Therefore, in this experiment, we examine the range of head orientations (angles) that allow accurate determination of mask wearing status.

The experiment is conducted in a laboratory setting, as shown in Fig. 10. As illustrated in Fig. 11, the verification is carried out at four distances from the camera: approximately 4 m, 6 m, 8 m, and 10 m. The camera is installed at a height of about 2.4 m. Although the footage is recorded in 4K at 30 fps, the resolution is downscaled to Full HD to match the conditions of actual worksites.



Fig.10. Location of Generalization Verification Experiment

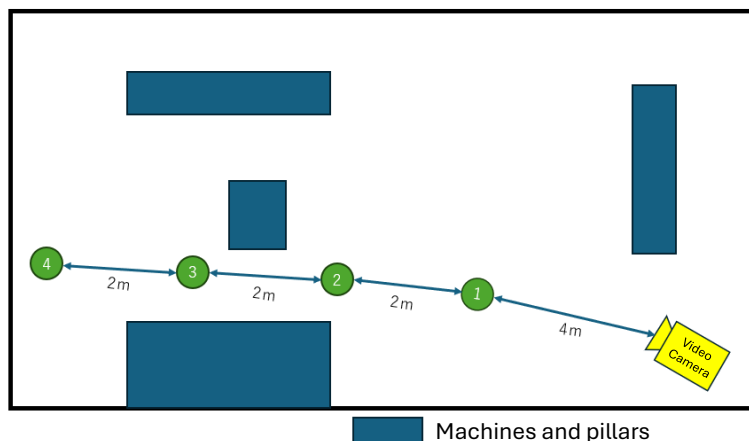


Fig.11. Points of Generalization Validation

At each location, the test subject rotates 360 degrees in 15-degree increments, starting from a position facing the camera (0 degrees). Then, the head region of each subject was visually inspected, manually cropped, and used as the validation data. For the training data, as shown in Fig. 12, images were captured of five participants wearing four different mask wearing conditions while rotating 360 degrees. Additionally, images were extracted at one-second intervals from the recorded videos and used for training. Furthermore, 20 head images per class for each individual were manually extracted from the videos, yielding a total of 400 images, which were employed as the training dataset.

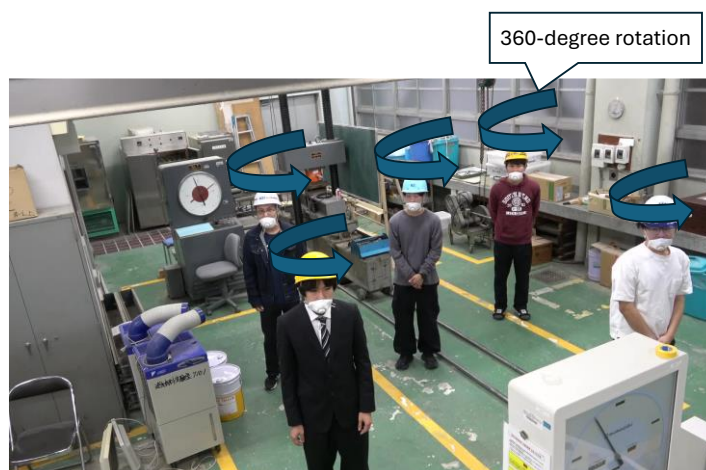


Fig.12. Method of Capturing Training Data

The experimental results are shown in Table 3. From the table, it can be observed that mask classification is difficult within the angular range of approximately 100 to 260 degrees. On the other hand, this range of angles frequently appears in factory environments, which significantly contributes to the decrease in accuracy. Therefore, in future work, a new category labeled "back of the head" will be added to address this unrecognizable range, and further validation will be conducted.

Table 3. Results of the Generalization Verification Experiment

| | Accurately classify | Cannot be accurately classified | Accurately classify |
|--------|---------------------|---------------------------------|---------------------|
| 1. 4m | 0~105 degrees | 120~195 degrees | 210~345 degrees |
| 2. 6m | 0~135 degrees | 150~210 degrees | 225~345 degrees |
| 3. 8m | 0~150 degrees | 165~210 degrees | 225~345 degrees |
| 4. 10m | 0~105 degrees | 120~285 degrees | 300~345 degrees |

5. Conclusions

In this study, we developed a technology to classify the mask wearing status of workers into four categories (properly worn, worn below nose, worn below mouth, and no mask) for automatic safety management at construction sites and factories. The experimental results showed that while the mask wearing status can be accurately classified at the entrance, the classification accuracy within the factory was found to be low. The primary cause is likely the small size of the workers' heads in the footage captured inside the factory. Therefore, we plan to collect real factory data and build a new model. Additionally, to address misclassifications of the back of the head, we plan to add patterns where the mask is not visible, such as the back and side of the head. However, such patterns exhibit substantial differences in visual features depending on the viewing angle, suggesting that consolidating them into a single category may degrade accuracy. Accordingly, future work will explore the optimal number of categories and seek to improve classification performance. Furthermore, we also plan to develop a technology to distinguish between dust masks and general masks. With these improvements, we aim to secure a high-precision mask wearing status classification technology for use in actual worksites environments.

Author Contributions

Conceptualization, W.J., Y.Y., H.T., K.N. and K.K.; methodology, W.J., Y.Y., H.T., K.N. and K.K.; software, W.J., Y.Y., N.N. and H.M.; validation, W.J., N.N. and H.M.; formal analysis, W.J., N.N. and H.M.; investigation, W.J., Y.Y., N.N. and H.M.; data curation, W.J., Y.Y., H.T., K.N., K.K., N.N. and H.M.; writing—original draft preparation, W.J.; writing—review and editing, W.J. and Y.Y.; supervision, W.J. and Y.Y.; project administration, W.J., Y.Y., H.T., K.N. and K.K.; funding acquisition, W.J., Y.Y., H.T., K.N. and K.K.

Funding

This research received no external funding.

Institutional Review Board Statement

Not applicable.

Informed Consent Statement

Not applicable.

Data Availability Statement

Not applicable

Acknowledgments

Not applicable.

Conflicts of Interest

The authors declare no conflict of interest.

Appendix

Not applicable.

References:

- Campos, A., Melin, P. and Sánchez, D. (2023). Multiclass Mask Classification with a New Convolutional Neural Model and Its Real-Time Implementation. *Life*, 13(2), 368. (<https://doi.org/10.3390/life13020368>)
- Dosovitskiy, A., Beyer, L., Kolesnikov, A., Weissenborn, D., Zhai, X., Unterthiner, T., Dehghani, M., Minderer, M., Heigold, G., Gelly, S., Uszkoreit, J. and Houlsby, N. (2021). An image is worth 16x16 words: Transformers for image recognition at scale. *International Conference on Learning Representations*. (<https://arxiv.org/abs/2010.11929>)
- Elnady, A. and Almghraby, M. (2021). Face Mask Detection in Real-Time Using MobileNetv2. *International Journal of Engineering and Advanced Technology*, 10(6), 104-108. (DOI:10.35940/ijeat.F3050.0810621)
- He, K., Zhang, X., Ren, S. and Sun, J. (2016). Deep Residual Learning for Image Recognition. *Proceedings of the IEEE Conference on Computer Vision and Pattern Recognition*. (<https://doi.org/10.48550/arXiv.1512.03385>)

- Howard, A. G., Zhu, M., Chen, B., Kalenichenko, D., Wang, W., Weyand, T., Andreetto, M. and Adam, H. (2017). MobileNets: Efficient Convolutional Neural Networks for Mobile Vision Applications, *arXiv*. (DOI:10.48550/arXiv.1704.04861)
- Huang, G., Liu, Z., Van Der Maaten, L. and Weinberger, K. (2017). Densely Connected Convolutional Networks. *Proceedings of the IEEE Conference on Computer Vision and Pattern Recognition*, 2261-2269. (DOI: 10.1109/CVPR.2017.243)
- Kagawa Occupational Health Promotion Center. (2002): Wearing Status of Dust Masks among Welders in 2002, A Survey on Proper Wearing Conditions. Retrieved from <https://www.kagawas.johas.go.jp/researchStudy/entry-54.html> (accessed July 2, 2025).
- Lin, T. Y., Goyal, P., Girshick, R., He, K. and Dollár, P. (2020). Focal Loss for Dense Object Detection. *Transactions on Pattern Analysis and Machine Intelligence*, 44(2), pp. 318-327. (DOI: 10.1109/TPAMI.2018.2858826)
- Liu, W., Anguelov, D., Erhan, D., Szegedy, C., Reed, S., Fu, C. and Berg, A. (2016). SSD: Single Shot Multibox Detector. *Proceedings of the European Conference on Computer Vision*, 21-37. (https://doi.org/10.1007/978-3-319-46448-0_2)
- Ministry of Health, Labour and Welfare. (2020). Study on the Effects of Powered Air-purifying Respirator (PAPR) with an Electric Fan on Respiratory Burden: Report on the Clinical Research Grant for Industrial Injury and Disease Prevention. Retrieved from <https://www.mhlw.go.jp/content/000680034.pdf> (accessed July 2, 2025).
- Pan, X., Liang, X., Ma, Z. and Deng, P. (2023). A Lightweight YOLOv5 Real-time Mask-wearing Detection Algorithm for the Post-pandemic Era, *Future Sensor Engineering*, 3(8), 21-30. (<https://doi.org/10.54691/fse.v3i8.5523>)
- Redmon, J. and Farhadi, A. (2018). YOLOv3: An Incremental Improvement. *arXiv*. (<https://doi.org/10.48550/arXiv.1804.02767>)
- Redmon, J., Divvala, S., Girshick, R. and Farhadi, A. (2016). You Only Look Once: Unified, Real-time Object Detection. *Proceedings of the IEEE Conference on Computer Vision and Pattern Recognition*, 779-788. (DOI: 10.1109/CVPR.2016.91)
- Ren, S., He, K., Girshick, R. and Sun, J. (2017). Faster R-CNN: Towards Real-time Object Detection with Region Proposal Networks. *IEEE Transactions on Pattern Analysis and Machine Intelligence*, 39(6), pp. 1137-1149. (DOI: 10.1109/TPAMI.2016.2577031)
- Sandler, M., Howard, A., Zhu, M., Zhmoginov, A., and Chen, L. C. (2018). MobileNetV2: Inverted Residuals and Linear Bottlenecks. *Proceedings of the IEEE/CVF Conference on Computer Vision and Pattern Recognition*, 4510-4520. (<https://doi.org/10.48550/arXiv.1801.04381>)
- Simonyan, K. and Zisserman, A. (2015). Very Deep Convolutional Networks for Large-scale Image Recognition. *International Conference on Learning Representations*. (<https://arxiv.org/abs/1409.1556>)
- Supreme Court of Japan (August 31, 2020). Ruling on Asbestos-related Health Damage and State/Manufacturer Duty to Warn and Protect Workers. Retrieved from https://www.rodo.co.jp/precedent/precedent_tag/労働安全衛生法 (accessed July 2, 2025).
- Takamatsu District Court (c. 2024). Decision on Employer Liability for Pneumoconiosis Caused by Asbestos Dust Exposure. Retrieved from https://ascope.net/asbestos_law/damage/石綿粉じんが飛散する工場に勤務していた被災者 (accessed July 2, 2025).
- Ullah, N., Javed, A., Ghazanfar, M., Alsufyani, A. and Bourouis, S. (2022). A Novel DeepMaskNet Model for Face Mask Detection and Masked Facial Recognition, *Journal of King Saud University Computer and Information Sciences*, 34(10), 9905-9914. (<https://doi.org/10.1016/j.jksuci.2021.12.017>)
- Ultralytics. (2020). YOLOv5. Retrieved from GitHub repository. <https://github.com/ultralytics/yolov5> (accessed July 2, 2025).
- Ultralytics. (2023). YOLOv8: Next-generation Object Detection and Segmentation. GitHub repository. Retrieved from <https://github.com/ultralytics/ultralytics> (accessed July 2, 2025).

Special Issue: Measurement, control, and analysis of motion using ICT and AI
Article

Impact of Three-Dimensional Multiple Object Tracking (3D-MOT) on Cognitive Performance and Brain Activity in Soccer Players

Yoshiko Saito^{1,3*}, Hirohisa Isogai^{2,3}, and Kiyohisa Natsume^{1,3}

¹Graduate School of Life Science and Systems Engineering, Kyushu Institute of Technology, 2-4 Hibikino, Wakamatsu-ku, Kitakyushu-shi, Fukuoka 808-0196, Japan

²Department of Human Science, Kyushu Sangyo University, 2-3-1 Matsukadai, Higashi-ku, Fukuoka-shi, Fukuoka 813-8503, Japan

³General Incorporated Association Behavior Assessment Systems Laboratory, 1-28-23 Shiobaru Minami-ku Fukuoka-shi Fukuoka 815-0032, Japan

Abstract

Previous studies on three-dimensional multiple object tracking (3D-MOT) training have primarily been conducted in controlled laboratory settings, with limited evidence on athletes' self-training at home. This study examined the effects of home-based 3D-MOT training using the NeuroTracker X (NTX) application on cognitive performance and brain activity in 29 university soccer players. Participants in the NTX group demonstrated significant post-training improvements in NTX scores ($p < .001$) and 2-back task accuracy ($p = .045$), which indicated enhanced 3D-MOT ability, working memory, and attentional functions. Brain wave recordings during the 2-back task revealed a significant increase in alpha power ($p < .001$). This provided novel evidence that NTX self-training modulated brain activity associated with working memory and attentional control among athletes. These findings highlight the potential of combining NTX interventions with EEG assessments and suggest that NTX-based 3D-MOT self-training may be a practical tool for enhancing attentional aspects of cognitive function in athletes.

Keywords: 3D-MOT Training; NTX; Cognitive Function; EEG; Soccer Players.

1. Introduction

Three-dimensional multiple object tracking (3D-MOT) is a computerized cognitive training method designed to improve the ability to simultaneously track and monitor multiple moving objects in a dynamic 3D space. It is a useful tool for evaluating and improving cognitive function (Parsons et al., 2016). This 3D-MOT training approach has been utilized in various fields, including sports (Faubert, 2013; Romeas et al., 2016; Zhang et al., 2025), education and learning (Che et al., 2023), dementia prevention and older adult care (Burgos-Morelos et al., 2025), and military, aviation, and professional training (Vartanian et al., 2016). Regarding its effects, Parsons et al. (2016) reported that it effectively improved cognitive functions, such as attention, visual processing speed, and working memory (WM). Clinically, it effectively improved attention in children with developmental disorders (Tullo et al., 2018). Assed et al. (2020) demonstrated that combining 3D-MOT training with memory training improved various cognitive functions, including attention, reaction time, visual processing speed, episodic memory, WM, and social cognition; furthermore, the effects were particularly pronounced in the 3D-MOT group.

3D-MOT training tools include Lumosity (Lumos Labs, USA) and CogniFit (CogniFit, USA) for adults, and NeuroTracker (NT; NeuroTracker Inc., Canada). Among these, NT is the most popular in the sports field and has been used in numerous intervention studies to provide scientific evidence in open-skill sports, such as soccer, basketball, and ice hockey (Acquin et al., 2024; Komarudin et al., 2021; Romeas et al., 2016; Tétreault et al., 2024). Open-skill

Received: 24 September 2025, Revised: 9 November 2025, Accepted: 30 January 2026, Published: 20 February 2026

* Correspondence: saitou@baslab.or.jp

Publisher's Note: JOURNAL OF DIGITAL LIFE. stays neutral with regard to jurisdictional claims in published maps and institutional affiliations.



Copyright: © SANKEI DIGITAL INC. Submitted for possible open access publication under the terms and conditions of the Creative Commons Attribution (CC BY) license (<https://creativecommons.org/licenses/by/4.0/>).

sports require immediate judgment and adaptation in rapidly changing external environments with unpredictable opponents, balls, and situations. Although many studies have used NT, all have used stand-alone types, which have limitations in practical cases. These systems are expensive, can only be used at fixed locations, and must be shared among multiple users, which reduces efficiency. Therefore, NeuroTracker X (NTX; NeuroTracker Inc., Canada) was developed for practical use. It can be downloaded to an individual personal computer, which allows users to train anywhere and anytime. Furukado et al. (2024) used NTX to train professional baseball players for approximately five months and investigated the effects of MOT skill training on their batting performance. The results showed a 128% improvement in NTX scores after training, batting performance also improved, particularly regarding zone contact and swinging-strike rates, especially against breaking balls. However, they did not include a control group. Thus, no systematic studies have investigated changes in cognitive abilities or brain activity in athletes via individual NTX self-training.

Cognitive functions, such as WM and attention control, play a crucial role in athletic performance, particularly in open-skill sports that require rapid information processing and decision-making under time constraints (Voss et al., 2010). Although the efficacy of 3D-MOT training has been recently debated (Romeas et al., 2025; Vater et al., 2021), most studies have focused on behavioral outcomes; no research has investigated brain activity in athletes undergoing NTX training.

Brain waves (EEG) reflect brain activity. Electroencephalogram (EEG) devices are small, easy to install, and inexpensive to acquire and maintain. Hence, EEGs are easy to use for measurements in laboratories and in the field (Chikhi et al., 2022). EEG measures delta (1–4 Hz), theta (4–8 Hz), alpha (8–12 Hz), beta (13–30 Hz), and gamma (30–50 Hz) waves. Theta waves are induced by WM, attention, and cognitive loads. Frontal theta waves are reliable markers of cognitive load (Chikhi et al., 2022; Riddle et al., 2021). Alpha waves are involved in high levels of attention and cognitive load (Chikhi et al., 2022; Zhang et al., 2018). Beta waves are associated with concentration and cognitive control and are facilitated during task performance (Chikhi et al., 2022; Riddle et al., 2021; Zhang et al., 2018). Gamma waves are essential for memory processes and contribute to the improvement of cognitive impairments (Kucewicz et al., 2014; Liu et al., 2022).

Previous research that combined 3D-MOT and EEG in healthy individuals, not athletes, reported improved attention, WM, and information processing speed, and changes in resting-state EEG after 3D-MOT training (Parsons et al., 2016). Furthermore, recent studies have demonstrated that real-time EEG neurofeedback during 3D-MOT training can enhance learning using NT (Parsons & Faubert, 2021) and employed alpha waves as the neurofeedback signal. Roy and Faubert (2022) analyzed brain activity across the three stages of a 3D-MOT task (identification, tracking, and recall), which indicated a within-task handoff from attention-dominant to WM-dominant processing when moving from tracking to recall. These studies have greatly contributed to elucidating the neural basis of cognitive functions and visualizing the effects of training. However, the effects of 3D-MOT training on behavioral performance and EEG activity in athletes remain insufficiently understood.

Therefore, we hypothesized that NTX self-training would improve 3D-MOT ability, enhance WM and attention function performance in athletes, and influence brain activity. We investigated the effects of spontaneous 3D-MOT training via NTX on the cognitive performance and brain activity of university soccer players.

2. Methods

2.1 Participants

This study included 30 male students from the soccer team of K.S. University, a highly competitive team with a history of participating in national championships. All participants were regular class players. To minimize variability in soccer players' skill levels, the team's head coach and coaching staff assisted in assigning players to either the NTX training group ($n = 15$) or the control group ($n = 15$). One participant in the control group was absent for the post-measurement; therefore, the final analysis included 15 and 14 participants in the NTX and control groups, respectively. Mean age was 19.9 ± 1.2 years in both groups, with no significant difference ($p = .89$). Mean soccer experience was 13.5 ± 2.2 and 12.6 ± 3.4 years in the NTX and control groups, respectively, with no significant difference ($p = .41$). All participants had normal or corrected-to-normal vision that did not interfere with the experiment. None had prior experience with 3D-MOT training, cognitive tasks, or EEG measurements. Prior to participation, the purpose and procedures of the study, as well as the handling of personal information, were explained in detail. Written informed consent was obtained from all participants after they voluntarily agreed to participate.

2.2 Group Assignment

The head coach and coaching staff were asked to randomly assign players while considering key factors such as academic year (age) and playing position. This procedure ensured that individual characteristics did not become unevenly concentrated in either group while maintaining randomness. No intentional selection bias based on the performance level was introduced.

2.3 Protocol

To examine the effects of 3D-MOT training using NTX, a pre-post experimental design was employed. Both the NTX training and control groups completed the same cognitive tasks and EEG recordings before (pre) and after (post) the training. The pre- and post-experimental periods lasted approximately 10 days. Training for the NTX group began immediately after the pre-experimental period and ended at the onset of the post-experimental period. The procedure was as follows: first, EEG devices were attached to the participants; subsequent cognitive tasks, which included the 3D-MOT and n-back tasks, were performed. EEG was measured during the n-back task. The NTX training group underwent 30 NTX training sessions over a 9-week period at home in addition to their usual activities. The control group did not undergo any specific training and continued their usual activities. The pre- and post-experimental days are referred to as Pre and Post days, respectively.

2.4 NTX Training

Participants in the NTX group were asked to bring their own computers on the Pre day and install the NTX software (<https://neurotracker.net/download-installer/>). They were provided with instructions on how to use the software and perform training so they could begin at home. Participants were asked to sit at a distance of approximately 40 cm from their eyes to the PC screen, following the NTX manual. They were lent 3D anaglyph glasses and wore them during NTX training. These glasses enabled them to view 3D images. Participants completed 30 NTX sessions using their own PCs, performing 1–2 sessions per day at a frequency of 2–3 days per week. Each session comprised 20 trials and lasted approximately 6 min. One trial comprised steps (a) to (d), as shown in Fig. 1. First, eight yellow balls appeared on the screen, and four of them—the targets to be tracked—appeared in a slightly larger, highlighted form for two seconds (Identification phase; Fig. 1a). Subsequently, the balls moved for 8 s along unpredictable linear paths in a three-dimensional space perceived through the 3D glasses (Tracking phase; Fig. 1b). Within this depth-rich virtual space, the balls travelled forward/backward and upward/downward, occasionally bouncing off the walls or colliding with each other, creating highly unpredictable motion patterns that participants had to track. After the balls stopped, numbers were displayed on them, and the participant had to select the numbers of the four target balls using either a touchscreen or keyboard, depending on each PC (Recall phase; Fig. 1c). Finally, the correct target balls were highlighted (Feedback phase; Fig. 1d). If the participants' choices were correct, the moving speed of the balls increased in the next trial; if there was a mistake with at least one ball, the speed decreased. After approximately three seconds, the next trial started. The speed varied via a 1-up/1-down staircase method (Levitt, 1971) to determine the ball speed threshold. The ball speed threshold was a numerical value that indicated the maximum speed of the balls at which a participant could accurately track the targets during the trials. Each session included 20 trials. The NTX score was displayed at the end, reflecting the ball speed threshold (Parsons et al., 2016). The higher the NTX score, the faster a participant was able to track the target balls. NTX scores for each session were shared between the participant and the experimenter, and other participants could not view the records.

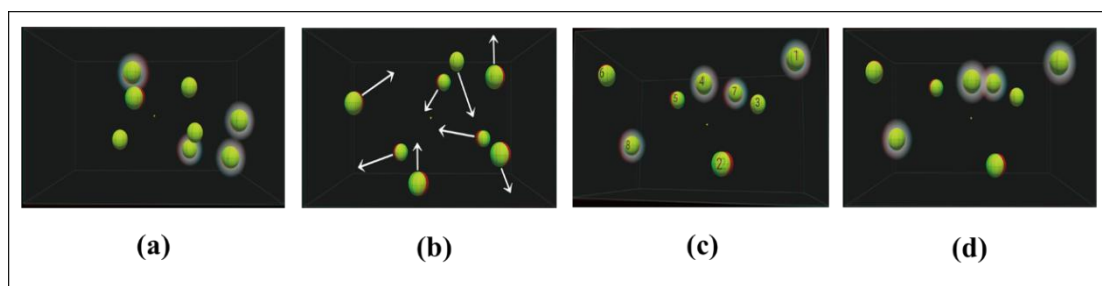


Fig. 1 Time course of a trial in NTX training.
One trial included the steps from (a) to (d). Details are described in the text.

2.5 Cognitive Tasks

2.5.1 3D-MOT Task

Experiments were conducted at the university’s Sport Psychology Laboratory during Pre and Post days. All participants visited the laboratory to participate. The NTX score reflected 3D-MOT skills (Isogai, 2023); hence, we used this score as an evaluation metric for the skills. Each participant completed one NTX session via a 15.5-inch notebook computer (NEC Endeavor SE-09079, Japan) as a cognitive task. Participants wore 3D anaglyph glasses and sat at a distance of approximately 40 cm from the screen, similar to during training. On the Pre day, responses were uniformly made using the keyboard, with 2–3 practice trials conducted to explain the task, followed by the main measurement task.

2.5.2 Working Memory Task

The n-back task is one of the most common experimental paradigms used in WM studies. Recently, variations of the n-back procedure (Owen et al., 2005) have been widely adopted. We used the non-verbal WM task shown in Fig. 2. This task was a modified version of the n-back task (n = two and three) (Park et al., 2013). It was conducted on a 15.5-inch notebook computer (NEC Endeavor SE-09079, Japan). Fig. 2 presents the time sequence of the computer screen for the 2- and 3-back tasks. We mainly explained the 2-back task. When the trial began, at the starting cue, a black cross appeared at the center of the screen for one second. Subsequently, a pair of symbols appeared on the left and right sides of the cross. Each pair of symbols was presented on the screen for 1–5 s. Participants were asked to click on the “different” symbol via the PC mouse within five seconds if the symbols on the previous two screens were different (Fig. 2, left) from the current ones. If the two symbols were the same, the participant clicked the “same” (“同じ” in Japanese) button at the bottom of the screen (Fig. 2, left). The positions of the symbols did not change across three continuous screens. Participants completed 20 trials, after which their accuracy rate and average reaction time were recorded. For the 3-back task, participants compared a pair of symbols with a pair from the previous three screens; other points were the same as those in the 2-back task. On the Pre day, we conducted 2–3 practice trials before the measurement task. The custom-made task program was developed using Unity (Unity Technologies, USA).

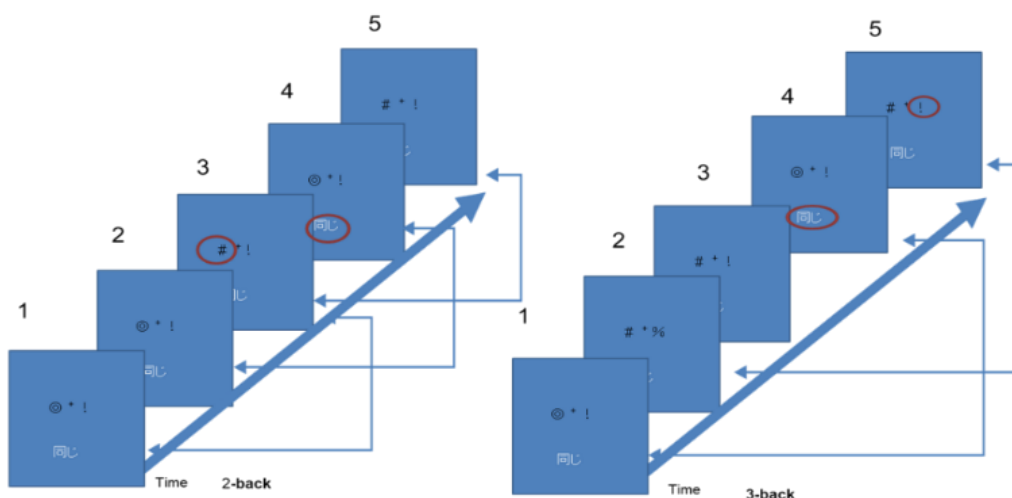


Fig. 2 Time sequences of the PC screen in 2- (left) and 3-back (right) tasks.

Numbers indicate the order of the presented screen. The participant compared the two screens indicated by both arrows. Symbols included the following 18 symbols: ○, △, □, !, #, &, ¥, ★, →, ←, ↓, ↑, ※, ◎, ♪, @, ◇, ▽.

2.6 EEG Measurement

EEG signals were recorded to investigate the effects of NTX-based 3D-MOT self-training on brain activity. EEG was measured from approximately 10 s before the 2- and 3-back tasks until after the task on both days. It was measured at the Fz site of the brain based on the International 10/20 system. A reference electrode was placed on the mastoid and a ground electrode on the FPz site. EEG was measured at the Fz electrode site because frontal midline activity, particularly at Fz, is considered a stable and sensitive indicator of WM load and attentional control (e.g., Gevins & Smith, 2000). Measurement was performed using the Intercross-415 (Intercross Co., Ltd., Japan). Sampling frequency was set to 1000 Hz. Analysis was performed using MATLAB R2020b (MathWorks, USA) with EEGLAB (<https://sccn.ucsd.edu/eeglab/index.php>). After blink artifacts were excluded via the ICA program, short-time fast

Fourier transformation analysis was performed. Baseline correction was performed using the power values for 0.5 s prior to task onset. Time-average power values during the task were calculated for each frequency band: θ (4–8 Hz), α (8–13 Hz), β (14–29 Hz), and γ (30–40 Hz).

2.7 Statistical Analysis

A two-way repeated-measures ANOVA was performed for the results of each cognitive task and EEG power, with the factors of measurement timing (Pre day \times Post day) and group (NTX group \times control group). Due to PC trouble, some data from the NTX and control groups in the 2-back task at the Post day and the 3-back task at the Pre day were lost, respectively. Hence, data from 14 participants in the NTX and control groups in the 2-back task at the Post day, and 15 in the NTX group and 13 in the control group in the 3-back task at the Pre day were analyzed. Based on the statistical analysis results, a simple main-effect test was conducted when an interaction was significant. Figures were presented only when a significant interaction was observed. A p -value of $<5\%$ was considered statistically significant. Statistical analysis was performed using the open source software JASP version 0.19.2 (Netherlands, <https://jasp-stats.org/download/>).

3. Results

3.1 NTX Training

In the 9-week NTX self-training, the NTX group completed approximately 29 sessions (28.5 ± 3.8 , $n = 15$). Of the 15 participants, 12 completed 30 sessions as requested, whereas three did not achieve the goal. The average NTX score for the first three sessions was 1.8 ± 0.4 , and the score for the last three sessions was 2.3 ± 0.3 , representing approximately 128% of the baseline score by self-training.

3.2 Cognitive Tasks

3.2.1 3D-MOT Task

A two-way repeated-measures ANOVA was conducted on the NTX scores with the factors of measurement timing and group. Results revealed a significant interaction ($F(1, 27) = 5.52$, $p = .026$, $\eta^2_p = .170$); therefore, a simple main effect test was conducted. Regarding the measurement timing factor, the NTX group demonstrated significantly higher scores at Post ($M = 2.34$, $SD = .43$) than at Pre ($M = 1.79$, $SD = .44$) ($F(1, 27) = 12.26$, $p = .004$). Conversely, the control group demonstrated no significant difference between Pre ($M = 1.46$, $SD = .48$) and Post ($M = 1.58$, $SD = .46$) ($F(1, 27) = 1.43$, $p = .247$). Regarding group factors, no significant difference was observed between the NTX ($M = 1.79$, $SD = .44$) and control groups ($M = 1.46$, $SD = .48$) at Pre ($F(1, 27) = 3.61$, $p = .068$). However, at Post, the NTX score in the NTX group ($M = 2.34$, $SD = .43$) was significantly higher than that in the control group ($M = 1.58$, $SD = .46$) ($F(1, 27) = 21.09$, $p < .001$) (Fig. 3).

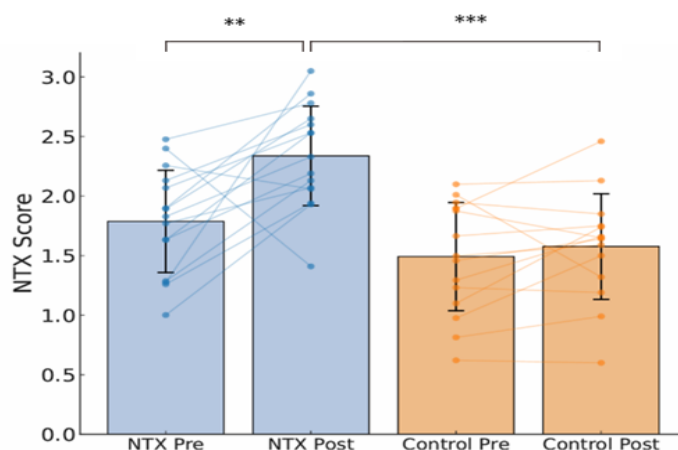


Fig. 3 NTX scores before and after NTX training.

In this and subsequent figures, the blue and orange bars indicate the mean values for the NTX and control groups, respectively. Error bars indicate the standard deviation. Blue and orange dots represent individual data points, and lines connecting each point indicate individual changes between Pre and Post.

3.2.2 Working Memory Task

A two-way repeated-measures ANOVA was conducted to examine the accuracy rate and reaction time for the 2-back and 3-back tasks. The results revealed a significant interaction in the accuracy rate for the 2-back task ($F(1, 26) = 4.43, p = .045, \eta_p^2 = .145$). Therefore, a simple main effect analysis was performed. Regarding the measurement timing factor, the NTX group showed significantly higher accuracy at post-test ($M = 85.00, SD = 11.77$) than at pre-test ($M = 78.93, SD = 14.83$) ($F(1, 26) = 6.34, p = .026$). However, no significant difference was observed in the control group between Pre ($M = 83.21, SD = 8.23$) and Post ($M = 81.43, SD = 8.86$) ($F(1, 26) = 0.39, p = .542$). For the group factor, no significant differences were observed between the two groups at either Pre ($F(1, 26) = 0.89, p = .353$) or Post ($F(1, 26) = 0.82, p = .373$) (Fig. 4). Furthermore, no significant interaction was observed in the accuracy rate in the 3-back task. Regarding reaction time, no significant interactions were observed in either the 2-back or 3-back tasks. However, a significant main effect of measurement timing was observed in both tasks; participants responded faster at Post than at Pre (2-back: $F(1, 26) = 4.97, p = .035, \eta_p^2 = .160$; 3-back: $F(1, 26) = 7.23, p = .012, \eta_p^2 = .218$). The shortened reaction time at Post in both groups could be due to the practice effect of task performance.

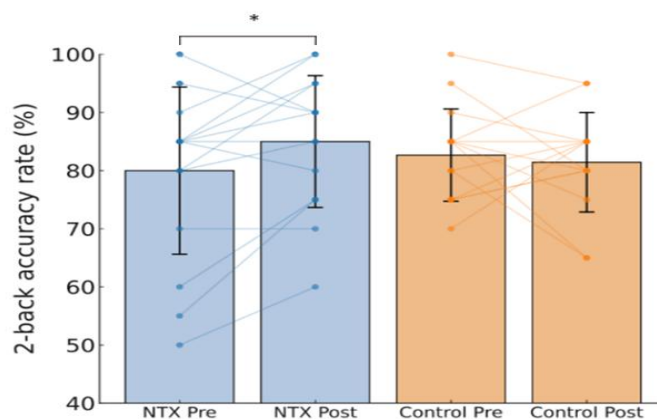


Fig. 4 Accuracy rate in 2-back task before and after NTX training.

3.3 EEG Measurement

A two-way repeated-measures ANOVA was conducted on the EEG power at the Fz site during the 2- and 3-task, with measurement timing and group as factors. Results revealed a significant interaction in the alpha band during the 2-back task ($F(1, 27) = 4.33, p = .047, \eta_p^2 = .138$); therefore, simple main effects were examined. In the NTX group, alpha power was significantly higher at Post ($M = -.003, SD = .060$) than at Pre ($M = -.075, SD = .060$) ($F(1, 27) = 20.76, p < .001$). However, no significant difference was observed between Pre ($M = -.047, SD = .078$) and Post ($M = -.035, SD = .072$) ($F(1, 27) = 0.22, p = .646$) in the control group. Since the task-related alpha power was baseline-corrected, the values were negative when alpha was suppressed relative to the baseline. For the group factor, no significant between-group differences were observed at either Pre or Post. Furthermore, no significant interactions were observed in the 2-back task for the frequency bands, except the alpha band. During the 3-back task, no interactions were observed in any frequency band at the Fz.

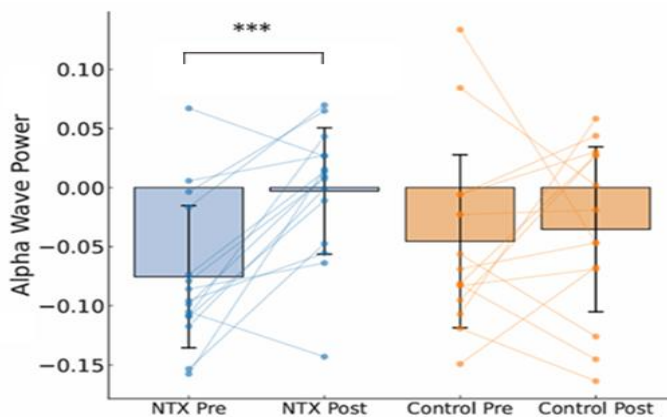


Fig. 5 Alpha power in 2-back task before and after NTX training.

4. Discussion

A previous study asked participants to visit the laboratory for 3D-MOT training via NT. In contrast, NTX allowed users to train independently anytime and anywhere. While this usability is a major advantage, it also carries the risk that participants may skip sessions without supervision. Therefore, to support the feasibility of a self-directed training environment, we implemented minimal monitoring using a management interface and provided brief reminder-style verbal check-ins. These procedures were not intended to enhance motivation or performance, but to prevent large deviations in training adherence. Participants completed 28.5 ± 3.8 NTX sessions over nine weeks (approximately two months). Furukado et al. (2024) trained 12 professional baseball players for approximately five months using NTX to examine the impact of MOT skill training on batting performance; however, they did not include a control group. In comparison, the present study included a control group, thereby increasing the internal validity of the findings regarding NTX-based 3D-MOT training in university athletes.

4.1 Effects of NTX Training on Cognitive Function

4.1.1 3D-MOT Ability

Furukado et al. (2019) reported that when university baseball players underwent 12 sessions of training over three weeks via NT, the NT training group demonstrated significant improvements in scores and a positive effect on 3D-MOT ability. Participants underwent controlled training in the laboratory. In our study, which used NTX self-training with university soccer players, a significant interaction effect was observed (measurement timing \times group) (Fig. 3); the improvement rate of NTX scores was 130% in the NTX group compared with 107% in the control group. This was similar to previous results obtained with self-training in participants' usual environments. Hence, a definite improvement in 3D-MOT ability could be achieved in approximately 30 sessions, even in self-training outside a controlled laboratory environment.

4.1.2 Working Memory Task

We investigated whether NTX training influenced cognitive abilities beyond 3D-MOT performance by examining its effects on the 2-back and 3-back tasks in university soccer players. The n-back task is widely used to assess WM function (Owen et al., 2005). In this task, participants compare the current stimulus with the stimulus presented n steps earlier, requiring online monitoring, updating of stored information, sustained attention, and attentional switching between stimuli (Kane et al., 2007). Since the n-back task places considerable demands on several key WM processes (Owen et al., 2005), it shares conceptual similarities with the cognitive processes engaged in during NTX training, which consists of four sequential phases: recognition, tracking, recall, and feedback. Roy and Faubert (2022) have demonstrated that these phases involve a dynamic handover between attention and WM, suggesting that 3D-MOT training can influence both domains.

In the present study, a significant interaction was observed in the accuracy of the 2-back task, with performance improving only in the NTX group (Fig. 4). These results indicated that NTX training enhanced WM and attentional regulation under moderate task demands. However, no significant improvement was observed in the 3-back task. Pre-training accuracy was lower for the 3-back task (73.3%) than for the 2-back task (81.3%), indicating that the 3-back task imposed a higher cognitive load. Previous research has shown that prefrontal activation decreases when task demands escalate from 2-back to 3-back (Callicott et al., 1999), suggesting increased neural inefficiency under a heavier cognitive load.

Together, these findings suggest that NTX training can be transferred to cognitive tasks with moderate WM demands, whereas transfer to more complex WM processing appears to be limited within the current intervention framework. NTX uses a 1-up/1-down adaptive staircase procedure (Levitt, 1971), which increases task speed after correct responses and decreases task speed after errors, thereby maintaining difficulty at an individually appropriate level. Rather than implying that the protocol was inherently designed to enhance maximal WM capacity, it is more appropriate to interpret that the adaptive load adjustment may have aligned optimally with the cognitive demands of the 2-back task. This alignment may support the transfer of attentional regulation and short-term information maintenance. By contrast, the substantially higher cognitive load of the 3-back task may have exceeded the range in which transfer effects could have occurred under the present training conditions.

4.2 Effects of NTX Training on Brain Activity

We compared the power of brain waves that reflected brain activity during 2/3-back tasks before and after NTX training. Consequently, a significant increase in alpha wave power was observed during the 2-back task in the NTX

group after training (Fig. 5). Increased alpha waves have been associated with inhibitory functions that protect against external interference (Toscani et al., 2010; Tuladhar et al., 2007; Webster & Ro, 2020).

The pre-training accuracy rate of the 2-back task was 81.3%, indicating that the difficulty level was close to optimal for the participants. This task required participants to remember the screen two steps earlier while focusing attention on holding the screen one step back, which involved relatively short-term memory and repeated attention. Thus, the observed increase in alpha waves may be associated with the “gate function” (Jensen & Mazaheri, 2010), which prioritizes necessary information and suppresses unnecessary information. Furthermore, an increase in alpha waves may reflect the suppression of neural activity and selective allocation of cognitive resources, which may indicate a state in which unnecessary information for the task is effectively suppressed (Klimesch, 2012; Payne & Sekuler, 2014). This change suggests improved neural efficiency, selective control of attentional resources, and reduced cognitive load through training. The pre-training accuracy of the 3-back task was 73.3%, reflecting a higher cognitive load than the 2-back task; when tasks are perceived as difficult and demanding, the brain must allocate more resources to the task, which can result in the suppression of the alpha band in the frontal region (Jensen & Mazaheri, 2010).

Although the frontal theta activity is widely regarded as a reliable index of cognitive load, no significant interaction was observed in the theta band in the present study. Since NTX is designed to optimize attentional regulation through its adaptive speed-based algorithm, it is more likely to enhance attentional processes rather than directly increasing WM capacity. This interpretation aligns with the behavioral findings that showed improvement only in the 2-back task and not in the 3-back task.

In contrast, alpha oscillations are strongly associated with sustained attention and attentional resource allocation. Therefore, the significant interaction observed in alpha power likely reflects the preferential modulation of attentional control mechanisms induced by NTX training.

5. Limitations and Future Directions

The primary methodological limitation of the present study is related to the characteristics of the NTX training protocol. The results indicate that the protocol effectively enhanced attentional control; however, improvements in higher-level WM processes were not observed during the intervention period. This suggests that the current NTX configuration may not impose sufficient memory-related cognitive load to induce measurable gains in WM capacity. To target WM enhancement more directly, future implementations of NTX may require increased task complexity; for example, by increasing the number of tracked objects or incorporating dual-task paradigms that simultaneously demand attention and memory retention. Such modifications may better challenge the memory manipulation processes necessary for improvements in higher-order WM functioning.

Furthermore, the development of more advanced adaptive training environments, including AI-based feedback systems capable of dynamically monitoring progress and adjusting task difficulty, may contribute to establishing a fully autonomous training model that effectively supports attentional enhancement and WM improvement.

6. Conclusion

This study investigated the effects of NTX-based 3D-MOT self-training on the cognitive function and brain activity of university soccer players. NTX is a personal, autonomously performed training tool that differs from the laboratory-based standalone 3D-MOT systems used in previous research. Consistent with earlier findings, NTX performance improved significantly after approximately 30 training sessions. A significant interaction was observed in the 2-back task, with the accuracy increasing only in the NTX group. This finding indicates that NTX training successfully enhanced attentional control and short-term information updating—cognitive processes that are closely aligned with the adaptive attentional demands imposed by the NTX protocol. In contrast, no improvement was observed in the more demanding 3-back task, suggesting that the present NTX training configuration was insufficient to induce measurable gains in higher-level WM manipulation.

Neurophysiological results supported this interpretation; alpha-band power, an index of sustained attention and inhibitory control, significantly increased during the 2-back task following NTX training, whereas frontal theta activity, typically associated with WM load, did not show any interaction effects. Together, these findings indicate that the NTX protocol primarily strengthened attentional regulation rather than the higher-order WM capacity. In addition to these laboratory outcomes, our findings also have important implications for real-world soccer cognition. Effective soccer performance frequently requires players to maintain the spatial positions of multiple teammates and

opponents, while making rapid decisions under pressure. These situations rely on both WM and attentional control. Based on the present results, the NTX training protocol appears to have selectively enhanced attentional processes, as evidenced by improvements in the 2-back task and alpha-band modulation. Therefore, although enhancement of more complex working memory processes could not be demonstrated under the present training conditions, the improvement in attentional capacity induced by NTX training may contribute to a reduction in passing errors during play and to improved decision-making accuracy.

Author Contributions

Conceptualization, Y. S.; methodology, Y. S., H. I., and K. N.; software, H. I. and K. N.; validation, Y. S.; formal analysis, Y. S. and K. N.; investigation, Y. S. and H. I.; resources, Y. S. and K. N.; data curation, Y. S.; writing—original draft preparation, Y. S.; writing—review and editing, Y. S. and K. N.; visualization, Y. S.; supervision, K. N.; project administration, Y. S. and K. N. All authors have read and agreed to the published version of this manuscript.

Funding

This research received no external funding.

Institutional Review Board Statement

This study was conducted in accordance with the guidelines of the Declaration of Helsinki and its future amendments and was approved by the Kyushu Institute of Technology Human Experimentation Committee (protocol #23-01).

Informed Consent Statement

Informed consent was obtained from all participants involved.

Acknowledgments

We would like to express our gratitude to the head coach and coaching staff of K.S. University for their cooperation in recruiting participants.

Conflicts of Interest

The authors declare no conflicts of interest.

References:

- Acquin, J. M., Desjardins, Y., Deschamps, A., Fallu, É., Fait, P., & Corbin-Berrigan, L. A. (2024). Impact of biological sex, concussion history and sport on baseline NeuroTracker performance in university varsity athletes. *Frontiers in Sports and Active Living*, 6, 1372350. <https://doi.org/10.3389/fspor.2024.1372350>
- Assed, M. M., Rocca, C. C. D. A., Garcia, Y. M., Khafif, T. C., Belizario, G. O., Toschi-Dias, E., & Serafim, A. D. P. (2020). Memory training combined with 3D visuospatial stimulus improves cognitive performance in the elderly: pilot study. *Dementia & Neuropsychologia*, 14(03), 290-299. <https://doi.org/10.1590/1980-57642020dn14-030010>
- Burgos-Morelos, L. P., Rivera-Sánchez, J. D. J., Santana-Vargas, Á. D., Arreola-Mora, C., Chávez-Negrete, A., Lugo, J. E., ... & Pérez-Pacheco, A. (2025). Effect of 3D-MOT training on the execution of manual dexterity skills in a population of older adults with mild cognitive impairment and mild dementia. *Applied Neuropsychology: Adult*, 32(2), 328-337. <https://doi.org/10.1080/23279095.2023.2169884>
- Callicott, J. H., Mattay, V. S., Bertolino, A., Finn, K., Coppola, R., Frank, J. A., ... & Weinberger, D. R. (1999). Physiological characteristics of capacity constraints in working memory as revealed by functional MRI. *Cerebral cortex*, 9(1), 20-26. <https://doi.org/10.1093/cercor/9.1.20>
- Che, X., Zhang, Y., Lin, J., Zhang, K., Yao, W., Lan, J., & Li, J. (2023). Two-dimensional and three-dimensional multiple object tracking learning performance in adolescent female soccer players: The role of flow experience reflected by heart rate variability. *Physiology & Behavior*, 258, 114009. <https://doi.org/10.1016/j.physbeh.2022.114009>
- Chikhi, S., Matton, N., & Blanchet, S. (2022). EEG power spectral measures of cognitive workload: A meta-analysis. *Psychophysiology*, 59(6), e14009. <https://doi.org/10.1111/psyp.14009>
- Ericsson, K. A. (2006). The influence of experience and deliberate practice on the development of superior expert performance. *The Cambridge handbook of expertise and expert performance*, 38(685-705), 2-2. <https://doi.org/10.1017/CBO9780511816796.001>

- Faubert, J. (2013). Professional athletes have extraordinary skills for rapidly learning complex and neutral dynamic visual scenes. *Scientific reports*, 3(1), 1154. <https://doi.org/10.1038/srep01154>
- Furukado, R., Akiyama, D., Sakuma, T., Shinriki, R., Hagiwara, G., & Isogai, H. (2019). Training Effects of Multiple Target Tracking Skills and Visual Search Strategies. *Ergonomics*, 55(2), 33-39. <https://doi.org/10.5100/jje.55.33>
- Furukado, R., Saito, Y., Ichikawa, T., Morikawa, K., Enokida, D., & Isogai, H. (2024). Transferability of multiple object tracking skill training to professional baseball players' hitting performance. *Journal of Digital Life*, 4(SpecialIssue). <https://doi.org/10.51015/jdl.2024.4.S5>
- Gevins, A., & Smith, M. E. (2000). Neurophysiological measures of working memory and individual differences in cognitive ability and cognitive style. *Cerebral cortex*, 10(9), 829-839.
- Hatfield, B. D., Haufler, A. J., Hung, T. M., & Spalding, T. W. (2004). Electroencephalographic studies of skilled psychomotor performance. *Journal of Clinical Neurophysiology*, 21(3), 144-156. <https://doi.org/10.1097/00004691-200405000-00003>
- Isogai, Hirohisa. (2023). Training Effects of Multiple Target Tracking Skills. *Journal of Biomechanical Society*, 47(3), 166. https://doi.org/10.3951/sobim.47.3_166
- Jensen, O., & Mazaheri, A. (2010). Shaping functional architecture by oscillatory alpha activity: gating by inhibition. *Frontiers in human neuroscience*, 4, 186. <https://doi.org/10.3389/fnhum.2010.00186>
- Kane, M. J., Conway, A. R., Miura, T. K., & Colflesh, G. J. (2007). Working memory, attention control, and the N-back task: a question of construct validity. *Journal of Experimental psychology: learning, memory, and cognition*, 33(3), 615. <http://www.apa.org/>
- Klimesch, W. (2012). Alpha-band oscillations, attention, and controlled access to stored information. *Trends in cognitive sciences*, 16(12), 606-617. <https://doi.org/10.1016/j.tics.2012.10.007>
- Komarudin, K., Mulyana, M., Berliana, B., & Purnamasari, I. (2021). NeuroTracker Three-Dimensional Multiple Object Tracking (3D-MOT): a tool to improve concentration and game performance among basketball athletes. *Annals of Applied Sport Science*, 9(1), 0-0.
- Kucewicz, M. T., Cimbalknik, J., Matsumoto, J. Y., Brinkmann, B. H., Bower, M. R., Vasoli, V., ... & Worrell, G. A. (2014). High frequency oscillations are associated with cognitive processing in human recognition memory. *Brain*, 137(8), 2231-2244. <https://doi.org/10.1093/brain/awu149>
- Levitt, H. C. C. H. (1971). Transformed up-down methods in psychoacoustics. *The Journal of the Acoustical society of America*, 49(2B), 467-477. <https://doi.org/10.1121/1.1912375>
- Liu, C., Han, T., Xu, Z., Liu, J., Zhang, M., Du, J., ... & Wang, Y. (2022). Modulating gamma oscillations promotes brain connectivity to improve cognitive impairment. *Cerebral Cortex*, 32(12), 2644-2656. <https://doi.org/10.1093/cercor/bhab371>
- Owen, A. M., McMillan, K. M., Laird, A. R., & Bullmore, E. (2005). N-back working memory paradigm: A meta-analysis of normative functional neuroimaging studies. *Human brain mapping*, 25(1), 46-59. <https://doi.org/10.1002/hbm.20131>
- Parsons, B., Magill, T., Boucher, A., Zhang, M., Zogbo, K., Bérubé, S., ... & Faubert, J. (2016). Enhancing cognitive function using perceptual-cognitive training. *Clinical EEG and neuroscience*, 47(1), 37-47. <https://doi.org/10.1177/1550059414563746>
- Parsons, B., & Faubert, J. (2021). Enhancing learning in a perceptual-cognitive training paradigm using EEG-neurofeedback. *Scientific Reports*, 11(1), 4061. <https://doi.org/10.1038/s41598-021-83456-x>
- Payne, L., & Sekuler, R. (2014). The importance of ignoring: Alpha oscillations protect selectivity. *Current directions in psychological science*, 23(3), 171-177. <https://doi.org/10.1177/0963721414529145>
- Riddle, J., McFerren, A., & Frohlich, F. (2021). Causal role of cross-frequency coupling in distinct components of cognitive control. *Progress in Neurobiology*, 202, 102033. <https://doi.org/10.1016/j.pneurobio.2021.102033>
- Romeas, T., Guldner, A., & Faubert, J. (2016). 3D-Multiple Object Tracking training task improves passing decision-making accuracy in soccer players. *Psychology of Sport and Exercise*, 22, 1-9. <https://doi.org/10.1016/j.psychsport.2015.06.002>
- Romeas, T., Goujat, M., Faubert, J., & Labbé, D. (2025). No transfer of 3D-Multiple Object Tracking training on game performance in soccer: A follow-up study. *Psychology of Sport and Exercise*, 76, 102770. <https://doi.org/10.1016/j.psychsport.2024.102770>
- Roy, Y., & Faubert, J. (2022). Significant changes in EEG neural oscillations during different phases of three-dimensional multiple object tracking task (3D-MOT) imply different roles for attention and working memory. *arXiv preprint arXiv:2207.14470*. <https://doi.org/10.48550/arXiv.2207.14470>

Received: 24 September 2025, Revised: 9 November 2025, Accepted: 30 January 2026, Published: 20 February 2026

* Correspondence: saitou@baslab.or.jp;

Publisher's Note: JOURNAL OF DIGITAL LIFE. stays neutral with regard to jurisdictional claims in published maps and institutional affiliations.



Copyright: © SANKEI DIGITAL INC. Submitted for possible open access publication under the terms and conditions of the Creative Commons Attribution (CC BY) license (<https://creativecommons.org/licenses/by/4.0/>).

- Tullo, D., Guy, J., Faubert, J., & Bertone, A. (2018). Training with a three - dimensional multiple object - tracking (3D - MOT) paradigm improves attention in students with a neurodevelopmental condition: a randomized controlled trial. *Developmental science*, 21(6), e12670. <https://doi.org/10.1111/desc.12670>
- Tétreault, É., Fortin-Guichard, D., McArthur, J., Vigneault, A., & Grondin, S. (2024). About the predictive value of a 3D multiple object tracking device for talent identification in elite ice hockey players. *Research Quarterly for Exercise and Sport*, 95(2), 370-383. <https://doi.org/10.1080/02701367.2023.2216266>
- Toscani, M., Marzi, T., Righi, S., Viggiano, M. P., & Baldassi, S. (2010). Alpha waves: a neural signature of visual suppression. *Experimental brain research*, 207(3), 213-219. <https://doi.org/10.1007/s00221-010-2444-7>
- Tuladhar, A. M., Huurne, N. T., Schoffelen, J. M., Maris, E., Oostenveld, R., & Jensen, O. (2007). Parieto-occipital sources account for the increase in alpha activity with working memory load. *Human brain mapping*, 28(8), 785-792. <https://doi.org/10.1002/hbm.20306>
- Vater, C., Gray, R., & Holcombe, A. O. (2021). A critical systematic review of the Neurotracker perceptual-cognitive training tool. *Psychonomic bulletin & review*, 28(5), 1458-1483. <https://doi.org/10.3758/s13423-021-01892-2>
- Vartanian, O., Coady, L., & Blackler, K. (2016). 3D multiple object tracking boosts working memory span: Implications for cognitive training in military populations. *Military Psychology*, 28(5), 353-360. <https://doi.org/10.1037/mil0000125>
- Voss, M. W., Kramer, A. F., Basak, C., Prakash, R. S., & Roberts, B. (2010). Are expert athletes 'expert' in the cognitive laboratory? A meta-analytic review of cognition and sport expertise. *Applied cognitive psychology*, 24(6), 812-826. <https://doi.org/10.1002/acp.1588>
- Webster, K., & Ro, T. (2020). Visual modulation of resting state α oscillations. *eneuro*, 7(1). <https://doi.org/10.1523/ENEURO.0268-19.2019>
- Zhang, H., Watrous, A. J., Patel, A., & Jacobs, J. (2018). Theta and alpha oscillations are traveling waves in the human neocortex. *Neuron*, 98(6), 1269-1281. <https://doi.org/10.1016/j.neuron.2018.05.019>
- Zhang, Y., Zhang, Y., Zhang, Q., Pan, X., Xu, G., & Li, J. (2025). Three-dimensional multiple object tracking (3D-MOT) performance in young soccer players: Age-related development and training effectiveness. *PloS one*, 20(8), e0312051. <https://doi.org/10.1371/journal.pone.0312051>